

Diss. ETH No. 19085

Microscopy of Ultra-Cold Fermionic Lithium

A dissertation submitted to the
ETH ZURICH

for the degree of
Doctor of Sciences

presented by
BRUNO ZIMMERMANN
Dipl.-Phys., ETH Zürich, Switzerland
born 22.01.1980
citizen of
Vilters-Wangs, Wangs SG
Switzerland

accepted on the recommendation of
Prof. Dr. Tilman Esslinger
Prof. Dr. Andreas Wallraff

2010

Kurzfassung

Eine einzigartige Eigenschaft von ultrakaltem, fermionischem Lithium ist, dass Streueigenschaften bei Zwei-Körper-Stössen durch eine präzise kontrollierbare Streulänge bestimmt sind. Diese kann in der Nähe einer Feshbach Resonanz über einen weiten Bereich durchgestimmt werden. So können nichtwechselwirkende und wechselwirkende Fermigase erzeugt werden. Unterhalb einer kritischen Temperatur wird das wechselwirkende Fermigas supraflüssig. Dies erlaubt es uns dann, Suprafluidität in Bereichen verschieden starker Wechselwirkung zu untersuchen. Die relevante Längenskala in diesen Fermigasen ist die Fermiwellenlänge von typischerweise $1\mu\text{m}$.

In dieser Arbeit wird ein experimenteller Aufbau präsentiert, der Mikroskopie von ultrakalten Fermigasen mit einer optischen Auflösung von 700nm ermöglicht. Innerhalb von 15s werden Lithium Atome ausschliesslich mithilfe von optischen Kühltechniken auf Temperaturen unterhalb der Fermitemperatur gekühlt. Dies erfolgt in mehreren Schritten: Zuerst werden die Atome mit einem Zeeman Abbremsler zum Stillstand gebracht und danach in einer magneto-optischen Falle gefangen. Anschliessend werden sie zur evaporativen Kühlung in eine Resonator-dipolfalle umgeladen. In einem weiteren Schritt werden die Atome, gefangen im Fokus eines Laserstrahls, 27cm weit in eine Glasszelle transportiert, die optischen Zugang für zwei Mikroskopobjektive bietet. Das zwischen den axial ausgerichteten Mikroskopobjektiven platzierte Fermigas wird in einem letzten Schritt evaporativ gekühlt, um schlussendlich ein entartetes Fermigas zu erhalten. In dieser Anordnung können Mikrodipolpotentiale durch das eine Mikroskopobjektiv erzeugt werden. Mit dem zweiten werden die Mikropotentiale, Absorptions-, Fluoreszenz- und Phasensignale von darin gefangenen Atomen lokal ausgelesen und charakterisiert.

Der Zustand eines atomaren Gases kann lokal durch Grössen wie der Dichte und der Dichtefluktuationen bestimmt werden. Wir haben die Dichteprofile von Nichtwechselwirkenden entarteten Fermigasen und molekularen Bose-Einstein Kondensaten nachgewiesen und zudem die lokale Dichte wie auch Dichtefluktuationen eines gefangenen nichtwechselwirkenden Fermigases mit hoher optischer Auflösung gemessen. Im Falle eines entarteten Fermigases wurden reduzierte Dichtefluktuationen beobachtet, die eine direkte Konsequenz des Pauli-Prinzips sind und somit die fermionische Natur der

Atome zum Vorschein bringen. Weil das Fermigas während der Abbildung im thermischen Gleichgewicht ist, kann das Fluktuations-Dissipations Theorem angewendet werden. Dieses besagt, dass die Dichte und ihre Fluktuationen zueinander proportional sind, wobei die Temperatur die Proportionalitätskonstante ist. Wir haben gezeigt, dass mit dieser auf Fluktuationsmessungen basierenden Methode die Temperatur eines Fermigases bestimmen werden kann.

Abstract

A unique feature of ultra-cold lithium atoms is that their scattering properties are determined by a precisely controllable two-body scattering length, which can be tuned over a wide range by accessing a Feshbach resonance. Non-interacting and interacting Fermi gases can be created. At a critical temperature, the latter can undergo a phase transition to a superfluid, which allows one to study fermionic superfluidity in different interaction regimes with a single system. Its relevant length scale is the Fermi wavelength, which is typically $1\mu\text{m}$.

In this thesis, we present an experimental apparatus that enables microscopy of a trapped ultra-cold gas of fermionic lithium with an optical resolution of 700nm . In a time sequence of 15s , lithium atoms are cooled to degeneracy by applying optical cooling technics only. The cooling procedure occurs in several steps: First, atoms are Zeeman slowed and magneto-optically trapped. Then, they are transferred to a high finesse resonator dipole trap for a first evaporative cooling step. In order to do microscopy, atoms are transported in a running wave dipole trap over a distance of 27cm to a region of high optical access and cooled below the Fermi temperature. In the final position, atoms are placed between two microscope objectives, which are aligned along their common optical axis. In this configuration, optical micro dipole potentials can be formed by means of the first microscope objective. With the second objective, the created potentials as well as atomic absorption, fluorescence and phase signals of atoms which are trapped in these potentials, can be locally detected and quantitatively characterized.

The state of the atomic ensemble is locally revealed by observable quantities such as the density and density fluctuations. Density profiles of non-interacting degenerate Fermi gases and Bose-Einstein condensates of tightly bound pairs will be shown. High resolution microscopy has allowed us to observe the local density and its fluctuations of a trapped non-interacting Fermi gas in-situ. In the case of a degenerate Fermi gas, a suppression of fluctuations has been observed, which is a direct manifestation of the Pauli exclusion principle and hence of the fermionic nature of the atoms. Because the atomic ensembles are in thermal equilibrium when being imaged, the fluctuation-

dissipation theorem can be used to relate the mean density to its fluctuations, with a proportionality constant, the temperature. With the obtained data, a fluctuation based-temperature measurement has been demonstrated.

Contents

1	Introduction	1
2	Ultra-cold gases of fermionic Lithium	9
2.1	Non-interacting Fermi gas in a harmonic trap	12
2.2	Interaction between atoms	15
2.3	Fermionic pairs	21
2.4	Molecular Bose-Einstein condensate	22
2.5	Bardeen-Cooper-Schrieffer state	26
2.6	Crossover from BEC to BCS	28
3	Design of the experimental apparatus	31
3.1	Overview of the experimental setup	32
3.2	Oven chamber	33
3.3	Zeeman slower	37
3.4	Main chamber	42
3.5	Glass cell	44
3.6	Optical traps	46
3.7	Standing wave dipole trap	48
3.8	Running wave dipole trap	59
3.9	Imaging Systems	65
3.10	Microscope Objectives	65
3.11	Magnetic field coils	70
3.12	Laser system	77

4	Performance of the apparatus	83
4.1	Experimental preparation of an ultra-cold Fermi gas of Li6	83
4.2	Characterization of the preparation procedure	86
4.3	Observation of degenerate Fermi gases	95
4.4	Microscopy of a Fermi gas	99
5	Local observation of antibunching in a trapped Fermi gas	103
6	Outlook	111
	Bibliography	113
	Acknowledgements - Danksagung	125
	Curriculum Vitae	127

1 Introduction

In a classical gas, atoms are treated as distinguishable, point-like particles. This assumption is valid from a quantum mechanical point of view if the extension of the wave packet of an atom, which is given by the thermal de Broglie wave length, is much smaller than the interatomic distance. When reducing the temperature of the gas, the thermal de Broglie wave length increases up to the point where the wave packets of neighboring atoms start to overlap. These atoms can no longer be considered as classical particles; they need to be treated as indistinguishable particles and their intrinsic angular momentum, the spin, starts to play a prominent role. For the case of atoms with integer spin — bosons — wave packets can overlap. Below a critical temperature, this gives rise to the phase transition to a Bose-Einstein condensate [1, 2, 3] — a macroscopic number of atoms occupies the same state, which can be regarded as one wave packet of many atoms. As opposed to this, atoms with half integer spin — fermions — cannot occupy the same quantum state according to Pauli's principle [4] and effectively repel each other despite the absence of interactions.

An intriguing aspect of trapped ultra-cold atomic gases is that their bosonic or fermionic nature and physical quantities are macroscopically observable in the density distribution. For example, in the case of a non-interacting Fermi gas, the repulsion of neighboring wave packets leads to a so-called Fermi pressure, which causes a spatial extension of the gas that is larger than that of a classical gas [5, 6, 7]. Furthermore, characteristics of Fermi statistics can be measured from the shape of the density distribution.

In an attractively interacting two-component spin mixture, the atomic Fermi gas can undergo a phase transition to a superfluid phase at a critical temperature. The decrease in energy in the superfluid phase is enabled by pairing between fermions of different spin. The two extreme cases of pairing are either fermions forming weakly bound pairs, so-called Cooper pairs, or strongly bound molecules which can be treated as composite bosons. The superfluid phase of Cooper pairs is described by the Bardeen-Cooper-Schrieffer [BCS] state [8, 9] and that of molecules is a Bose-Einstein condensate [BEC] [1, 2, 3]. Superfluidity of attractively interacting fermionic pairs is again revealed

in their density distribution, which could be macroscopically demonstrated by exciting a vortex pattern — a superfluid characteristic of a gas.

When we started setting up a new experimental apparatus in the year 2006, interest in the field of ultra cold atomic Fermi gases was growing rapidly. In the previous few years, methods developed to achieve Bose-Einstein condensation [10, 11, 12, 13] had been successfully applied to cool Fermi gases to below the Fermi temperature [5]. These temperatures were achieved by cooling fermions first with resonant light, followed by either evaporative cooling of a spin mixture or sympathetic cooling of a Bose-Fermi mixture [14]. Research groups had managed to measure the density distribution of non-interacting atomic Fermi gases and reveal the difference in Bose and Fermi statistics [6, 7]. Even the physics of attractively interacting Fermi gases were within reach of investigation, because the interaction strength could be tuned almost at will by making use of Feshbach resonances [15, 16]. Strongly bound pairs could be formed and molecular Bose-Einstein condensation could be demonstrated [17, 18, 19]. In the most recent development, the pairing mechanism was studied with respect to the interaction strength [20, 21, 22]. Superfluidity of fermionic pairs [23] has been observed in a regime, where pairing can neither be described by Cooper pairs nor by molecules [24, 25, 26, 27, 28, 29]. It was the first time that this entire intermediate regime, the so-called BEC-BCS crossover [30, 31, 32], could be accessed with a single system. With the precise control over parameters such as temperature, atom number in each spin state [33, 34] and interaction strength, the phase diagram of ultra-cold Fermi gases at the critical temperature can be studied [35, 36, 37].

In most experiments, information about the ultra-cold atomic ensemble is gained by optical imaging of its density distribution (see [38] and references therein). Because of limited optical resolution, measurements on these ensembles have been carried out with systems of very large size, and/or after free expansion from the trapping potential in order to make use of the increased size of the expanded cloud. For the same reason, optical dipole potentials to trap atoms were relatively large in size. In the case of a periodic potential, its periodicity extends over the whole cloud [39]. Small local substructures in the optical dipole potential could not be created. Naturally appearing or artificially generated spatial substructures in the density distribution of the Fermi gas could only be detected if their length scales were larger than the imaging resolution.

How powerful high resolution optical control can be has been demonstrated in an experiment with a Bose-Einstein condensate trapped in a double well potential, where tunneling dynamics could be measured [40, 41]. The artificially created substructure is the barrier between the two wells. The dimension of this barrier is so small that tunneling occurs between the two wells. With a sufficiently high imaging resolution, the atom number in each well can be measured [42]. In the case of a Bose-Einstein condensate, dynamics in the density distribution is governed by coherent tunneling,

which is caused by the difference in chemical potential: the superfluid phase in each well evolves such that an oscillating mass current between the wells known as Josephson oscillation [43] can be observed. Here, the generation of the double well potential represents local control with respect to tunneling dynamics. If the separation between the two wells is larger than the optical resolution, but still small enough for a reasonably high atomic tunneling rates, the dynamics in the atomic ensemble can be read out locally.

In order to make optical control with high resolution accessible to Fermi gases, we decided to build up an experiment that enables us to create and locally probe substructures in the density distribution of a trapped Fermi gas. This experimental setup allows one to prepare a quantum gas of fermionic lithium close to absolute zero temperature in a potential which can be arbitrarily controlled down to the length scale of the optical scattering cross section — the smallest experimentally relevant length scale for optical detection of the atomic density distribution. In addition, read out of the atomic density distribution is possible at the same length scale.

The starting point was the conception of an experimental apparatus that integrates the physics of strongly correlated ultra-cold fermions with local control and readout. Atomic ensembles have to be prepared at temperatures below the Fermi temperature, which are typically on the order of $1\mu\text{K}$. At that temperature, the thermal de Broglie wave length is approximately 200nm and typical interatomic separations are about 400nm . We aimed for optical resolutions on the length scale of the interatomic separation, both to create optical dipole potentials and to image atoms.

The actual design of an experimental apparatus and the potential for local measurements strongly depend on the atomic element of choice. The preparation procedure for experimenting with an ultra-cold atomic ensemble including cooling, trapping and imaging is different for every element and imposes a variety of technical constraints. There were several reasons for choosing ${}^6\text{Li}$. Previous experiments have shown, that ${}^6\text{Li}$ and ${}^{40}\text{K}$, which are two stable and commercially available fermionic alkali isotopes, can be cooled down to degeneracy [5, 7, 44, 45, 46, 47, 48, 49, 50, 6, 51, 52, 53, 54, 55, 56, 57]. The ability to measure locally the dynamics of trapped atomic ensembles with a low mass are more favorable, because the dynamics which are given by the tunneling rate are exponentially decreasing with the mass of the element and the well separation. A low mass, therefore, allows a less stringent requirement for the needed well separation and hence optical resolution. Experimental progress in cooling lithium down to degeneracy by using optical techniques only [50, 58] as well as the fortunate technical aspect of the recent availability of novel laser and tapered amplifier diodes for laser cooling supported the choice.

A major experimental effort lies in cooling an atomic ensemble of ${}^6\text{Li}$ below Fermi

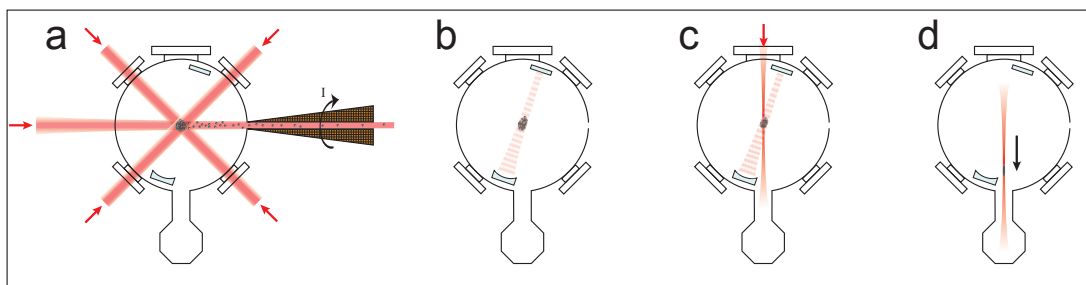


Figure 1.1: An atomic beam, which traverses a decreasing magnetic field is decelerated by a counter-propagating laser beam (a). Magneto-optically trapped atoms are transferred first into a standing wave dipole trap (b) and then into a much smaller running wave dipole trap (c), before being transported into the glass cell (d), the so-called science chamber. There, high resolution microscopy of the atomic ensemble is done.

temperature and placing it between two microscope objectives. First, enriched fermionic lithium, which is commercially available in solid blocks of about 1g, is heated to about 400°C and evaporated into an ultra-high vacuum chamber. The atomic vapour is collimated into a beam with a mean velocity of about 1000m/s .

In a second step, atoms are laser cooled with resonant photon scattering. The atoms in the beam are decelerated to about 60m/s (corresponding to a temperature of 0.93K) by a counter-propagating laser beam in a so-called Zeeman slower [59], before they are trapped in a so-called magneto-optical trap (figure 1.1a)[60]. Three counter-propagating laser beams exert dissipative forces on atoms. Due to a magnetic gradient field, forces are position-dependent such that atoms are slowed and always repelled in a backwards direction to their movement into the trap center. Inside this trap, atoms still move randomly at a certain minimum threshold temperature of about $140\mu\text{K}$, which is called the Doppler temperature [14].

In a third step, atoms are evaporatively cooled [14, 61]. Evaporation is known as the process when particles of highest energy leave the atomic ensemble, while the remaining particles rethermalize to a lower mean temperature. In order to be able to cool the atoms by evaporation, they first have to be transferred into a conservative potential to reduce heating caused by resonant photon scattering, either in a magnetic or optical dipole trap.

For efficient loading, both traps need to have good spatial overlap. Such a large volume optical dipole trap can only be created with sufficiently large light power, which is here obtained by the power enhancement inside an optical resonator [62]. With a two mirror configuration, atoms are trapped in a standing wave dipole trap (figure 1.1b). During the evaporation process, the dipole trap depth is lowered and the atoms

of highest energy always leave the atomic ensemble, i.e they escape from the trap. If the remaining atoms simultaneously thermalize by elastic scattering, the Boltzmann distribution is shifted to lower temperatures. Because scattering of identical fermions at low temperatures is inhibited by the Pauli exclusion principle, we decided to cool a spin mixture of fermionic lithium [50, 52]. While lowering the depth of the standing wave dipole potential, a second much smaller dipole trap is turned on (figure 1.1c). This time, the attractive potential is created by a tightly focused laser beam, a so-called running wave dipole trap [63]. After turning off the standing wave dipole trap, pre-cooled atoms remain in the running wave dipole trap with a trap depth of $300\mu\text{K}$. Here, the trap depth can be lowered much further for technical reasons to finally obtain a degenerate Fermi gas.

The fourth and last step is the transport of the ultra-cold gas, which is still trapped in the dipole potential of the tightly focused laser beam [64]. Atoms are moved from the place, where they are initially cooled and trapped, to a region of high optical access, where the two microscope objectives are installed. Since the atoms are also axially confined by the focussed laser beam, they always remain at the focus (figure 1.1d). By simply moving the lens that focusses the trapping laser beam, the atomic ensemble can be placed between the two microscope objectives that are positioned above and below a glass cell. After a final evaporation, the temperature of the atomic ensemble reaches values below the Fermi temperature (200nK). Now, the degenerate Fermi gas can be controlled and read out with high optical resolution.

Lithium atoms can be confined within or repelled from optical dipole potentials by inducing a dynamic Stark shift with far off resonant light — in this case with laser light at a wave length of 767nm or 532nm , respectively. For imaging, lithium atoms are illuminated with resonant light at a wave length of 671nm to detect either fluorescence or absorption [38]. In order to control atoms on a short length scale, light at these wave lengths is focused by a specially designed and chromatically corrected microscope objective. This enables local control and readout at the 700nm length scale of the optical resolution.

For this experimental apparatus, two identical microscope objectives were axially aligned above and below a glass cell (figure 1.2). The microscope objective above the glass cell is used to create optical dipole potentials, while the one below is used to read out either the light of created potentials or imaging light. In order to achieve such a high optical resolution, the glass cell needs to be integrated in the optical system of the two microscope objectives. In addition, the optical resolution can only be maintained if alignment tolerances below $1\mu\text{m}$ in the x-,y- and z-directions and an angular tilt of 0.1° relative to the glass cell are not exceeded at any time. Very high passive and active stability for the mounting and a reproducible adjustment procedure are also crucial.

The high optical access offered by the octagonally shaped glass cell allows one to create diverse optical dipole potentials either in static or dynamic configurations. In the axis of the two microscope objectives, dipole potentials can be read out and quantitatively analyzed. This large variety of small scaled potentials, which can be created in a controlled way, opens up many possibilities for probing fermionic ensembles in the BEC-BCS crossover in different configurations.

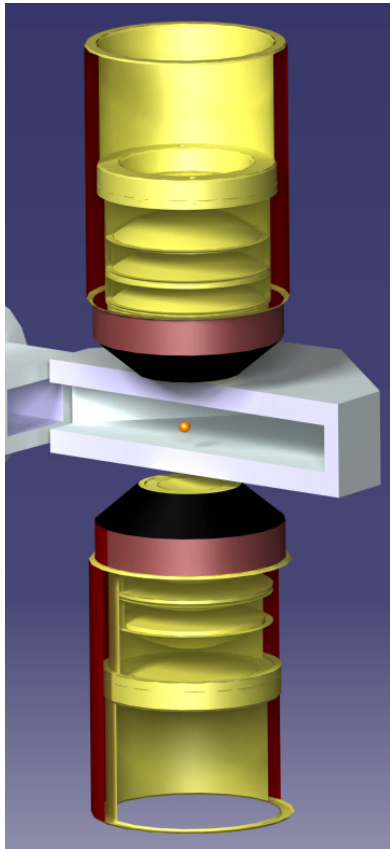


Figure 1.2: The illustration shows a partially cut CAD drawing of the configuration of two microscope objectives mounted above and below a glass cell. Atoms are schematically shown in the center of the cell. They can be trapped in a dipole trap that is created by a laser beam focused by means of the upper microscope objective. The imaging light is detected with the microscope objective mounted below the glass cell.

Within the scope of this thesis we have designed and built the experimental apparatus and created ultra-cold Fermi gases. We have managed to access the BEC-BCS crossover and to trap and image attractively and non-interacting Fermi gases with a resolution up to 700nm. The experimental setup and the preparation procedure will be presented in detail in section 3 and 4.

The optical resolution achieved has allowed us to perform in-situ measurements of the density distribution and especially of the density fluctuations. In a classical gas, the variance of the atom number δN^2 in a small subsystem is equal to the mean number of atoms $\langle N \rangle$. We succeeded to observe for the first time that in a degenerate Fermi gas the variance is suppressed with respect to the non-degenerate case. This manifestation of anti-bunching is a direct result of the Pauli principle and constitutes a local probe of quantum degeneracy.

At thermal equilibrium, the density fluctuations are universally linked to the thermodynamic properties of the gas through the fluctuation-dissipation theorem, which can be expressed as:

$$k_B T \frac{\partial \langle N \rangle}{\partial \mu} = \delta N^2, \quad (1.1)$$

where T is the temperature of the gas, μ the chemical potential and k_B the Boltzmann constant. We use this relation to demonstrate a fluctuation based temperature measurement proposed recently [65]. The particularly

appealing feature of this method is that it allows determining the temperature of the gas irrespective of its equation of state or specific interaction. The single assumption of a local density approximation enables one to assign a local chemical potential to any position in the trap and to determine the compressibility $\frac{\partial \langle N \rangle}{\partial \mu}$ directly from the mean density profiles. Measurement of the variance δN^2 then yields the temperature. We anticipate that this method will prove very fruitful for thermometry in strongly correlated systems [66] and measurement of susceptibilities [67].

The work presented in this thesis was carried out in close collaboration with Torben Müller, Jakob Meineke, Henning Moritz and Jean-Philippe Brantut.

2 Ultra-cold gases of fermionic Lithium

Identical atoms in a classical gas occupy energy levels with a probability given by the Boltzmann distribution, which applies whenever the quantum nature of the atomic ensemble can be neglected, i.e. the mean occupation number of energy levels is much smaller than unity. Otherwise, the distribution must take into account the spin degree of freedom of the atom. Atoms with integer or half-integer spin are called bosons and fermions, respectively. For fermions, the occupation of quantum states is restricted by the Pauli exclusion principle [4]: two identical atoms must not populate the same quantum state. When decreasing the temperature T , the occupation probability of the energetically lowest levels gradually increases, finally reaching a state at $T = 0$, where all the lowest levels are occupied with one fermion per spin state, up to Fermi energy E_F . The corresponding temperature is the Fermi temperature $T_F = E_F/k_B$.

In this thesis, a quantum degenerate gas is experimentally realised with fermionic lithium, the lightest fermionic atom in the alkali group. Using modern laser cooling techniques [14], we cool the dilute gas down to temperatures below the Fermi temperature, which is on the order of $1\mu\text{K}$ for our experimental conditions. Despite the fact that the ground state at this temperature is solid, the atomic ensemble remains gaseous due to its low density. For solidification, three-body recombination would be necessary [68]. In this process, two atoms form a molecule by transferring the binding energy to the third atom. However, this process is highly improbable within the time scales of the experiment.

In ultra-cold gases, two-body scattering [69] is the dominant collision process. Here, the spin symmetry of the scattering states plays a key role. The low kinetic energy of the atoms only allows scattering with zero relative angular momentum, implying a symmetric orbital wave-function. Since the total wave-function of two fermions must be anti-symmetric, the spin wave-function must also be anti-symmetric and scattering between two identical fermions is prohibited. The experiments are done with a mixture of two hyper-fine spin states with equal population, where two-body scattering is allowed and evaporative cooling is possible. In this case, the scattering properties are determined by one single parameter, the scattering length a . By making use of the so-

called Feshbach resonance, the scattering length a can be tuned by applying an external magnetic field B [70, 71, 72]. This enables the control of interaction between fermions over a wide range.

At a certain magnetic field, the scattering length can be tuned to zero, thus obtaining a non-interacting Fermi gas [73]. Due to the absence of interaction, such fermionic ensembles are simple to describe quantitatively. For a non-zero scattering length, attractive two-body interactions can cause different kinds of pairing [30, 31, 32]. As pairs of fermions, either weakly bound Cooper pairs [74] or strongly bound molecules, they can be considered as composite bosons. They can occupy the same ground state and form a superfluid state.

In an attractively interacting two-component Fermi gas, there is a phase transition to a superfluid phase below a critical temperature. For weak attractive interactions, fermions form Cooper pairs at the Fermi surface, which is a spherical shell of radius p_F in momentum space, with $E_F = p_F^2/2m$. Since the Fermi energy depends on the atom number N , Cooper pairing is a many-body phenomenon. The corresponding many-body state, consisting of many Cooper pairs, is the Bardeen-Cooper-Schrieffer state [8, 9].

The situation is very different for strong attractive interactions where molecular pairs are formed. Pairing can be described only with two-body physics and depends solely on the scattering length a . Due to the larger binding energy E_b , pairing is much less sensitive to temperature. Such molecular pairs behave like bosons that obey Bose statistics, which allow the occupation of many molecules in one state. Below a critical temperature, a majority of molecules will occupy the absolute ground state and form a Bose-Einstein condensate [1, 2, 3].

With ultra-cold fermions, and in particular with ${}^6\text{Li}$, the tunability of the two-body interaction allows one to study different pairing regimes. In the experimentally accessible regime, fermionic pairs can not simply be described by one of the extreme cases, which are weakly bound Cooper pairs or strongly bound molecules. The corresponding superfluid is neither a BCS-state nor a BEC. This intermediate pairing regime is called BEC-BCS crossover regime. It is characterized by the relative length scale of the pairs, i.e. the ratio between pair size and interatomic distance. Ideally, the size of a Cooper pair is much larger and that of a molecular pair much smaller than the mean interatomic distance. But in this intermediate regime, these length scales are all of the same magnitude. While the molecular pair size is proportional to the scattering length a , the interatomic distance is proportional to the Fermi length scale k_F^{-1} (which is the length corresponding to the Fermi energy E_F). Therefore, the relative pair size can be expressed by $k_F a$, which is also known as the gas parameter. In figure 2.1, fermionic pairing phases and their transition to a superfluid state are illustrated with respect to their relative pair size at the critical temperature.

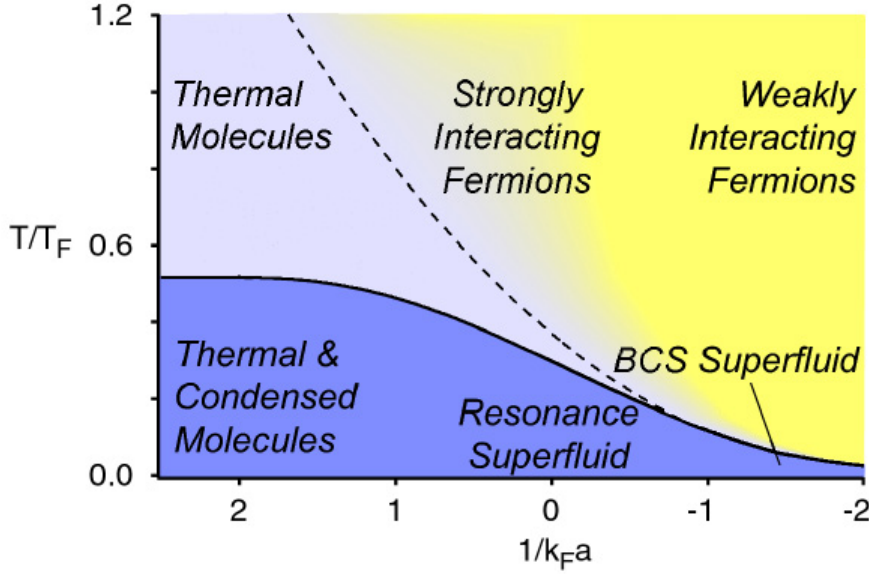


Figure 2.1: Phase diagram of interacting fermi mixtures in a harmonic trap [75, 76]. The scales of the axes are the relative temperature T/T_F and the inverse relative pair size $1/k_F a$. Below the critical temperature at $1/|k_F a| > 1$, the phase diagram shows pairing in a regime where states are approximate a BEC of molecules or a BCS superfluid. The critical temperature of the BCS-state strongly depends on both k_F and a . The critical temperature of the BEC state on the other hand is mainly determined by the Bose statistics of the molecules. The regime $1/|k_F a| \leq 1$ is called the BEC-BCS crossover. There, a distinction between molecules and Cooper pairs becomes irrelevant, the corresponding many-body state is a resonance superfluid. Right at the Feshbach resonance, where $1/|k_F a| = 0$, the system is in the so-called unitary regime. Above the critical temperature at $1/k_F a < 1$, Cooper pairing does not occur because the thermal energy is larger than the binding energy E_b . The fermionic ensemble behaves as an interacting Fermi gas. However, at $1/k_F a > 1$, stable but not condensed molecular pairs exist.

A smooth transition between the BEC and the BCS regime had already been predicted [30, 31, 32, 77], before it was first experimentally observed in the year 2004 [24, 25, 26, 27, 28, 29]. Exploring this regime is of particular interest, because results can be applied to describe systems which are not experimentally accessible. In the unitary regime for example, properties of the Fermi gas become universal. The scattering length a is much larger than any other length scale and interactions need not be considered in the description of the interacting Fermi gas. The system can then be described as a non-interacting Fermi gas [78, 79]: its physical quantities must be proportional to those of a non-interacting Fermi gas with proportionality constants that are universal. The pair size, for example, is proportional to k_F^{-1} .

There are still many open questions about the BEC-BCS crossover regime and the availability of this phase diagram now may prove to be a starting point for a wealth of physical exploration.

2.1 Non-interacting Fermi gas in a harmonic trap

At low temperature, physical quantities of a non-interacting Fermi [68, 75, 80] gas can be derived from the Fermi distribution, which is given by the occupation probability

$$f(E, T) = \frac{1}{e^{(E-\mu(N,T))/k_B T} + 1}, \quad (2.1)$$

of a state with energy E . The chemical potential $\mu(N, T)$ is determined by the total number of atoms N and the temperature T for a given density of states $D(E)$ as

$$N = \int_0^\infty D(E) f(E, T) dE. \quad (2.2)$$

Without knowing details of the Fermi gas, estimates of practical use can be made, if it is assumed that atoms are confined in a potential that can be harmonically approximated and if the temperature is equal to zero. By definition, the chemical potential at zero temperature $\mu(N, 0)$ is called the Fermi energy E_F . If N fermions are now confined in a harmonic potential $V(r)$ with trap frequencies ω_x , ω_y and ω_z , the density of state is $D(E) = E^2/2\hbar^3\omega_x\omega_y\omega_z$. With equation 2.2, the Fermi energy and temperature is then given by

$$E_F = k_B T_F = (N\hbar)^{1/3}\bar{\omega}, \quad (2.3)$$

with $\bar{\omega} = (\omega_x\omega_y\omega_z)^{1/3}$. The particle number N can be estimated from the size of the trapped Fermi gas: in the Thomas-Fermi approximation, the trapping potential term is considered to be much larger than the kinetic energy term, hence the kinetic energy is neglected. The chemical potential $\mu(N, 0) = E_F(N)$ is then equal to the trapping potential $\frac{1}{2}m\omega_i^2 R_{TF,i}^2$ at the maximal extension of the trapped atomic ensemble, the so-called Thomas-Fermi radii $R_{TF,i}$, with $i = x, y, z$. The total atom number can then be estimated to be

$$N \simeq N_{TF} = \frac{1}{\hbar} \left(\frac{1}{2} m \frac{\omega_i^2}{\bar{\omega}} R_{TF,i}^2 \right)^3 \quad (2.4)$$

By inserting the result into equation 2.3, the Fermi energy is obtained.

2.1.1 Density distribution at finite temperature

Many physical quantities of a harmonically trapped Fermi gas are derived from the Fermi distribution $f(T)$. Because the distribution only gradually changes when lowering the temperature T to zero, finite temperature must be taken into account. In experiments with ultra-cold atoms, the temperature of an ensemble is usually extracted from the shape of the density distribution $n(\mathbf{r}, T)$. While the shape of the classical gas is given by a gaussian density distribution $n(\mathbf{r}, T \gg T_F)$, that of a Fermi gas at $T = 0$ is

$$n(\mathbf{r}, T = 0) = \frac{1}{6\pi^2} \left(\frac{2m}{\hbar^2} \right)^{3/2} (E_F - V(\mathbf{r}))^{3/2} \quad (2.5)$$

in a semi-classical approximation. The smooth transition from the classical to the zero-temperature Fermi density distribution stems from the Fermi distribution $f(T)$ and thus reveals the temperature T . The following is an explanation of the method used for determining the temperature from the density distribution.

The density distribution of the atomic ensemble is measured by resonantly illuminating the ensemble, a process commonly known as absorption imaging [38, 75]: Photons are absorbed by the atomic ensemble and the shadow is detected on a CCD camera. From the shadow picture, the integrated atomic density $n_{2D}(\mathbf{r}, T)$ along the illumination axis can be retrieved. Usually the atomic ensemble is small in size and optically so dense that the density distribution cannot be inferred accurately from the shadow picture. The atomic ensemble is therefore often released from the trapping potential before it is illuminated. After expansion, the shape and the optical density, i.e. the shadow of the atomic ensemble, can even be measured with an imaging system of limited optical resolution. The shadow corresponds to the integrated density distribution of the expanded atomic ensemble, resulting in an atomic two-dimensional column distribution $n_{2D}(\mathbf{r}, T, t)$, with an expansion time t . From that density distribution, the initial distribution in trap, $n_{2D}(\mathbf{r}, T, t = 0)$ can be obtained. Following is a description of the relation between the Fermi distribution and the column density $n_{2D}(\mathbf{r}, T)$ to finally obtain the temperature T :

First, the Fermi distribution given in equation 2.1 is expressed by

$$f(\mathbf{r}, \mathbf{p}, T) = \frac{1}{e^{(\frac{\mathbf{p}^2}{2m} + V(\mathbf{r}) - \mu(N, T))/k_B T} + 1}, \quad (2.6)$$

where the energy E is replaced by $\frac{\mathbf{p}^2}{2m} + V(\mathbf{r})$. This is the so-called semi-classical Fermi distribution. By integrating it over \mathbf{p} , one directly obtains the three-dimensional atomic density distribution

$$n(\mathbf{r}, T) = \frac{1}{(2\pi\hbar)^3} \int f(\mathbf{r}, \mathbf{p}, T) d\mathbf{p} = -\frac{1}{\lambda_{dB}^3} Li_{3/2} \left(-e^{(\mu(N,T) - V(\mathbf{r}))/k_B T} \right), \quad (2.7)$$

where $Li_n(s)$ is the n^{th} -order Polylogarithm and $\lambda_{dB} = \sqrt{\frac{2\pi\hbar^2}{mk_B T}}$ is the so-called de Broglie wavelength. From equation 2.7, the density distribution of the expanded atomic ensemble is deduced. Since collisions in a non-interacting Fermi gas can be neglected during expansion from the trapping potential, it can be assumed that the expansion is ballistic: Apart from the size and the amplitude, the distinctive shape of the density distribution remains unchanged over an expansion time t and can still be expressed by the initial density distribution, using scaled variables r' ,

$$n_{2D}(\mathbf{r}, T, t) = n_{2D}(\mathbf{r}', T, 0). \quad (2.8)$$

The scaled variables r'_i are equal to $r_i/b_i(t)$, where $b_i(t)$ are scaling factors that depend on the potential into which atoms are released [81, 82, 83]. The experimentally accessible atomic column density is obtained by integrating the three-dimensional density $n(\mathbf{r}', T, 0)$ along the illumination direction:

$$n_{2D}(x', y', T, 0) = \int n(\mathbf{r}', T, 0) dz = n_{2D,max} Li_2 \left(-e^{-(V(x',y') - \mu)/k_B T} \right) / Li_2(-e^{\mu/k_B T}). \quad (2.9)$$

Usually, the confining potential $V(x', y')$ is assumed to be harmonic. In this approximation, the relative temperature T/T_F (also called the degeneracy parameter), which is a function of the fugacity $e^{\mu/k_B T}$, can finally be obtained. By fitting the column density distribution $n_{2D}(e^{\mu/k_B T})$ to the measured shape of the density distribution, the fugacity can be extracted and the relative temperature is then given by [84]

$$T/T_F = \left(-6 Li_3(-e^{\mu/k_B T}) \right)^{-1/3}. \quad (2.10)$$

In order to obtain an absolute temperature T , the Fermi temperature $T_F(N) = E_F(N)/k_B$, and hence the absolute particle number N , needs to be determined. While the relative temperature measurement only depends on the shape of the detected shadow, the absolute particle number N can only be gained from the absolute depth of the shadow, which is given by the detected photon distribution. Converting this distribution into the exact two dimensional atomic column density distribution $n_{2D}(x', y')$ is a challenging task, because it is sensitive to many experimental parameters. By integrating $n_{2D}(x', y')$ over x' and y' , the atom number N can be obtained. In the case of a harmonic trapping potential, the result can be inserted in equations 2.3, to finally

calculate the Fermi temperature T_F . Since Fermi gases are trapped in potentials with a gaussian shape, the absolute temperature determination in the harmonic approximation overestimates the real temperature. This error is more pronounced the smaller the relative temperature T/T_F is.

2.2 Interaction between atoms

In a simplified physical picture, the scattering process between two atoms can be replaced by an elastic collision between two hard spheres of radius a [85]. Their interaction potential $U(r)$ in relative coordinates is infinitely large for distances $r \leq a$ and is otherwise zero. The whole collision process can be described by one parameter, the so-called impact parameter. This is the distance at which the two spheres would pass if there were no interactions. The total scattering cross section is given by πa^2 . Although this model seems to be too simple to describe scattering of two atoms, as it turns out, it encompasses the essential part of the scattering processes in an ultra-cold gas: The mean interatomic distance is so large that the interaction is dominated by elastic two-body collisions. The interaction potential can be described by a Lennard-Jones potential $U(r)$, which is spherically symmetric and vanishes at large distances, and most important: the scattering process depends only on a single parameter.

The quantum mechanical scattering process is described by probability amplitudes for scattering into a final state with a quantized relative angular momentum [69]. Due to the low collision energy, the parameter, which governs the collision of two atoms, is the probability amplitude of lowest angular momentum. This probability amplitude is proportional to the scattering length a (section 2.2.1). Since the total cross section σ in the quantum mechanical scattering process is $4\pi a^2$, the background scattering length a can be considered as an effective radius a of a hard sphere, which leads us back to the simple classical model.

The collision process of two atoms in an external magnetic field is still governed by the scattering length $a(B)$, which is now a function of the magnetic field B [71]. This magnetic field dependence is due to the interaction potential $U(r)$ that includes the magnetic moment of the two atoms: with the spin degree of freedom, the interaction potential is described by $U_S(r)$ and $U_T(r)$ in a spin singlet or triplet configuration, respectively. By making use of the Zeeman effect [68], the energy difference of the two spin configurations can be tuned via the magnetic field (figure 2.2a). When the energy of a bound state of the singlet interaction potential is close to the energy of the two incoming atoms of the triplet interaction potential, they can virtually populate that bound state. In this case, the scattering length $a(B)$ is resonantly enhanced (section 2.2.2).

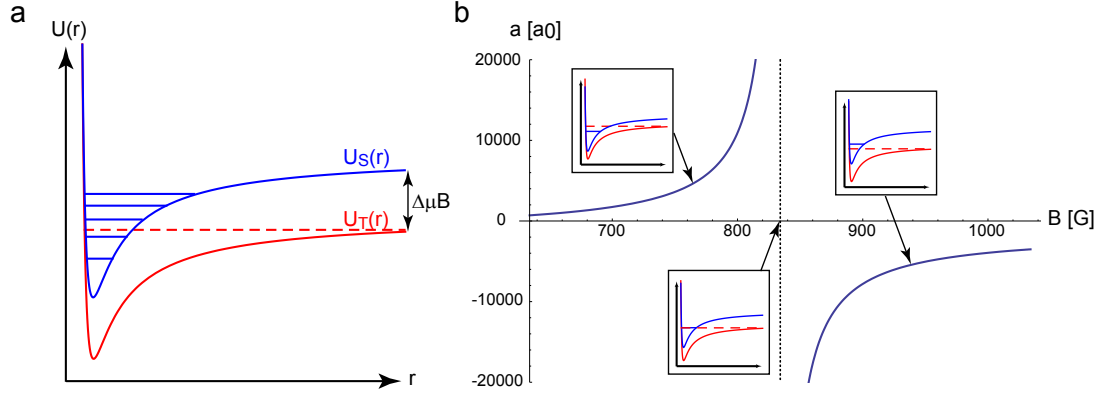


Figure 2.2: a. Lennard-Jones potential $U(r) \sim \frac{1}{r^n} - \frac{1}{r^6}$ of two fermions in a spin triplet (red) and a spin singlet (blue) configuration. Bound state energy levels can be tuned relative to the continuum (dashed line) by the magnetic field B . b. The resonant enhancement of the scattering length $a(B)$ (in units of Bohr radii a_0) depends on the relative position of the bound state and is described by equation 2.11.

In the case of lithium, a coupling between a bound state and the state of the two incoming atoms exists and indeed, resonant enhancement of the scattering length [86, 87] by applying an external magnetic field B (section 2.2.3). The scattering length a can be enhanced to values much larger than the background scattering length a_{bg} in the case of zero coupling:

$$a = a_{bg} \left(1 + \frac{\Delta B}{B - B_{res}} \right). \quad (2.11)$$

Here, the Feshbach resonance [70] is expressed in terms of ΔB and B_{res} representing resonance width and position, respectively. In the picture of two freely scattering atoms, the scattering length $a < 0$ can be attributed to an attractive interaction, which occurs if the bound state is slightly above the continuum energy. Atoms only occupy a virtual bound state. Alternatively, two atoms actually occupy the bound state and form a molecule, even though the scattering length $a > 0$ is attributed to a repulsive interaction in this picture (figure 2.2b). The following is an explanation of how the background scattering length a_{bg} and coupling enter the expression of the effective scattering length a .

2.2.1 Background scattering length

In general, an elastic scattering process of two atoms [69] can be written in relative coordinates r , a relative wave vector $k = \sqrt{mE_0/\hbar^2}$ and a reduced mass m . E_0 is the kinetic energy of the two atoms. The wave function in the far field is described by an

incident plane wave and a spherical wave that is generated during the scattering process with the probability amplitude $f(\theta)$:

$$\psi(\theta, \mathbf{r}) \sim \exp ikz + f(\theta) \frac{\exp ikr}{r}. \quad (2.12)$$

The angle θ is defined by \mathbf{r} and the z -axis, which is the axis of the two incoming atoms. The probability amplitude is called the scattering amplitude. Scattering is caused by a Lennard-Jones potential $U(r)$, which is proportional to r^{-6} at large distances. Because the Lennard-Jones potential is spherically symmetric, the wave-function of scattered particles can be separated into an angular term $f(\theta)$ and radial term $R_{kl}(r)$, which depends on the quantum number of angular momentum l . Because the Lennard-Jones potential can be considered to be short ranged, the scattering amplitude $f(\theta)$ does not depend on details of the potential. The only information about the potential $U(r)$ is revealed by a phase shift δ_l in the radial part of the wave function $R_{kl}(r)$. This phase shift is called scattering phase. In the far field, where the two atoms behave as free particles, their relative radial wave function is then expressed by $R_{kl}(r) = \sin(kr - \frac{\pi}{2} + \delta_l)$. The scattering amplitude $f(\theta)$ is a sum over partial wave scattering amplitudes $f_l(\theta)$ that describe the probability of scattering into a state with relative angular momentum l at an angle θ . Since the partial wave amplitudes scale like $f_l \sim k^{2l}$, only the lowest angular momentum $l = 0$ need to be taken into account in the low energy limit, where $E_0 \sim k^2 \simeq 0$. The partial wave amplitude $f_{l=0}$ in the so-called s -wave scattering does not depend on θ and hence scattering is isotropic. Finally, the relation between the partial wave amplitude f_0 and the background scattering length a is given by $a = -f_0 = \frac{\delta_0}{k}$ and henceforth will be named a_{bg} . So, the background scattering length, which is often considered as an effective atomic radius in the picture of two hard spheres, only depends on one parameter, the relative phase lag $\frac{\delta_0}{2\pi}$ induced by the scattering potential $U(r)$.

2.2.2 Resonantly enhanced scattering length

The background scattering length a_{bg} , set by the scattering phase δ_0 , is constant for a given interatomic scattering potential. However, the situation is different, if a bound state with energy $E_c < 0$, referred to as closed channel $|c\rangle$, enters the interatomic scattering potential. In that case, the background scattering length a_{bg} is resonantly enhanced. This result is obtained by following a derivation of Landau and Lifschitz [69]. There the non-physical assumption is made, that two atoms in the continuum state with energy E_0 , referred to as open channel $|o\rangle$, scatter into the closed channel $|c\rangle$, although the coupling strength γ between the two channels is zero. By assuming smooth boundary condition between the open and the closed channel wave-function, the s -wave scattering amplitude can be expressed by

$$f_0 = -\frac{\hbar}{\sqrt{(m|E_c|)} + i\sqrt{(mE_0)}} = \frac{a_c}{1 + ia_c k}. \quad (2.13)$$

The scattering length, $a_c = \tan \frac{\delta_0}{k}$, simply represents a length scale that corresponds to the energy difference

$$\Delta E = E_0 - E_c = E_0 + |E_c| \simeq |E_c| = \frac{\hbar^2}{ma_c^2}, \quad (2.14)$$

if $E_0 \simeq 0$. The total scattering cross section is then given by

$$\sigma(k) = 4\pi|f_0|^2 = 4\pi\frac{a_c^2}{(1 + a_c^2 k^2)} = 4\pi\frac{\hbar^2}{m\Delta E} \simeq 4\pi a_c^2, \quad (2.15)$$

for $k \rightarrow 0$. The scattering length a_c and the total scattering cross section $\sigma(k)$ diverge if the energy difference ΔE is brought close to zero.

The nature of the scattering cross section changes qualitatively if a_c diverges, because the total scattering cross section depends only on $k \sim \sqrt{E_0}$. An interesting regime is then entered: if k and a_c are replaced by the Fermi wave vector k_F and the effective scattering length a , one obtains the gas parameter $k_F a$ of the Fermi gas. According to the phase diagram in figure 2.1, the scattering cross section $\sigma(k)$ of a Fermi gas at the scattering resonance, $1/k_F a = 0$, is therefore solely determined by the Fermi energy E_F . This is a manifestation of universality [78].

The resonantly enhanced scattering length a_c is only a length scale introduced to demonstrate the basic idea of a resonant enhancement of the scattering length. However, it will turn out that apart from introducing a coupling strength γ , the basic concept for obtaining the real scattering length is not altered and the main aspects of resonant enhancement are already encompassed in the model introduced above.

2.2.3 Feshbach resonance

Only if there is coupling between the open channel $|o\rangle$ and the closed channel $|c\rangle$, the scattering length a is resonantly enhanced. In the case of lithium atoms, there is a coupling between different electronic spin states. Although the total spin $F_{1,2} = S_{1,2} + I_{1,2}$, is a fixed quantity during the scattering process, electronic spin $S_{1,2}$ and nuclear spin $I_{1,2}$ are not separately conserved. Therefore, the electronic spin $S_{1,2} = S_1 + S_2$ can flip from a triplet state T to a singlet state S . Their energy difference $\Delta E(B)$ in a magnetic field B mainly depends on the difference in magnetic moment between the two spin states, given by $\Delta\mu$, which is known as the Zeeman effect. So, the energy threshold

$E_0 = U_T(r = \infty, B)$ of the open channel can be tuned relative to an energy level E_c of the closed channel with the magnetic field B , such that their energy difference is

$$\Delta E(B) = E_0(B) - E_c = (E_0(0) + \Delta\mu B) - E_c. \quad (2.16)$$

With a model presented by Cheng Chin [88], which includes coupling between the two channels $|o\rangle$ and $|c\rangle$, the essential physics of a Feshbach resonance can be quantitatively described. Because in large magnetic fields coupling between electronic and nuclear spin $S_{1,2}$ and $I_{1,2}$ is small relative to the potential depth $U(r)$, eigenstates of the coupled system can be treated in first order perturbation. These are named $|+\rangle \sim \cos(\phi)|o\rangle + \sin(\phi)|c\rangle$ and $|-\rangle \sim -\sin(\phi)|o\rangle + \cos(\phi)|c\rangle$, with a mixing angle $\phi \ll 1$. At distances r which are smaller than the characteristic length r_0 of the potential, the new state of two colliding atoms can be expressed as a superposition of eigenstates

$$|\psi(r < r_0)\rangle = A_+(r)|+\rangle + A_-(r)|-\rangle, \quad (2.17)$$

where the first and second term on the right hand side of the equation are mainly determined by the open and the closed channel, respectively. At large distances $r > r_0$, there is no coupling between the channels and $|\psi(r > r_0)\rangle$ is equal to the asymptotic wave function of the open channel

$$|\psi(r > r_0)\rangle \simeq A_0(a, r)|o(r > r_0)\rangle. \quad (2.18)$$

$|\psi(r > r_0)\rangle$ carries the information of the potential $U(r)$ in the scattering phase δ_0 which determines the effective scattering length a . Therefore A_0 depends on a . $A_c|c(r \geq r_0)\rangle$ must naturally be zero, because the closed channel does not exist at distances $r > r_0$. Again, by assuming smooth boundary conditions between $|\psi(r_{0+})\rangle$ and $|\psi(r_{0-})\rangle$ at r_0 , an equation can be obtained for the effective scattering length a :

$$\frac{1}{-a} = \frac{1}{r_0 - \bar{a}} = \frac{1}{r_0 - \bar{a}_{bg}} - \frac{\hbar^2 \gamma}{\Delta E(B)m}. \quad (2.19)$$

The background and effective scattering length are expressed by $a_{bg} = \bar{a}_{bg} - r_0$ and $a = \bar{a} - r_0$, which are reduced by the characteristic length of the potential. Coupling between open and closed channels is given by γ . With equation 2.14, the energy difference $\Delta E(B)$ can be described by the length $a_c(B)$, which leads to

$$a = a_{bg} \frac{1}{1 + \gamma a_{bg} a_c^2(B)}. \quad (2.20)$$

The effective scattering length a is a function $a(a_{bg}, a_c(B), \gamma)$. It follows from the details of the calculation that the background scattering length a_{bg} is mainly determined

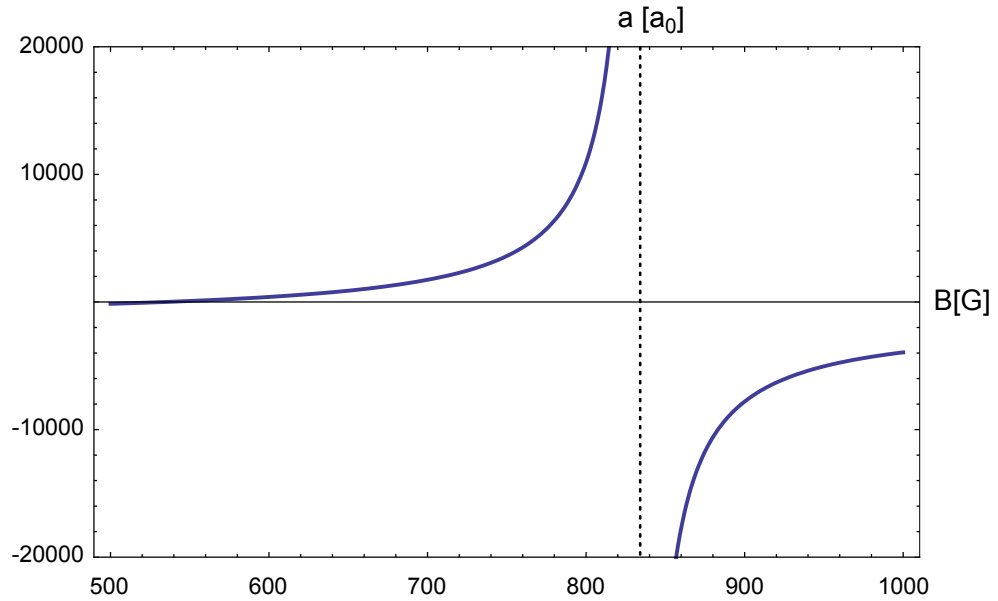


Figure 2.3: The shape of the Feshbach resonance of ${}^6\text{Li}$ at 834G is obtained with the model described [88] and parameters [86] for ΔB and B_{res} , which are $a_{bg} = -1405a_0$, $r_0 = 29.9a_0$, $\gamma^{-1/3} = 101a_0$ and $\Delta\mu = 2.0\mu_B$. The zero-crossing of the scattering length a is at 535G (experimentally obtained value: 528G).

by the constant $A_+(r_0)$, which is dominated by the open channel wave function. This is due to the fact that far off resonance (or without coupling between the two channels), the scattering length is only determined by the shape of potential $U_T(r)$ and therefore $a = a_{bg}$. The last term in equation 2.19, which is given by $\gamma a_c^2(B)$, is determined by $A_-(r_0)$. This coefficient, which is dominated by the closed channel wave function, naturally includes coupling and the relative energy difference to the open channel.

The effective scattering length a at a Feshbach resonance can be expressed as in equation 2.11, with a width $\Delta B = -\Delta\mu^{-1} \left(\frac{\hbar^2}{m} \right) \gamma a_{bg}$ and a resonance position $B_{res} = -\Delta\mu^{-1} \frac{\hbar^2}{ma_c^2} + \Delta B$. In the case of lithium, there is a broad Feshbach resonance [86] at $B_{res} = 834\text{G}$ (figure 2.3). Due to its large width $\Delta B = 300\text{G}$, precise tuning of the scattering length is possible by an experimentally achievable control of the magnetic field. At 528G, there is a zero-crossing [73] that allows one to treat the spin mixture as a non-interacting Fermi gas.

2.3 Fermionic pairs

At the Feshbach resonance, the scattering length a can be tuned such that the two-body interaction leads to pairing. In the case of attractive interaction, pairing is naturally expected, but not necessarily in the case of repulsive interaction. The scattering length a can only be considered as a parameter that characterizes the scattering amplitude in the far field of two free atoms. But as it turns out, a also describes the binding energy and the size of bound pairs. Before going into details of molecular and Cooper pairing, how the scattering length a relates to the pairing mechanism will be explained.

The formation of molecular pairs is observed at a positive scattering length a . Two atoms form a bound state by occupying the highest vibrational energy level of the scattering potential, with a binding energy [88]

$$E_b = -\frac{\hbar^2}{ma^2}. \quad (2.21)$$

This relation is shown in figure 2.4a, where the scaled chemical potential μ/E_F of an interacting Fermi gas at $T = 0$ is plotted against the gas parameter (black dotted line)[75]. At $1/k_F a \gg 1$, the binding energy approximately equals the chemical potential, $\mu \simeq E_b$. These molecules are called Feshbach molecules with a pair size ξ_0 proportional to a (figure 2.4b)[75].

Feshbach molecules can be considered as point-like bosons, if two conditions are fulfilled: the binding energy E_b must be larger than the thermal energy $k_B T$ and the rela-

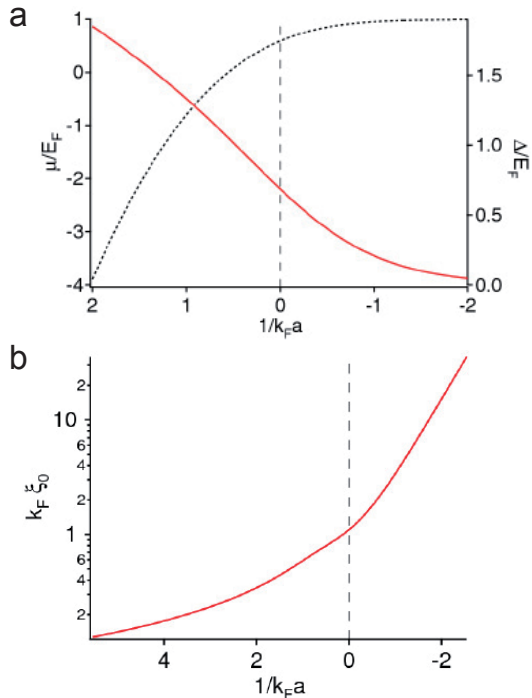


Figure 2.4: Properties of fermionic pairs. a. The scaled chemical potential μ/E_F (black dotted line) and the superfluid gap Δ/E_F (red line) of an interacting Fermi gas in the BEC-BCS crossover regime at $T = 0$ [75]. The superfluid gap Δ of the BCS state is proportional to the binding energy E_b of the Cooper pair. The chemical potential μ of the extreme cases of a BEC at $1/k_F a \gg 1$ is mainly determined by the binding energy of the molecular pairs, $\mu \simeq E_b$; that of a BCS state at $-1/k_F a \gg 1$ is mainly determined by Fermi statistics, $\mu \simeq 2E_F$. b. Pair size $\xi_0 = \sqrt{\frac{\langle \varphi(\mathbf{r}) | \mathbf{r}^2 | \varphi(\mathbf{r}) \rangle}{\langle \varphi(\mathbf{r}) | \varphi(\mathbf{r}) \rangle}}$, with the pair wave function $\varphi(\mathbf{r})$ and the distance \mathbf{r} between the two fermions [75].

tive pair size given by the gas parameter must be small. In the case of bosons, the gas parameter is often expressed by $n_{mol}a_{mol}^3$, with a molecular scattering length $a_{mol} = 0.6a$ [89] and an intermolecular distance $n_{mol}^{-1/3}$. Because such Feshbach molecules follow Bose statistics, they will undergo a phase transition to a Bose-Einstein condensate at a critical temperature T_c . This critical temperature is only determined by the statistics of the Feshbach molecules and is independent of the binding energy E_b .

In the case of attractive interaction, atoms only virtually populate that molecular state, which is attributed to a scattering length $a < 0$. With a gas parameter $-1/k_F a \gg 1$, two atoms can form a Cooper pair [74] with a binding energy

$$E_b = \frac{8}{e^2} E_F e^{-\pi/k_F |a|}, \quad (2.22)$$

if the thermal energy $k_B T$ is smaller than the E_b . The character of a many-body effect is revealed in the binding energy that depends on the two-body scattering length a as well as on the Fermi energy. By including Cooper pairs of all momentum states k , the Bardeen-Cooper-Schrieffer state is obtained [8, 9]. The binding energy E_b of a Cooper pair is proportional to the superfluid gap Δ of the BCS state (figure 2.4a, red line). The binding energy becomes vanishingly small, when tuning the scatter length a to small negative values. It is extremely difficult to access the BCS state with an ultra-cold atomic gas [75] at experimentally achievable temperature. Here, the chemical potential is governed by Fermi statistics. Adding two fermions to the Fermi gas raises the chemical potential by $\mu \simeq 2E_F$ (figure 2.4a, black dotted line), because Cooper pairing occurs at the Fermi surface and the superfluid gap is small. Since only fermions with an energy $E + \delta E$ at the Fermi surface E_F form pairs, the corresponding length scale of pairs is $\xi_0 = 1/\delta k \gg 1/k_F$ (figure 2.4b).

2.4 Molecular Bose-Einstein condensate

The formation of molecules occurs, because two lithium atoms attractively interact by populating the highest vibrational molecular state (the branch of the Feshbach resonance causing repulsion is not accessed). This is a dressed molecular state $|\psi_m\rangle$ that can again be considered as the state of two freely scattering atoms which is perturbed by a molecular bound state [88]. Hence, $|\psi_m\rangle$ is mostly a state of two freely scattering atoms with a small admixture of the molecular state [25]. The spatial extent ξ_0 of this dressed molecular state is much larger than the characteristic length r_0 of the interaction potential [22] and scales with the scattering length a . This long range character $\xi_0 > r_0$ of the Feshbach molecule persists over the whole width of the Feshbach resonance in the case of the lithium around 834G. Close to resonance, Feshbach molecules become extremely large. Despite their large pair size, Feshbach molecules are stable [52, 90,

91]. The two main decay processes — relaxation into a deeply bound molecule and dissociation induced by collisions — are highly suppressed [89]. The first is improbable, because the wave function of the Feshbach molecules has little overlap with the one of deeply bound molecules. Only far removed from resonance, is relaxation enhanced due to the smaller size of the molecules. There, the lifetime of the atomic ensembles is limited because the relaxation processes cause heating. The second decay process is the dissociation of molecules. There, two fermions would transfer their binding energy to a close nearby third. However this process is largely suppressed due to the Pauli exclusion principle and the low density. At low temperatures collision rates between molecules scale as $(T/T_F)^2$ [16, 89]. Therefore, Feshbach molecules are good candidates for stable molecules at low temperatures.

In the following, molecules are considered as composite bosons. In order to explain the phase transition to a Bose-Einstein condensate, it is assumed that the molecules do not interact. But since composite bosons do actually interact with a scattering length a_{mol} , the physically more relevant case of an interacting Bose-Einstein condensate will be described later.

2.4.1 The non-interacting Bose-Einstein condensate

Bosons consisting of two fermions have integer spin and are described by a symmetric wave-function. This implies that more than one boson can occupy the same state. Below a critical temperature, the energy of the bosonic ensemble is so low that the majority of the bosons populate the ground state, and hence they can be described by one and the same wave-function. Bosons populating this wave-function form a Bose-Einstein condensate [68].

Again, at low temperatures physical quantities can only be deduced from the Bose distribution, which is given by the occupation probability

$$f_B(E, T) = \frac{1}{e^{(E-\mu(N,T))/k_B T} - 1} \quad (2.23)$$

of a state with energy E . The chemical potential μ is set by the condition that, after summing over all possible energy levels, the total particle number N must be obtained:

$$N = \int_0^\infty D(E) f_B(E, T) dE. \quad (2.24)$$

Since the particle number N cannot be negative, the chemical potential μ must always be smaller than the lowest energy level $E_0 = 0$.

Here, we assume that the trapping potential can be approximated by a harmonic

potential with a density of states $D(E) = E^2/2(\hbar\bar{\omega})^3$ and $\bar{\omega} = (\omega_x\omega_y\omega_z)^{1/3}$. At the critical temperature T_c , when bosons start to populate the ground state with energy E_0 , the chemical potential approaches zero. When decreasing the temperature T further, below T_c , the chemical potential remains zero and the particle number $N(T < T_c)$ obtained from equation 2.24 becomes smaller than the actual total particle N :

$$N(T < T_c) < N = N(T_c) = \zeta(3) \left(\frac{k_B T_c}{\hbar\bar{\omega}} \right)^3, \quad (2.25)$$

where $\zeta(3) = 1.202$ is the Riemann zeta function. The $N_0 = N - N(T < T_c)$ "missing" bosons will occupy the ground state E_0 , which is obviously not accounted for in equation 2.24, since the density of states $D(E_0 = 0)$ is zero. These bosons condense to a so-called Bose-Einstein condensate. Their relative number as a function of temperature is given by

$$\frac{N_0}{N} = 1 + \left(\frac{T}{T_c} \right)^3. \quad (2.26)$$

Since all condensed bosons occupy the same ground state, they can be expressed by a single particle wave function

$$\Phi(\mathbf{r}) = \sqrt{N_0}\phi(\mathbf{r}), \quad (2.27)$$

with $N_0 = \int n_0(\mathbf{r})d^3r = \int |\Phi(\mathbf{r})|^2d^3r$. A Bose-Einstein condensate can be considered as a coherent matter wave revealing similar interference phenomena (first order correlation) and statistics (second order correlation) as those of a coherent light wave.

2.4.2 The interacting Bose-Einstein condensate at $T = 0$

Although the non-interacting Bose gas is useful for understanding the condensation process, the approximation of zero interaction does not apply to a Bose-Einstein condensate of Feshbach molecules. Since the intermolecular scattering length given by $a_{mol} = 0.6a$ [89], cannot be neglected, interactions must be taken into account. As long as interactions can be considered weak ($n_{mol}^{-1/3} a_{mol} \ll 1$), the ground state wave function of an interacting Bose-Einstein condensate (see [68] and references therein) can be calculated in a relatively simple way with only one additional energy term, the mean-field interaction term

$$U(\mathbf{r}) = n_{mol}(\mathbf{r}) \frac{4\pi\hbar^2 a_{mol}}{2m} = n_{mol}(\mathbf{r})g. \quad (2.28)$$

At zero temperature, the ground state can again be expressed by a single particle wave function, whose main difference in shape is its larger width. This broadening, which leads to a reduction of the mean density, is caused by the mean-field energy term U : the total energy of the ground state is minimized by reducing a mean-field interaction energy, which is proportional to the mean density, at the cost of a higher potential energy. Despite the similarity in description, there is an important qualitative difference between the interacting and the non-interacting case: due to this additional interaction energy term, the excitation spectrum of the interacting BEC changes such that, below a critical velocity, it cannot be excited. Therefore, the interacting BEC behaves as a superfluid - a fluid with frictionless motion. The determination of the ground state wave function in the mean field approximation is briefly outlined in the following.

The substitution of two-body interactions through one mean-field energy term allows one again to treat the many-body wave function $\Phi(\mathbf{r}_1, \dots, \mathbf{r}_{N_0})$ as an actual single particle wave function $\Phi(\mathbf{r})$ (equation 2.27), where it is assumed that all molecules occupy the same ground state. But since $\Phi(\mathbf{r})$ depends on $n_{mol}(\mathbf{r}) = n_0(\mathbf{r}) = |\Phi(\mathbf{r})|^2$ via the mean-field term $U(\mathbf{r})$, a solution has to be found in a self-consistent way. In order to obtain the ground state wave function $\Phi(\mathbf{r})$, its energy is minimized under the constraint that the molecule number N_0 is conserved. This leads to the non linear Schrödinger equation, the so-called Gross-Pitaevski equation

$$\left(-\frac{\hbar^2}{2m} \nabla^2 + V(\mathbf{r}) + gN_0|\phi(\mathbf{r})|^2 \right) \phi(\mathbf{r}) = \mu\phi(\mathbf{r}). \quad (2.29)$$

The non linearity is caused by the mean-field interaction term $g|\Phi(\mathbf{r})|^2 = gN_0|\phi(\mathbf{r})|^2$. The eigenvalue μ is the chemical potential of the molecules, which does not include their binding energy. For a given external potential $V(\mathbf{r})$, the single particle ground state wave function $\phi(\mathbf{r})$ can numerically be computed.

A practical alternative to obtain an approximated ground state wave function without computation is the Thomas-Fermi approximation. This simplifies the Gross-Pitaevski equation by dropping the kinetic energy term in equation 2.29. This assumption only holds if the mean field interaction term $g|n(\mathbf{r})| \sim gN_0/R^3$ is much larger than the kinetic energy term, which can be estimated to be $\hbar^2/2mR^2$, where R is the size of the cloud. The criterion for a valid Thomas-Fermi approximation [68] is often expressed by

$$N_0 a_{mol}/a_{osc} \gg 1, \quad (2.30)$$

since the ground state of the potential $V(\mathbf{r})$ can be treated as a harmonic potential with an oscillator length $a_{osc} = (\hbar/m\bar{\omega})^{1/2}$ and an energy of approximately $1/2m\bar{\omega}^2 R^2$.

The Thomas-Fermi density profile $n_{TF}(\mathbf{r}) = N_0|\phi_{TF}(\mathbf{r})|^2$ is an analytical solution of the equation

$$V(\mathbf{r}) + gN_0|\phi_{TF}(\mathbf{r})|^2 = \mu_{TF} \quad (2.31)$$

for $\mu_{TF} \geq V(\mathbf{r})$. In the harmonic approximation, $n_{TF}(\mathbf{r})$ has the shape of an inverted parabola

$$n_{TF}(\mathbf{r}) = \text{max} \left(\frac{\mu_{TF} - V(\mathbf{r})}{g}, 0 \right). \quad (2.32)$$

In experiments, the density distribution reveals a bimodal, i.e. gaussian and parabolic, shape, when lowering the temperature T below T_c . Thermal molecules contribute to the gaussian density distribution. From the ratio between the gaussian and parabolic contribution, the condensate fraction N_0/N , the number of condensed molecules N_0 as well as the relative temperature T/T_c (equation 2.26) is obtained.

In the Thomas-Fermi approximation, the chemical potential μ_{TF} of condensed molecules can be calculated with the normalization condition $\int n_{TF}(\mathbf{r})d^3r$ and equation 2.32:

$$\mu_{TF} = \frac{\hbar\bar{\omega}}{2} \left(\frac{15N_0a_{mol}}{a_{osc}} \right)^{2/5}. \quad (2.33)$$

This leads to the Thomas-Fermi radius of the Bose-Einstein condensate $R_{TF,i}$, which is determined by the length r , where the density $n_{TF}(\mathbf{r})$ vanishes:

$$R_{TF,i} = \sqrt{\left(\frac{2\mu_{TF}}{m\omega_i^2} \right)} = a_{osc,i} \left(\frac{15N_0a_{mol}}{a_{osc}} \right)^{1/5} \left(\frac{\bar{\omega}}{\omega_i} \right)^{1/2}. \quad (2.34)$$

In conclusion, we have obtained an expression that relates the scattering length a_{mol} and hence the mean field energy to the broadening of the density distribution $n_{TF}(\mathbf{r}) = N_0\phi_{TF}^2(\mathbf{r})$.

2.5 Bardeen-Cooper-Schrieffer state

Fermions with weak attractive interaction g undergo a phase transition to a superfluid — the BCS state — at a critical temperature T_c . Due to pairing of fermions, the total energy of the system is decreased. The basic idea of this pair formation can be explained with the Cooper problem [74]. There, two attractively interacting fermions are added to a non-interacting Fermi sea in the ground state at $T = 0$. The new ground state is then given by a Fermi sea and two fermions of opposite spin and momenta

$\hbar k_1 = -\hbar k_2$. While the new ground state energy of non-interaction fermions equals E_F , the two attractively interacting fermions decrease the total energy below E_F if they form a Cooper pair. The following is a brief outline of how pairing leads to this decrease in energy [92].

The two fermions are described by a two-body wave-function $\varphi(r)$. If pairing occurs, $\varphi(r)$ should not vanish for small relative distances $r = r_1 - r_2$, hence the wave-function must be symmetric and is expressed by $\varphi(r) \simeq \sum_{k > k_F} \alpha(k) \cos(kr)$. If this wave function is inserted into the interaction Hamiltonian

$$\left(-\frac{\hbar^2}{m}\nabla^2 + g\right)\varphi(r) = E\varphi(r), \quad (2.35)$$

and transformed into momentum space, one obtains an equation that relates the interaction g to the energy E of the two-body wave function:

$$\frac{1}{g} = D(E_F) \int_{E_F}^{E_F + E_r} \frac{1}{\epsilon - E} d\epsilon. \quad (2.36)$$

$\epsilon(k) = \hbar^2 k^2/m$ is the kinetic energy of two free fermions, which must be larger than E_F and smaller than $E_F + E_r$. $E_r = \hbar^2/mr^2$ is the energy needed to confine two fermions to a pair of size r . At zero temperature, the Fermi surface is a sharp boundary between occupied and unoccupied states. Hence one can assume that the density of states $D(E_F) = \frac{mk_F}{2\pi^2\hbar^2}$ [75] is constant at the Fermi surface. Integrating the right side of equation 2.36 leads to an expression that can be approximated to

$$E \simeq 2E_F - 2E_r e^{-2/D(E_F)g} \quad (2.37)$$

in the case of weak interactions where $D(E_F)|g| = k_F|a|/\pi \ll 1$. The energy E of the two-body wave function is actually smaller than E_F and hence it can be considered as a bound state at the Fermi surface — a Cooper pair. This conclusion was a crucial step in explaining the superfluidity of fermions. In the case of electrons in a metal, it could be shown that electrons resonantly interact with the ion crystal of the solid and interactions can indeed be attractive.

Unlike in the case of the Cooper problem, all fermion pairs are included in the problem of finally obtaining the BCS state [8, 9]. The original description of a superfluid is given by the phenomenological Ginzburg-Landau equation, which introduces a superfluid wave function as a classical field in the same way that the Gross-Pitaevski equation does. However, in a microscopic description, superfluidity can be explained directly as a many-body state of Cooper pairs, which gives more insight in the pairing mechanism. Bardeen, Cooper and Schrieffer first introduced a Hamilton operator to describe a superfluid that only consists of Cooper pairs:

$$H_{cp} = \sum_{k,s} \epsilon_k c_{k,s}^\dagger c_{k,s} + \sum_{k,k'} g_{k,k'} c_{k\uparrow}^\dagger c_{-k\downarrow}^\dagger c_{k'\downarrow} c_{k'\uparrow}. \quad (2.38)$$

The creation and annihilation operator for a spin up or spin down fermion with momentum k is expressed by $c_{k,\uparrow(\downarrow)}^\dagger$ and $c_{k,\uparrow(\downarrow)}$. The ground state of this Hamiltonian is the BCS state

$$|\Phi_{BCS}\rangle = \prod_k (|u_k + v_k c_{k\uparrow}^\dagger c_{-k\downarrow}^\dagger|0\rangle). \quad (2.39)$$

The probabilities $|v_k|^2$ and $|u_k|^2$ (with $|u_k|^2 + |v_k|^2 = 1$) determine if a Cooper pair does or does not occupy state k , respectively. The superfluid gap at zero temperature is close to the result for the binding energy of a Cooper pair and is given by

$$\Delta = \frac{8}{e^2} E_F e^{-\pi/2k_F|a|} \quad (2.40)$$

The critical temperature of the phase transition is proportional to the superfluid gap:

$$T_c = \frac{e^\chi}{\pi} \Delta, \quad (2.41)$$

with $\chi = 1.78$. The shape of the density distribution $n_{BCS}(\mathbf{r})$, from which the temperature T is experimentally inferred, is very similar to that of a normal Fermi gas. There are differences, but they are difficult to detect.

2.6 Crossover from BEC to BCS

A connection between the two regimes of a Bose-Einstein condensate of tightly bound molecules and a BCS state of weakly bound Cooper pairs had already been proposed by Eagles [30], when Leggett showed in 1980 [31], that there exists a smooth crossover in many-body systems, where pairing dominated by two-body physics in real space evolves into a state with pairing in momentum space.

While the BCS state, which is the one extreme case of superfluidity due to pairing in momentum space with $k_F a \rightarrow 0_-$, was experimentally observed in a superconductor already in 1911, it took until 1995 for the first realisation of a weakly interacting BEC [10, 11, 12, 13]. This finding represents the other extreme case, where bosons can be considered as extremely tightly bound fermions ($k_F a \rightarrow 0_+$), which are electrons bound to the nucleus [93]. Examples of the crossover regime are superfluid ^3He , observed in 1972 [94] and high temperature superconductivity, which was not known until 1986 [95].

Although each of these observations was a major milestone in exploring the phenomena of superfluidity and superconductivity, the interaction U between fermions in none of these systems could be tuned, so that BEC-BCS crossover could only be accessed by comparing the different systems. The situation changed in 2004 with the first observation of an ensemble of ultra-cold atomic gas of resonantly interacting fermions [24, 25, 26, 27, 28, 29]. By accessing a Feshbach resonance, the scattering length $a(B)$ could be tuned via the magnetic field B such that finally, the entire crossover and also a part of the BEC-regime could be approached by experimenters with a single system.

Nozières and Schmitt-Rink [32], who extended Leggett's model for finite temperatures T , found expressions for the superfluid gap Δ and the critical temperature T_c for the two limiting cases of a BCS state and a molecular Bose-Einstein condensate, which are given by

$$\Delta_{BCS} = \frac{8}{e^2} E_F e^{-\pi/2k_F|a|} \quad (2.42)$$

and

$$\Delta_{BEC} \simeq \frac{E_F}{\sqrt{k_F a}}, \quad (2.43)$$

respectively. The critical temperature for a harmonically trapped Fermi gas is

$$T_{c,BCS} \sim \Delta_{BCS} \quad (2.44)$$

and

$$T_{c,BEC} \sim 0.55T_F = 0.55E_F/k_B. \quad (2.45)$$

While the critical temperature for a BCS state is proportional to the superfluid gap Δ_{BCS} , that of a molecular Bose-Einstein condensate only depends on the Fermi temperature T_F , which is reached when the ground state starts to be populated by molecules.

Since the first observation of a resonantly interacting Fermions with tunable interaction strength U , the progress in this field has been rapid. In 2003, molecular Bose-Einstein condensation was first observed [17, 18, 19] and the pairing gap at different positions in the BEC-BCS crossover was measured [20, 22]. Already in 2005, a vortex pattern in the atomic cloud could be observed, which can be considered as proof for superfluidity in this parameter regime [23]. Different thermodynamic variables, such as the heat capacity [96] and the entropy [97, 98] have also been measured.

Another research field has opened, where experiments with ultra-cold fermionic ensembles of imbalanced spin population have been performed. These atomic ensembles

consist of a two component spin mixture of hyper-fine spin states, whose ratio is unequal to one. This additional degree of freedom in the spin population is new. Before these findings a spin imbalance in conventional superconductors could only have been created by applying a external magnetic field. But according to the Meissner-Ochsenfeld effect [99], this is impossible, since magnetic fields are suppressed inside a superconductor. It has also been shown that in a trapped Fermi gas with imbalanced spin population, the excess fermions of majority spin component are separated from the superfluid core. This phase separation has been observed in the entire BEC-BCS crossover [33, 35, 100].

3 Design of the experimental apparatus

The main challenge in designing the experimental apparatus presented here, was to combine cooling and trapping techniques to obtain Fermi gases below Fermi temperature and high resolution microscopy. To reach temperatures near $1\mu\text{K}$, the atomic ensemble must be kept in a thermally well-insulated environment. This is achieved by reducing the ambient pressure to avoid collisions with atoms of the background gas. All experiments with ultra-cold atoms are carried out in an ultra-high vacuum [UHV] environment, where pressures of 10^{-11}mbar are maintained. Inside the vacuum chamber, the lifetime of an ultra-cold atomic ensemble is extended to more than one minute.

The atoms inside the vacuum chamber are manipulated with magnetic fields and laser light. Space consuming magnetic field coils and optical viewports are placed around the vacuum chamber. The design is such that optical access, which might be needed in the future, is not obstructed. In addition, the construction of the apparatus must be extremely stable, so that vibrations or long term drifts, which would jeopardize the maximally allowed mounting tolerances of the microscope objectives, can be suppressed.

In our case, however, not only is the optical access for the two microscope objectives obstructed at the location where atoms are initially trapped and cooled, but large switching magnetic fields inducing eddy currents also would cause vibrations. Therefore, the atomic ensemble is transported into a glass cell that offers high optical access and a surrounding with non-conducting materials. The transport of the atoms is done with a moveable optical dipole trap, a tweezer, that does not again obstruct the optical access so gained. In the final position, which is in the center of a glass cell, microscopy of the atomic ensemble is carried out.

Components of the experimental apparatus are introduced here in the order of the general cooling procedure and explanations focus on design and technical aspects. First, an overview of all components is given in the following section.

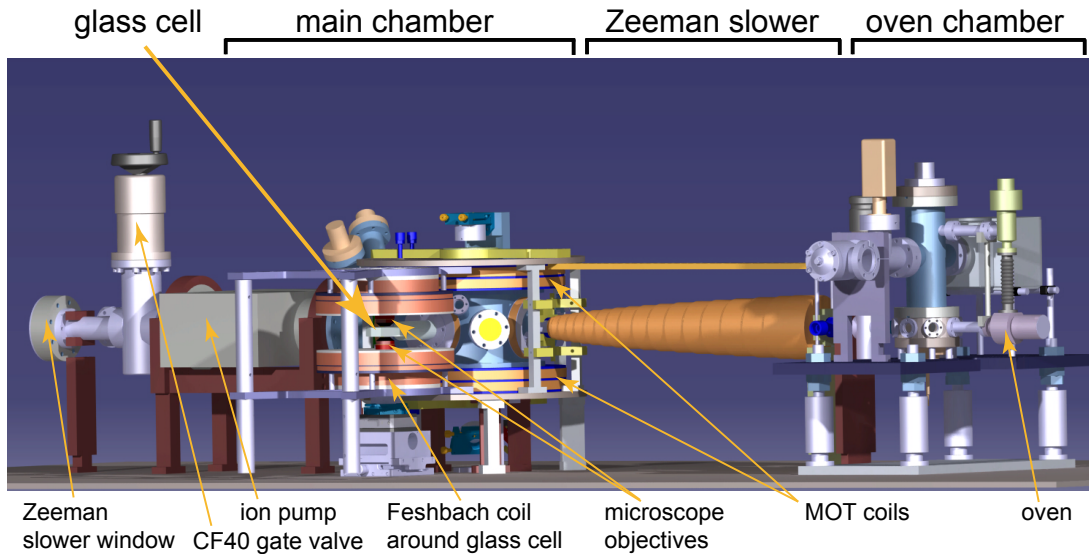


Figure 3.1: Overview of the experimental apparatus showing the four sections: Oven chamber, Zeeman slower, main chamber and glass cell. The overall length of the apparatus is 2.2m (optics and optical breadboards obscuring the apparatus are not shown). The heart of the experiment is the glass cell with two microscope objectives above and below, embedded between large magnetic field coils.

3.1 Overview of the experimental setup

The vacuum chamber with surrounding and incorporated magnetic field coils and optics can be separated into four sections: The oven chamber, where an atomic beam is produced, the Zeeman slower that decelerates the atoms, the main chamber, in which atoms are trapped and cooled with different optical techniques, and the glass cell, where experiments are finally carried out (figure 3.1).

In the oven chamber, the two main components for the lithium beam production are the oven itself and two apertures. The oven is used to heat and evaporate lithium atoms, while the two apertures collimate the evaporated atoms to a beam. A high oven temperature not only raises the partial pressure of lithium, but also the pressure of the background gas. In order to maintain vacuum conditions in the main chamber at 10^{-11} mbar, the two chambers are partly separated. They are only connected by a small, differential pumping tube and only the collimated lithium beam enters the main chamber.

A Zeeman slower, consisting of a cone shaped magnetic field coil and a laser beam entering through a viewport at the other end of the main chamber, slows the beam down, before atoms approach the magneto-optical trapping region.

The atoms of the decelerated beam are then trapped in a magneto-optical trap [MOT]

located at the center of the main chamber. With three orthogonal pairs of counter-propagating laser beams, which are transmitted through six viewports, and two large magnetic field coils, which create a quadrupole field, atoms are trapped and cooled. Further cooling of the atoms is done in an optical dipole trap that about matches the trap volume of the magneto-optical trap. Such a dipole trap can only be realized with sufficiently large laser light intensities which we generate by making use of the intensity enhancement achieved inside an optical resonator. Here, this optical resonator is placed into the vacuum chamber. By lowering the intensity inside the optical resonator, the depth of the standing wave dipole potential decreases and atoms are evaporatively cooled. Because atoms can only be evaporated at certain magnetic fields, so-called Feshbach coils at the center of the main chamber and the glass cell are installed. The pre-cooled atomic ensemble is then loaded into a smaller running wave dipole trap and transported to the glass cell.

The glass cell can be considered as the science chamber. There, the last evaporation step takes place to reach the final temperature and experiments are carried out: micro dipole potentials are created and ultra-cold ensembles of fermionic lithium are imaged with high resolution by employing two microscope objectives.

3.2 Oven chamber

A new ensemble of ultra-cold atoms is prepared in each experimental sequence since the applied measurement techniques are destructive. For efficient operation of the experimental apparatus, the one isotope of interest must be cooled and trapped within seconds without contaminating the vacuum system.

Here, a lithium reservoir, which is part of the oven, is heated to achieve a high partial pressure. Because commercially available lithium is not perfectly clean, the overall pressure in the oven can rise to approximately 10^{-5} mbar. Atoms are evaporated from the oven nozzle into the pumping chamber, where the pressure is $8 \cdot 10^{-10}$ mbar. The pumping chamber is connected to the main chamber by a differential pumping tube that assures a maximal pressure ratio of 10^{-4} ; enough to maintain a pressure below $1.8 \cdot 10^{-11}$ mbar in the main chamber. Only a lithium beam passes through this tube.

The oven creates a flux and two apertures placed in the pumping chamber collimate the evaporated atoms to a beam. Since the pumping and the main chamber are partly separated during operation and totally separated by a gate valve during oven service, vacuum conditions in each chamber are independently maintained by different pumps. An overview of the oven chamber consisting of the oven and the pumping chamber is shown in figure 3.2.

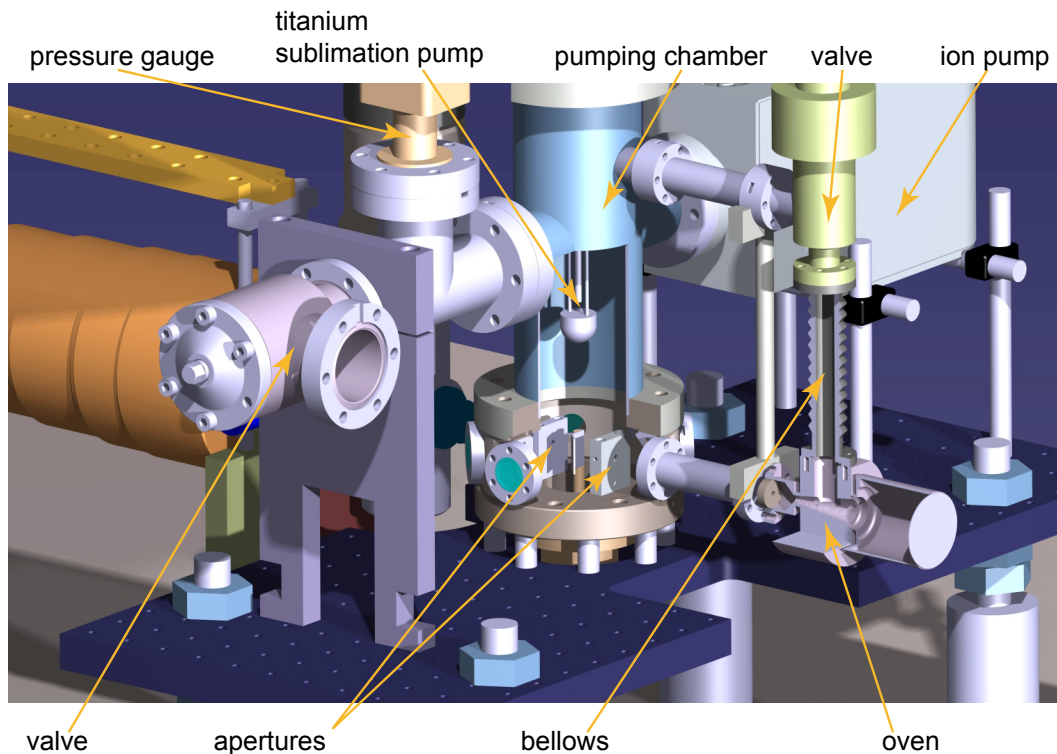


Figure 3.2: Overview of the oven chamber, which is illustrated as a partially cut CAD drawing. The oven chamber consists of a pumping chamber and the oven, which are mounted on an adjustable table. The main components of the pumping chamber are the two apertures, pumps and valves for initial pump-down.

3.2.1 Atomic beam and oven design

When designing an oven, a geometry has to be found to ensure efficient heating of the lithium reservoir, while contamination of the pumping chamber, i.e. the increase of background pressure, is sufficiently low. Furthermore, lithium atoms emanated from the oven should be efficiently collimated to a beam.

For a fixed geometry of oven nozzle and apertures, the flux of the lithium beam is proportional to the emission rate of atoms from the oven. Since the emission rate is given by the partial vapor pressure of lithium $p_{Li}(T)$ [101], the flux can be adjusted by tuning the oven temperature. With increasing temperature, the mean atomic velocity of the Boltzmann distribution simultaneously also increases. Since a Zeeman slower only allows deceleration of atoms below certain threshold velocity v_{th} , the percentage of atoms, that can still be brought to standstill will drop. Hence, the product of the lithium flux and the percentage of lithium atoms that can be decelerated results in an effective lithium flux.

The ratio between emitted lithium atoms and those collimated to a beam is set by the design of the oven, the geometry of the oven nozzle and the two apertures. Simply increasing the temperature would indeed increase the effective flux, but it would also lead to a higher pressure in the pumping chamber. If the pressure ratio between main and pumping chamber were larger than 10^{-4} , the pressure in the main chamber would increase. In addition, a higher percentage of lithium atoms which cannot be decelerated would only enhance collisions with trapped lithium atoms. Eventually, viewports would be reflection-coated with lithium much faster, especially the one used for the slowing laser beam, which is counter-propagating to the atomic beam. Although oven and apertures have been described as separate components, their exact setting determines how efficient evaporated atoms are collimated to a beam.

Ideally, a small diameter nozzle that generates a lithium beam of already low angular divergence, should be placed as close as possible to the apertures. The temperature of the nozzle is above the 180°C melting point of lithium to make sure that the nozzle is not obstructed by recondensed, solid lithium. Furthermore, the lithium reservoir is heated to a temperature of about 400°C to achieve a partial vapor pressure of approximately 10^{-5}mbar . Because the temperature, and hence pressure inside the pumping chamber, must not be increased by heating the oven, nothing but very good thermal insulation between oven and pumping chamber prevents the latter from being contaminated. For this reason there are limitations on how compact the design can be.

A cut through the oven is shown in figure 3.3. The oven consists of a heated cylindrical reservoir, a conical reflux stage — intended to bring condensed lithium atoms back to the reservoir, and a heatable nozzle [102]. The entire oven is custom machined and welded out of a block of special stainless steel (type 1.4429), which is suitable for high temperatures and highly reactive materials. Nickel gaskets were used to avoid corrosion and leakage.

The cylinder is filled with approximately 3g of enriched ^6Li , which is evaporated at a temperature of 402°C . The fraction that does not pass through the nozzle will condense in the conical reflux region at a temperature of 267°C . Here capillary wells are eroded along the cone axis to let lithium flow to regions of higher temperature. Furthermore, the cylindrical reservoir is covered by a thin mesh to facilitate the reflux of condensed, fluid lithium to the hottest region due to the capillary effect [102].

To prevent liquid lithium from reaching the nickel gasket and possibly causing corrosion, a protection barrier is inserted, effectively forming a reservoir for superfluous Lithium. Both, the nozzle and the oven temperature (300°C / 402°C) determine the flux. The cylindrical reservoir and the nozzle are heated by a copper collar onto which a thermocoax cable has been wound. The required heating power is 51W and 16W, respectively. On the outside of the reservoir and the nozzle, fibreglass fabric is used

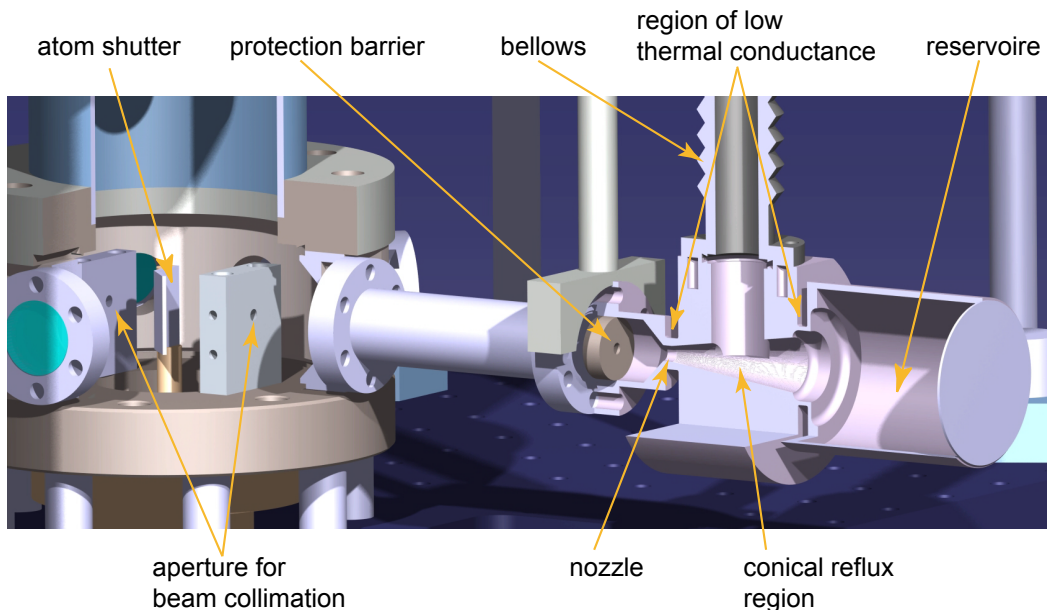


Figure 3.3: A cut through the oven and neighboring components. The thin-walled transition regions between the cylindrical reservoir, the conical reflux section and the nozzle have low thermal conductivity to be able to heat the three sections independently. The lithium beam passes through a 75mm long vacuum tube and is then collimated by the two apertures. The bellows attached to the oven vertically are only used for the initial pump-down.

for thermal insulation. The conical region is neither heated nor insulated, leading to a significant drop in temperature.

3.2.2 Pumping chamber design

The lithium beam produced in the pumping chamber passes through the differential pumping tube, which is 145mm long with an inner diameter of 3mm and connects to the Zeeman slower. The pumping chamber is designed such that direction and position of the lithium beam can be precisely adjusted. An overview of the oven chamber, including the oven and the pumping chamber is shown in figure 3.2.

Two 3mm apertures in the center of the oven chamber collimate the divergent flux coming from the nozzle. In order to maximize the number of atoms transmitted through the differential pumping tube, the angle and position of the collimated lithium beam can be adjusted using different adjustment nuts and screws that move the whole oven chamber. To provide the flexibility necessary for the movement of the oven chamber

relative to the Zeeman slower, the vacuum components are connected via short bellows. Between the two apertures, a mechanical shutter can interrupt the atomic beam.

The oven is connected to the pumping chamber via two ports. The horizontal one is connected to a 75mm long tube that provides additional thermal insulation. The temperature at end of that tube is below the melting point of lithium so that lithium contamination of the nickel gasket at the center piece of the pumping chamber is not possible. The vertical port is connected to a valve, which is open during the initial pump-down of the oven and the bake out. This is primarily done to enhance the pumping of hydrogen, whose partial pressure dominates the background pressure in the oven. Auxiliary components needed to create and maintain ultra-high vacuum [103] are a valve only opened during initial pump-down, a 20l/s ion-getter pump and a titanium sublimation pump. The pressure is measured by a combined Pirani/hot cathode UHV pressure gauge. In the case of oven replacement, a gate valve can be closed to totally disconnect the main chamber from the oven chamber.

3.2.3 Installation

Lithium is a highly reactive material. It oxidizes instantly and burns provided that the humidity is high. Certain precautions have to be made to fill and install a lithium oven properly. Prior to filling, lithium is cleaned with acetone and cut in smaller pieces under an argon atmosphere. Then the oven is sealed. Next, the oven chamber, to which the oven has not yet been connected, is evacuated to remove nitrogen and oxygen and is then floated with high purity argon at a slight overpressure. The two CF16 blind flanges at the end of the bellows and the rear side of the eight port cylinder are removed allowing the argon to flow out. The oven is then bolted to the cylinder and to the bellows, before the whole chamber is evacuated again. The oven chamber was baked out at about 200°C for seven days, while the oven was baked out at about 560°C for about 12 hours. Such high bake out temperatures are needed to remove any residual hydrogen that will contaminate lithium. As for other vacuum components, the temperature difference between bake out and operation temperature is about 200°C. During bake out, the top valve to the oven is left open for efficient pumping of the oven and later closed during operation. After sublimating titanium, an operating pressure of about $8 \cdot 10^{-10}$ mbar was achieved.

3.3 Zeeman slower

The lithium beam produced in the oven chamber would enter the main chamber at a longitudinal velocity of more than a 1000m/s, but only atoms up to a maximum velocity of about 60m/s can be magneto-optically trapped. Here a (decreasing magnetic field)

Zeeman slower [59] consisting of a laser beam and a cone shaped magnetic field coil is employed to decelerate atoms. In the following, the general deceleration process is explained, before the design of the magnetic field coil and the characteristics of the laser beam is discussed.

The basic idea of a Zeeman slower is to decelerate atoms by means of resonant light forces [14]. Atoms propagate in the opposite direction to a laser beam and resonantly scatter photons. Photon momentum is transferred to the atom and then randomly distributed by spontaneous emission. The resulting net force decelerates the atom. Because of the Doppler effect, the effective resonance frequency of the atoms in the lab frame changes as they are decelerated. Atoms are kept in resonance with the slowing laser beam by exploiting the Zeeman effect: the transition frequency of the atom is tuned by applying an external magnetic field B in such a way that the resonance condition is fulfilled for all velocities.

Here, the magnetic field coil of a Zeeman slower is designed such that the frequency shift caused by the Doppler effect is compensated while the atoms are decelerated from a maximal velocity $v_{th} = 910\text{m/s}$ to nearly standstill. The Doppler frequency shift linearly depends on the velocity as $\Delta\omega_D = \frac{2\pi}{\lambda_L}v(x)$, where λ_L is the resonance laser wavelength (671nm). The frequency shift $\Delta\omega_Z$ caused by the Zeeman effect is linear with respect to the magnetic field amplitude: $\Delta\omega_Z = \frac{\Delta m\mu_B B(x)}{\hbar}$, where Δm is the difference in magnetic quantum number between ground and excited state [101], and μ_B is the Bohr magneton. For a certain final velocity v_{end} , one obtains the condition for the cancelation of the two frequency shifts:

$$\frac{\Delta m\mu_B B(x)}{\hbar} = \frac{2\pi}{\lambda_L}v(x) - \frac{2\pi}{\lambda_L}v_{end}. \quad (3.1)$$

There are two possibilities to control the velocity of the atoms. One is to choose the final velocity v_{end} reached when the magnetic field $B(x)$ drops to zero. The final velocity can be tuned by setting the corresponding frequency difference ω_{end} with respect to resonance frequency of an atom at rest to $\omega_{end} = \frac{2\pi}{\lambda_L}v_{end}$. In our case, the frequency of the counter-propagating laser is detuned to $\nu_{end} = \frac{\omega_{end}}{2\pi} = -86\text{MHz}$, which results in a final velocity of approximately 60m/s at zero magnetic field.

The other way to control the velocity is through the spatial magnetic profile $B(x)$, which in effect controls the velocity profile $v(x)$. There are obviously physical limits to the maximum deceleration: as long as the laser frequency is in resonance with the atoms in the moving frame, the scattering force F_{sc} can be assumed to be constant. The scattering force only depends on the resonant photon scattering rate Γ and the average photon recoil momentum p_{ph} . If the transition is driven with only half of the saturation intensity, the corresponding maximal deceleration is $a = \frac{F_{sc}}{m} = \frac{\Gamma}{4} \frac{-|p_{ph}|}{m}$. The velocity profile can be expressed by

$$v(x) = \sqrt{2 \left(\frac{\Gamma p_{ph}}{4 m} \right) x + v_{th}^2}, \quad (3.2)$$

where m is the lithium mass. By combining equations 3.1 and 3.2, the shape of the magnetic field $B(x)$ can be determined.

3.3.1 Dimensions and construction of the Zeeman slower coil

All important coil parameters can be calculated with only two assumptions: The maximal initial velocity, v_{th} , above which atoms cannot be decelerated and the maximal scattering rate, which must of course be smaller than Γ . The former sets the maximally needed magnetic field amplitude (equation 3.1), which is $B_{max} = 929\text{G}$ in our case. The latter determines the minimally needed laser light intensity and the minimal length of the Zeeman slower (equation 3.2), which is $I = 1.28\text{W/cm}^2$ and $L = 442\text{mm}$. The construction of a Zeeman slower coil is experimentally feasible only because the deceleration $\frac{F_{sc}}{m} = 5.9 \cdot 10^6\text{m/s}^2$.

The minimal inner radius of the coil is ultimately limited by the radius r_{zs} of the atomic beam. Because there is absorption and spontaneous emission in random direction, even a perfectly collimated atomic beam changes its radius along the beam axis as

$$r_{zs}(x) = \int v_{trans}(t) dt = \int v_{trans}(x)/v(x) dx, \quad (3.3)$$

where $v_{trans}(t) = \int_0^t \left(\frac{1}{3} \sqrt{\Gamma/4t'} p_{ph} \right) dt'$ is the transversal velocity. At the position, where the lithium beam leaves the Zeeman slower vacuum tube, the beam radius $r_{zs,max} = 9\text{mm}$.

With the set of parameters B_{max} , L and $r_{zs,max}$, one can roughly estimate at what current density the coil needs to be operated and if water cooling is required due to ohmic heating. The Zeeman slower coil cannot be wound directly onto the vacuum tube, since vibrations during coil turn off have to be avoided and any heat dissipation during operation would negatively affect the vacuum conditions in the main chamber. Nevertheless, the coil design should be as compact as possible to make operation at lower current densities possible. A small radius at the end of the slower is advantageous since it will enable a rapid magnetic field decay and less disturbance of the magnetic field for the magneto-optical trap.

In figure 3.4, a cut through the Zeeman slower is shown. The innermost tube is a custom made vacuum tube out of stainless steel. It consists of a micro conflate flange (CF10), which is attached to the gate valve, a differential pumping tube, a main Zeeman

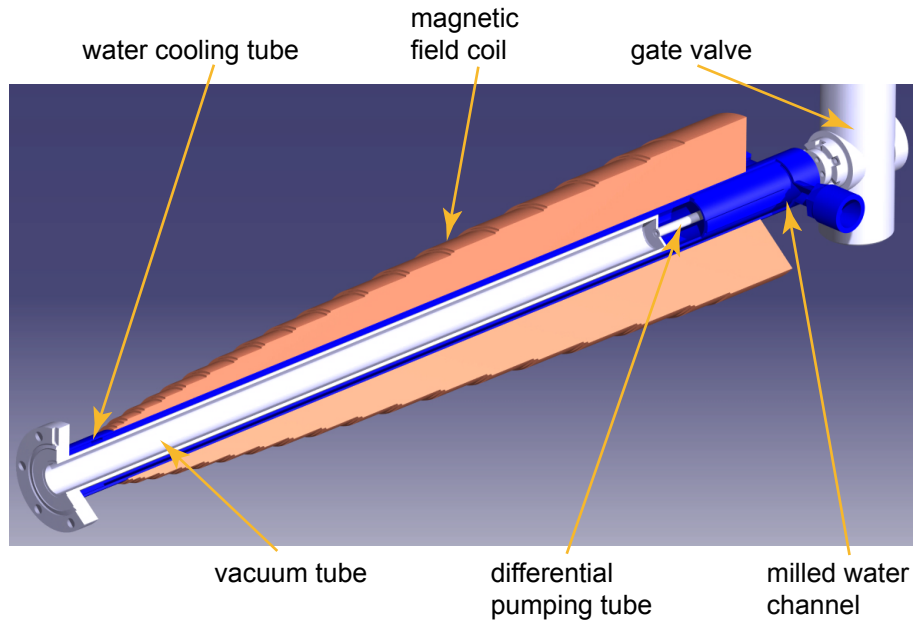


Figure 3.4: Zeeman slower, which is illustrated as a partially cut CAD drawing. Wires wound around the double-walled cooling tube, which is mounted separately from the vacuum tube, produce a square root shaped magnetic field with a total number of 4190 windings and a wire length of 520m.

slower vacuum tube, whose inner radius is 10.5mm (slightly larger than the maximal lithium beam radius $r_{zs,max} = 9mm$ in the tube) and a CF40 conflat flange. The coil is wound around a double-walled copper tube with integrated water channels milled along the inner tube, yielding a very compact coil mounting and cooling system with an outer radius of only 17.5mm. The two copper tubes are vacuum-welded with an electron beam to ensure that no cooling water leaks out.

The coil itself consists out of 17 double layers and a single layer of $1 \times 3 \text{ mm}^2$ high temperature doubly enamelled copper wire. The layers are grouped in pairs, with each double layer starting at a different position to realize the square root shaped magnetic field required by equation 3.2. The longest double layer has 185 windings and a length of 571mm. Instead of winding the entire coils with one continuous piece of wire, every pair is connected to a central board, where the various pairs are connected in series. This precaution was taken to be able to disconnect layers in which shortcuts could occur after coil bake out. The coil was wound by a professional coil manufacturer. No thermally conducting glue was used since none of the available glues had a thermal expansion coefficient similar to copper wire. Air confinements between coil layers and dried glue would be a perfect thermal insulation after coil bake out. Instead, air confinements were

reduced by winding the coil at a constant force of 50N and a wire positioning precision along the coil axis of about 1mm per meter. The coil was then sealed with aluminium tape and all wire endings were fixed with clamps. An additional water cooling tape made out of a stainless steel mesh with incorporated Teflon tubes was wound around the coil. Only one power supply with 8A and 50V is used to operate the Zeeman slower coil. Apart from the connection board, the whole installation can be baked at temperatures as high as 250°C.

The coil was tested regarding thermal characteristics and the magnetic field shape. The cooling system on the inside and the outside of the coil prevents overheating if it is run at a duty cycle of 30%. The measured magnetic field $B(x)$ was compared to the simulation including all aspects of the dimensioning of the coil as explained above. The simulated deceleration profile along the coil axis obtained with the actual magnetic field shows that deviations between simulated and measured magnetic field curves should not diminish performance (figure 3.5).

The mode of the laser beam that induces the decelerating atom-photon collisions is approximately matched to the atomic beam size. At the starting positions of the Zeeman slower, $x = 0$, the atomic beam diameter has about the size of the inner diameter of the differential pumping tube, i.e. 3mm. At the end of the Zeeman slower, where the acceleration drops to zero, the atomic beam radius $r_{zs,end} \simeq 14\text{mm}$ according to the simulation. Here, to obtain a good overlap with the atomic beam, we use a telescope with lenses of focal length $f = 25\text{mm}$ and $f = 200\text{mm}$ to enlarge the beam radius and to focus the laser beam from an initial radius at the lens position of approximately 10mm to a radius of about 3mm. A minimal laser power of 20mW is needed to drive the electronic transition at more than half of the saturation intensity at any position of the atomic beam.

The laser beam is transmitted through a Sapphire viewport that is directly bonded to a CF63 flange. Sapphire is optically birefringent, but has the advantage that it is not corroded by lithium. Around the viewport, a heating cuff with an extra insulation glass in front of the viewport was mounted to heat up and evaporate a potential lithium coating on the window. Moreover, the CF40 gate valve (figure 3.1) should allow one to replace the sapphire viewport without breaking the vacuum in the main chamber.

The transition $2^2S_{1/2}, m_J = 1/2 \rightarrow 2^2P_{3/2}, m_J = 3/2$ is driven by circularly polarized laser light, where m_J are the magnetic quantum number of the electron (for details see figure 3.22 on page 82). Seventeen per cent of the atoms in the beam have an initial velocity below 910m/s at an oven temperature of 380°C. With this oven and Zeeman slower configuration, we obtain a flux of slowed atoms of approximately 10^9 s^{-1} , enough for our experimental purposes.

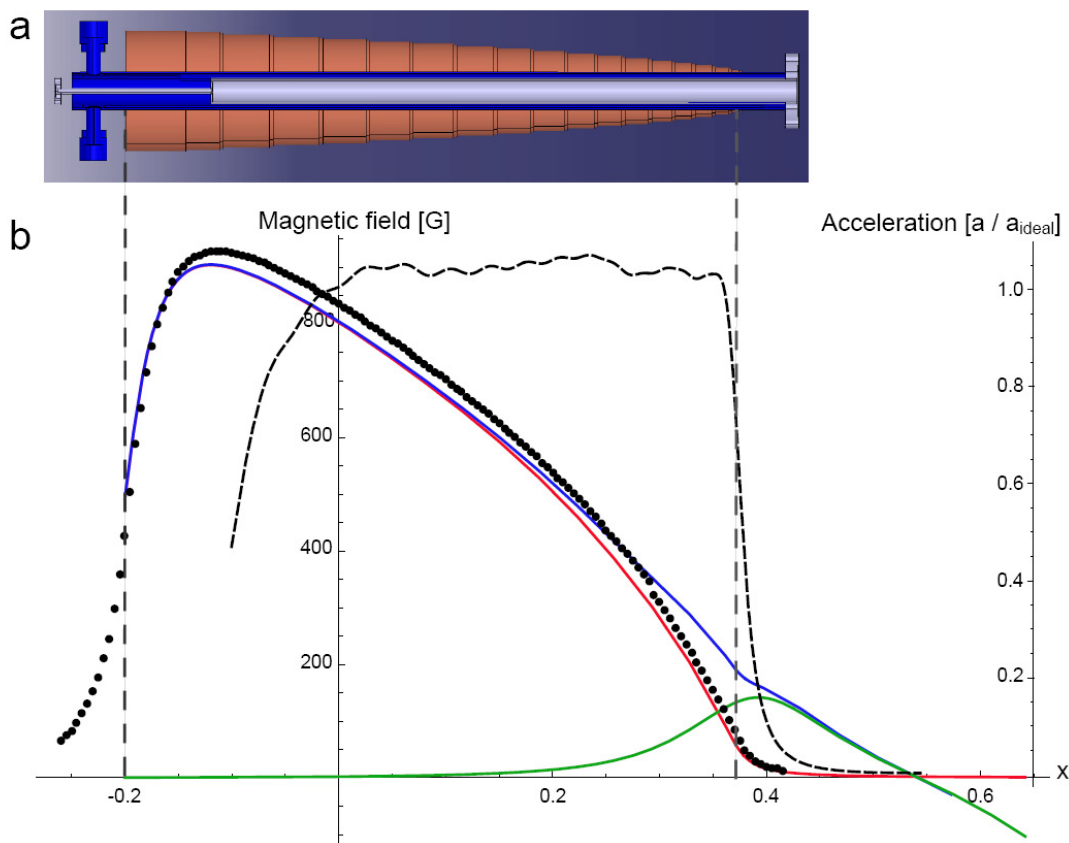


Figure 3.5: a. A cut through the Zeeman slower coil. b. Simulated curves are the magnetic field curve $B(x)$ of the Zeeman slower (red line), the gradient field of the magneto-optical trap (green line) and the combined magnetic field (blue line). Inserting the measured magnetic field values (black circles) into the simulation leads to a deceleration profile (dashed line), which is scaled with $a_{ideal} = \frac{\Gamma - |p_{ph}|}{4m}$.

3.4 Main chamber

The decelerated atoms enter the main chamber where they are trapped and cooled, first in a magneto-optical trap making use of spontaneous light forces, then in a standing wave dipole trap created by the optical resonator and finally in a running wave dipole trap, which is created by focused laser beam. The three traps are all located at the center of the main chamber to reduce the effects of eddy currents caused by fast switching of magnetic fields. The following is an overview of components in and around the main chamber (figure 3.6a) and the main chamber itself (figure 3.6b).

The most prominent and technically challenging component in the main chamber is the in-vacuo optical resonator, which basically sets the dimension of the main cham-

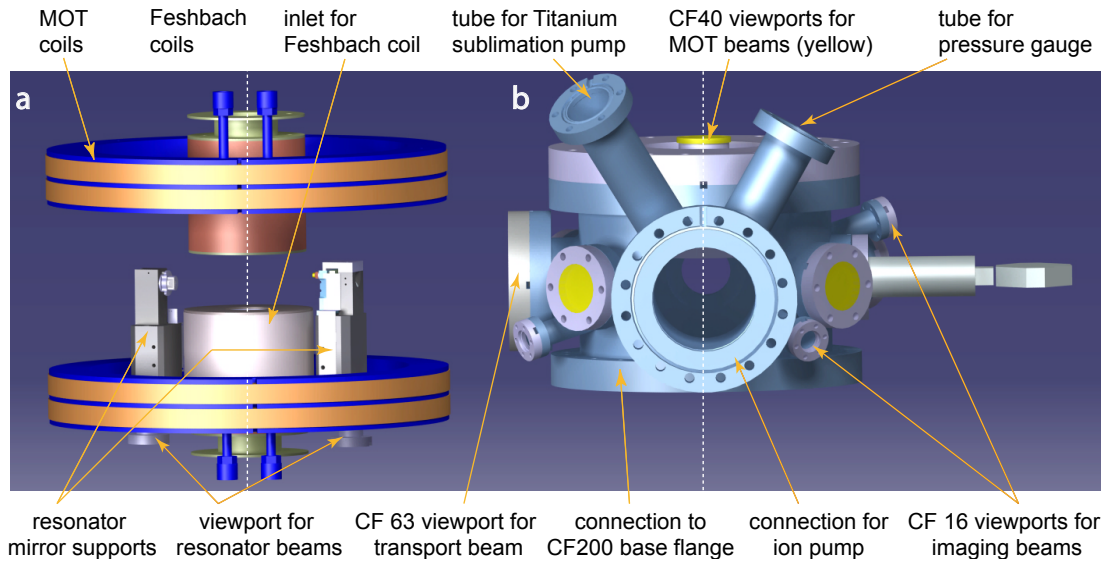


Figure 3.6: Overview of the main chamber. a. Components in and around the main chamber: optical resonator mirror supports with base flange setting the dimensions of the main chamber and magnetic field coils for magneto-optical trapping and evaporative cooling. b. Main chamber with connecting flanges for viewports, pumps and the resonator base flange.

ber. The two resonator mirror mounts are directly attached to a CF200 base flange. Light which is coupled into the resonator, passes through the CF16 viewport (15mm in diameter) vertically and is afterwards redirected to the horizontal resonator axis.

Onto the base flange is mounted a custom made, TIG-welded stainless chamber, which provides optical access for the magneto-optical trapping light and for the running wave dipole trap. There are four CF40 anti-reflection-coated glass viewports (38mm in diameter) horizontally and two housekeeper-sealed viewports vertically. Since housekeeper-sealed viewports could not be coated, an anti-reflection-coated substrate with an index matching oil was attached to the outside to the optical viewport to decrease reflections. A CF63 fused silica viewport (63mm in diameter) offers optical access for a tightly focussed laser beam that creates a running wave dipole trap in which atoms are transported to the glass cell and evaporated there. Two pairs of additional CF16 glass viewports, whose axes are orthogonal, allow one to image atoms located in the center of the main chamber.

All magnetic field coils are mounted around the chamber on mounts that are totally separated from the chamber and the optical elements to reduce vibrations during coil turn off. For the magneto-optical trap, there are two large coils in anti-Helmholtz configuration to create the needed quadrupole field. For evaporation in the standing

wave dipole trap, which is created by the optical resonator, as well as in the running wave dipole trap, there is one pair of Feshbach coils. One is centered around the main chamber, in inlets of the base and top flange to obtain large magnitude magnetic fields at moderate currents (a second pair of Feshbach coils is centered around the glass cell, where a final evaporation step and experiments are done). There are five smaller auxiliary coils around the main chamber which are not shown in figure 3.6a.

In the main chamber, ultra-high vacuum is achieved with a residual pressure below $1.8 \cdot 10^{-11}$ mbar [103]. Two pumps maintain the vacuum. One is a 80l/s ion-getter pump with differential pumping elements consisting of titanium and tantalum to improve pumping of argon and helium. The other is a mini ball-point titanium sublimation pump. The ion-getter pump is directly connected to the main chamber via a tube with 89mm diameter to obtain maximum pumping efficiency. Magnetic stray fields caused by the ion-getter pump at the position of the magneto-optical trap and in the glass cell on the order of mG/cm. The mini-ball titanium sublimation pump is mounted inside the connecting tube. Its titanium ball is pointed at the main chamber to efficiently coat the inside of the vacuum chamber. Some shields had to be placed to protect windows and resonator optics from being coated directly. During sublimation, the gate valve at the Zeeman slower is closed to protect the window. Pressure is measured by a hot cathode pressure gauge, which is located in the connection between the ion-getter pump and the main chamber. This gauge overestimates the actual pressures below $2 \cdot 10^{-11}$ mbar by approximately a factor of two.

3.4.1 Installation

The main chamber and all standard components are made out of stainless steel (type 1.4401). Most of the sealings employed are preheated OFHC conflate flange copper gaskets. If there was a risk of lithium contamination, nickel gaskets were used, since lithium corrodes copper. Before assembly, the main chamber was electro-polished. Apart from the viewports, all components were first put into an ultra-sonic bath, cleaned with acetone and then baked out in air at a temperature of 200°C. After assembly, the main chamber was again baked out on air at 200°C before finally being evacuated. The bake out in the evacuated state lasted 5 days. After sublimation of titanium, the final pressure fell below the measuring range of the UHV pressure gauge.

3.5 Glass cell

All our experiments exploiting high resolution imaging are done in a glass cell, below and above which two microscope objectives are installed. This octagonally shaped, UHV-compatible cell (figure 3.7) is made out of fused silica plates.

Since the high resolution imaging and manipulation uses the optical access through the upper and lower windows of the glass cell, it is imperative that the thickness of these fused silica windows be known precisely and that the microscope objectives be corrected for these windows. Thickness measurements of the glass provided by the manufacturer, are $4 \pm 0.005 \mu\text{m}$. The glass cell is anti-reflection coated for 532nm, 671nm and 761nm on the outside of the upper, the lower as well as on front surface .

Because reflections from the inner walls cannot be avoided the octagon is turned by 3° counter clockwise around the z-axis. This reduces the detrimental effect of back-reflections of the running wave dipole trap that is used for transport.

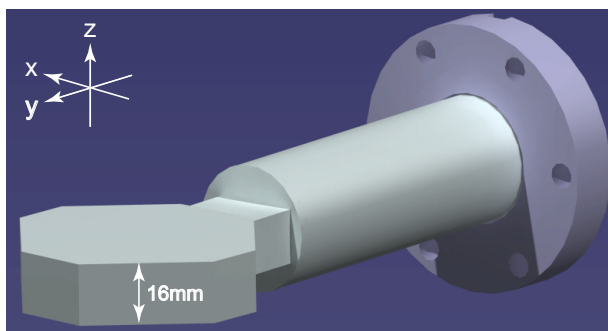


Figure 3.7: Illustration of the glass cell with glass-metal transition and CF40 flange. The octagon is made out of 4mm thick fused silica glass plates. Top and bottom glass plate are separated by 8mm.

The glass cell is attached to a non-magnetic glass-metal transition via a rectangular feed through. The final position of the glass cell could only be adjusted by asymmetrically tightening the screws of the rotatable con-flate flange. The whole glass cell is tilted by $\sim 1^\circ$ counter clockwise around the x-axis (figure 3.7). The distance between upper and lower surfaces was chosen to be as small as possible to attain a short working distance for the microscope objective and hence a high numerical aperture for the optical system. The minimum size of the rectangular feed through is limited by the minimum pumping

speed needed, which is approximately 7 l/s in our case.

Before installing the glass, it was cleaned on the inside and the outside. Evacuating the vacuum chamber did not stress the surface or bend the glass plates, according to measurements with a Hartmann-Shack sensor. The glass cell was encased within a special metal housing serving as an oven for the bake-out, which was carried out at 175°C . The birefringence of the glass plate after pump-down and bake-out is not known. Precautions have to be taken if the main chamber is floated, since the glass cell cannot withstand any excess pressure.

3.6 Optical traps

During the cooling procedure, atoms are trapped with two different techniques, which are explained in more detail in the following section. Each trapping technique only works for a limited temperature range. In our case, atoms that are magneto-optically trapped with dissipative light forces, have a maximal temperature of 0.93K and can be cooled down to a minimal temperature of $140\mu\text{K}$ [14, 60]. At the lower temperature limit, heating and cooling caused by resonant scattering achieves a balance. For a further reduction of temperature, the atomic ensemble needs to be transferred to a different type of trap. This is a conservative potential which can be generated by either magnetic [104] or optical dipole forces [63]. There, heating of atoms caused by resonant photon scattering is largely reduced within the relevant time scale of one experiment sequence, which lasts about 15s. Optical dipole traps have the two advantages that all spin states can be trapped and that the magnetic field still remains as a free parameter. The latter is important for evaporative cooling [14, 50, 58, 61]: because the scattering cross section can be tuned to large values by the magnetic field by accessing a Feshbach resonance, thermalization times can be shortened.

Compared to resonant light forces, the optical dipole force, and therefore its potential, is weak. The mean temperature of an atomic ensemble inside an optical dipole trap is mainly determined by its potential depth. An atomic ensemble at a mean temperature of $140\mu\text{K}$ is only efficiently transferred into a dipole trap generated by sufficiently large laser intensities. By lowering the depth of the potential, the hottest atoms are evaporated and the temperature can finally be reduced, in our case down to 200nK.

3.6.1 Magneto-optical trap

The magneto-optical trap [14, 60] serves as the final slowing stage of the atomic beam and as an atom trap. By making use of resonant light forces, which correspond to decelerations on the order of 10^6m/s^2 , the kinetic energy, and hence the temperature, can be reduced by a factor of 10^4 . The atomic beam enters the cooling and trapping region of the magneto-optical trap at a velocity of 60m/s (0.93K) and is then decelerated further, before atoms are trapped. In the magneto-optical trap, lithium atoms can be cooled down to $140\mu\text{K}$, which is the so-called Doppler temperature T_D . Due to frequent resonant light scattering, the minimal kinetic energy $k_B T_D$ of the atoms is given by a random photon recoil movement, which corresponds to a mean velocity of approximately 70cm/s. Because of the characteristics of the hyperfine splitting of the excited states of lithium, the temperature can not be decreased below Doppler temperature with resonant light [105].

The final slow-down of the atoms works as in the case of the Zeeman slower: atoms

decelerate through the magneto-optical trap's decreasing quadrupole magnetic field to compensate for the Doppler shift. With equations 3.1 and 3.2, and a mean photon scattering rate $\frac{\Gamma}{2}$, a minimum deceleration distance of 0.15mm can be estimated, over which the atoms are brought to standstill. At the turning point, the atoms are then forced to reverse into the trap center. Because of the magnetic field gradient in the 3D case, transitions between two Zeeman substates are only resonant at that position in space given by an ellipsoidal shell with a thickness of more than 0.15mm.

The polarizations of the laser light are chosen such that only the laser beams, which are counter-propagating to the motion of the atom are resonant. As soon as atoms approach the ellipsoidal shell, one of the three pairs of counter-propagating laser beams exerts dissipative light forces to slow the atom down and again to force them to reverse direction.

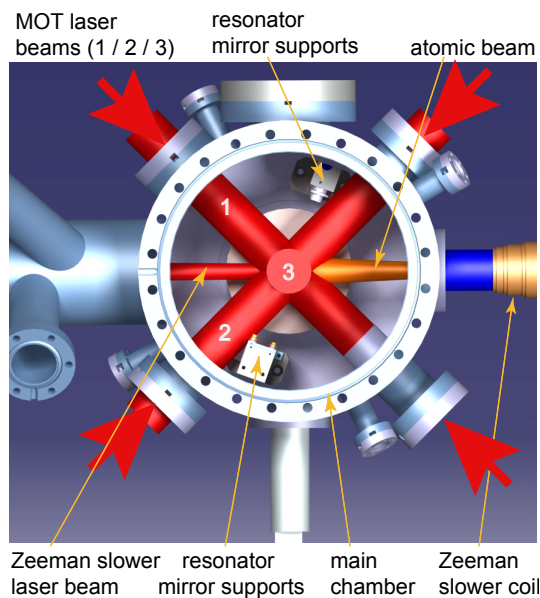


Figure 3.8: Top view of the main chamber. Three orthogonal pairs of retro-reflected MOT laser beams pass through viewports of 38mm in diameter and trap atoms of the decelerated atomic beam. Resonator mirror supports are placed such that resonant light is not reflected.

The shell is centered at the location of the zero point of the magnetic field. In order to trap a high number of atoms, this ellipsoidal shell, at which atoms are repelled into the trap center, should be large. This, in turn, asks for large laser beam diameters and laser power.

Experimentally, the size of the trapping region is limited by the diameter of the three counter-propagating laser beams and the available laser power. Here, the laser power is equally split into four beams, of which three are used. After passing through the main chamber, the three MOT-beams are retro-reflected (figure 3.8). Because the level structure of lithium at low magnetic fields can be treated as an actual three level system, with two ground and one excited state, two laser frequencies with equal power are needed to drive the transitions $2^2S_{1/2}, F = 3/2 \rightarrow 2^2P_{3/2}, F = 5/2$ and $2^2S_{1/2}, F = 1/2 \rightarrow 2^2P_{3/2}, F =$

$3/2$, where F is the hyper-fine spin (for details see figure 3.20 on page 77). The average intensity of each laser beam and each frequency, being transmitted through the CF40

(38mm in diameter) is about saturation intensity. The laser frequency is de-tuned below resonance between 3MHz (-0.5Γ) and 39MHz (-6.5Γ).

3.6.2 Optical dipole trap

Attractive potentials can be created by light fields that are far red de-tuned from the resonance frequency. There, resonant photon scattering is largely suppressed and the electrical fields of the laser light only induce electrical dipole moments in the atoms, causing them to be attracted by regions of high intensity. This creates a conservative potential, which is called optical dipole potential [63].

The optical dipole trap with a potential $U_{dip}(x, y, z)$ is given by the intensity distribution $I(x, y, z)$ of the light mode:

$$U_{dip}(x, y, z) = -\frac{3\pi c^2}{2\omega^3} \left(\frac{\Gamma}{\omega - \omega_L} + \frac{\Gamma}{\omega + \omega_L} \right) I(x, y, z) = -C(\omega_L)I(x, y, z), \quad (3.4)$$

where c is the speed of light, ω is the resonance frequency and ω_L is the laser frequency. Because resonant light scattering would significantly heat up the atomic ensemble, parameters should be chosen such that the photon scattering rate Γ_{dip} , which is given by

$$\Gamma_{dip}(x, y, z) = -\frac{3\pi c^3}{2\hbar\omega_L^3} \left(\frac{\omega_L}{\omega} \right) \left(\frac{\Gamma}{\omega - \omega_L} + \frac{\Gamma}{\omega + \omega_L} \right)^2 I(x, y, z) \quad (3.5)$$

is sufficiently low. Because the factor depending on the frequency difference $\omega - \omega_L$ is linear and quadratic for the dipole trap depth and the photon scattering rate, far de-tuned laser light at large intensities is chosen to achieve deep trapping potentials and a low scattering rates. The following is a discussion about the creation of two different dipole potentials employed in the experimental apparatus. Their intensity distribution $I(x, y, z)$ is given by a standing and a running wave.

3.7 Standing wave dipole trap

Atoms in the magneto-optical trap have a temperature $T_D = 140\mu\text{K}$. To reduce the temperature further, they are transferred into an optical dipole potential, where they are evaporatively cooled. In order to efficiently transfer atoms, the depth of the optical dipole trap should be on the order of the thermal energy of the atomic ensemble, about $k_B T_D$, and the size of the potential should approximately match the atomic cloud size, which is on the order of 1mm. At a wavelength of 1064nm, about 2100W of laser power

would be needed to obtain an optical dipole potential comparable to the thermal energy and size of a magneto-optically trapped atomic ensemble.

We transfer atoms into an optical dipole potential, which is created by intensity enhanced standing wave inside an optical resonator [62]. In order to obtain a large intensity enhancement, it is crucial that the mirrors be of high reflectivity as well as losses be low inside the optical resonator. In this experimental setup, the two resonator mirrors are placed inside the vacuum chamber to avoid losses otherwise caused by the residual reflectance of viewports. Since readjustment of the resonator mirrors in vacuum is impossible, a setup with long term stability had to be designed. With two resonator mirrors, mainly one selected laser mode in longitudinal and transverse direction is enhanced, forming a standing wave dipole potential with an adjustable size in transverse direction.

The following is a detailed discussion about the design of the optical resonator [106]. Important resonator parameters are introduced to explain how a large intensity enhancement and a large resonator mode size is obtained. Because the laser intensity inside the optical resonator is only enhanced if the resonance condition is fulfilled, i.e. the resonator length is a multiple of a wave length, active control of the laser frequency and passive stability of the resonator setup are described. To conclude this section, parameters of the created dipole potential are presented.

3.7.1 Intensity enhancement inside the resonator

Light travelling between two highly reflective mirrors builds up a standing wave whose intensity, and hence the potential depth in the anti-nodes, grows with the number of round trips. Naturally, the number of round trips as well as the intensity I_{circ} in the resonator are maximized if light is perfectly reflected many times before it is finally absorbed by or transmitted through one of the mirrors. Two mirrors of the highest commercially available amplitude reflectivity r_1 and r_2 able to be accurately specified, are used for the optical resonator. In order to obtain deep optical potentials with the available laser power, the intensity enhancement S , which is the ratio between the intensity I_{circ} in the resonator and the intensity I_{inc} that is coupled into the resonator, must be as large as possible. S can be expressed in terms of the reflectivities r_1 and r_2 as

$$S = \frac{I_{circ}}{I_{inc}} = \frac{t_1 t_2}{(1 - r_1 r_2 l)^2}, \quad (3.6)$$

with amplitude transmissions t_1 and t_2 and resonator amplitude losses l .

At the same time, amplitude reflectivities are chosen such that ideally all of the available incident laser light is coupled into the optical resonator. The highest efficiency

of coupling is achieved if the light intensity reflected from the input port vanishes. This can be expressed with the ratio

$$\frac{I_{refl}}{I_{inc}} \sim r_1^2(r_1 - r_2l)^2 \equiv 0. \quad (3.7)$$

Coupling efficiency is highest, if the second mirror compensates for resonator losses with a reduced amplitude reflectivity $r_2 = r_1l < r_1$. In this situation, the two mirrors are so-called impedance-matched.

3.7.2 Transversal mode size

Atoms that are trapped in the potential wells of the standing wave cannot move along the resonator axis. This allows one to adjust the potential depth and size separately. The potential depth depends only on the choice of the right amplitude reflectivities. The transversal mode size of the optical resonator is matched to the size of the atomic ensemble by setting the resonator geometry. Large transversal mode sizes, which are required in our case, are obtained with an optical resonator operating close to the given stability limit.

Here, we chose a two mirror configuration of a half near-concentric, or hemispherical resonator, which we are able to operate very close to the stability limit. It consists of a planar and a curved mirror M_1 and M_2 with a radius of curvature $R_1 = \infty$ and $R_2 = 150\text{mm}$, respectively.

This configuration is stable as long as the resonator length, given by the distance L between the two mirrors, is smaller than the radius of curvature R_2 . Here, we assume that only modes with a gaussian beam profile, i.e. the transversal mode profile of lowest order, are enhanced. By placing the two resonator mirrors close to the stability limit $\Delta L = R_2 - L$, the transversal mode size along the resonator axis can be expressed by

$$\omega_{\Delta L}(z) = \omega_0 \sqrt{1 + \frac{z^2}{L\Delta L}}, \quad (3.8)$$

with laser beam waist $\omega_0 = 42\mu\text{m}$. For small distances ΔL , the beam radius $\omega_{\Delta L}(R_2)$ at the location of the two mirrors M_2 diverges. The resonator is placed such that the magneto-optical trap is located in the center between the two mirrors at $\Delta L + L/2 \simeq L/2$, where the transversal mode size scales with $\sqrt{\frac{L}{\Delta L}}$. In our case, the hemispherical resonator is only $115\mu\text{m}$ from the stability limit. This results in a transversal mode size of $\omega_0 \approx \omega_{\Delta L}(\Delta L) = 42\mu\text{m}$ and $\omega_{\Delta L}(R_2) = 1.52\text{mm}$ at mirror M_1 and M_2 . The beam radius at the place of the atoms $\omega_{\Delta L}(L/2) \simeq 760\mu\text{m}$.

With increasing resonator length, the transversal mode size $\omega_{\Delta L}(R2)$ at the mirror M_2 would become comparable to the diameter D of the mirror, $D/\omega_{\Delta L}(R2) \approx 1$, which reduces the angular tolerance between the perpendicular of mirror M_1 and the resonator axis. With any misalignment, a larger percentage of the mode would no longer be incident on the mirror and losses would increase. However, in our case, the size D of the mirror is much larger the transversal mode $\omega_{\Delta L}(R2)$ and the only critical parameter remaining is the resonator length L .

3.7.3 Measuring the standing wave dipole potential

In order to determine the actual dipole potential in the resonator, the intensity distribution $I(r, z)$, given by the power P_{circ} in the standing wave and the gaussian beam profile $\omega_{\Delta L}(z)$, is measured.

For the transversal mode size $\omega_{\Delta L}(z)$, the exact distance to the stability limit, and hence the resonator length L , needs to be determined. This is done here by measuring the frequency difference $\Delta\nu_L(\Delta q, \Delta m, L)$ between the Gaussian ($m = 0$) and higher order transversal modes ($m > 0$), as well as between different axial modes q , which are functions of the resonator length L . These frequency differences can be obtained by measuring the drop in reflection (equation 3.7) at the input port of the resonator, which occurs if the laser frequency of the transversal modes are in resonance with the optical resonator and light is actually coupled into the resonator.

The power P_{circ} inside the resonator is obtained by measuring the power P_{inc} , which is coupled into the resonator, and multiplying it with the power enhancement S . Since the power enhancement S depends on the resonator losses (equation 3.6), an actual resonator loss measurement has to be performed to finally obtain P_{circ} . As in the case of a damped oscillator, the energy dissipation, and hence loss, is characterized by the quality factor Q . Its optical counter-part is the finesse F . It is used to characterize the decrease of power inside the resonator optical. The finesse is obtained by first turning off the laser at the input port and then measuring the exponential decay in power P_{trans} . From the decay time, the finesse $F(l)$ can be fitted to determine finally the resonator loss coefficient l .

Due to imperfect mode matching, the power P_{actual} measured at the incoupling mirror and relevant power P_{inc} matching the resonator mode can differ significantly. For comparison, we can find the power inside the resonator, $P_{circ} = P_{trans}/|t_2|^2$, also by independently calibrating the amplitude transmission t_2 of the second mirror and by measuring the transmitted power P_{trans} . The ratio between power inside the resonator P_{circ} obtained from the two methods is a measure for the mode matching quality.

The following is a more detailed explanation of how $\omega_{\Delta L}(z)$ and P_{circ} are measured,

before the estimated standing wave dipole potential as well as the resonator parameters are listed at the end of this section.

Determination of the transversal mode size

The transversal modes are only enhanced inside the optical resonator, if their frequencies fulfil the resonance conditions of the optical resonator: After one round trip inside the resonator, the light must be phase shifted by a multiple of 2π to constructively interfere. In that case, light is coupled into the resonator and a drop in reflection can be observed. For a hemispherical resonator, transversal mode frequencies

$$\nu_L(q, m, L) = \frac{c}{2L} \left(q + \frac{m+1}{\pi} \arccos \left(\sqrt{\frac{R_2 - L}{R_2}} \right) \right), \quad (3.9)$$

depend on the axial as well as on transversal mode numbers q and m . The speed of light is given by c . One can then measure the frequency difference between two transversal modes, $\Delta\nu_L(\Delta q = -1, \Delta m = 2, L) = \nu_L(q, m, L) - \nu_L(q-1, m+2, L) = 18\text{MHz}$, and calculate $L = 14.875\text{mm}$ with equation 3.9. Once the length is known, the waist at the location of the magneto-optically trapped atoms, $\omega_{\Delta L}(L/2) = 760\mu\text{m}$ can also be calculated with equation 3.8 and $\Delta L = R_2 - L$.

Estimation of the power inside the resonator

The simplest way to estimate the power inside the resonator is to measure the transmitted power $P_{trans} \simeq 100\text{mW}$ and the transmission coefficient $|t_2|^2 \simeq 0.015\%$ of the second mirror. Then the power inside the resonator is $P_{circ} = P_{trans}/|t_2|^2 \simeq 670\text{W}$. While we now know how much power is in the resonator, it is instructive to understand what limits this power. The three limiting factors are the mode matching, the absolute input power P_{inc} and the impedance matching and power enhancement, both contained in S .

Power enhancement occurs because light travels a certain number of round trips inside the resonator before it is either transmitted through one of the mirrors or lost. Naturally, the power enhancement S depends on the characteristics of the mirrors, i.e. amplitude reflectivity r , transmission t and losses l . While reflectivities r and transmission t of the two mirrors are precisely specified by the manufacturer, resonator losses l have to be measured. Losses are obtained by measuring the finesse $F(l)$. As in the case of the quality factor Q of weakly damped oscillators, which stands for the number of oscillation before the energy of the oscillator has dropped by a factor e , the Finesse F is the quality factor for optical resonators. The finesse is proportional to the number of round trips n_{rt} , before the energy inside the resonator drops by a factor e and is often expressed by

$$F = \frac{Q}{q_{rt}} = 2\pi n_{rt}, \quad (3.10)$$

where q_{rt} is the number of oscillations per round trip. Here, not the energy inside the resonator, but the power P_{trans} , is measured. After the incoupling laser light is turned off, the light inside the resonator behaves like a weakly damped optical oscillator, whose finesse can be extracted by measuring the exponentially decaying transmitted power

$$P_{trans}(t) \sim P_{circ}(t) \sim e^{-\frac{t-t_0}{\tau}} \sim e^{-\frac{2\pi}{F} \frac{c}{2L}(t-t_0)}. \quad (3.11)$$

The resonator loss l can now be estimated with the expression

$$F(l) = \frac{\pi\sqrt{(r^2l)}}{(1-r^2l)}. \quad (3.12)$$

With a finesse $F = 10200$, the given transmission coefficients t_1 and t_2 , and equation 3.6, we obtain a power enhancement of $S = 1580$ and a power $P_{circ} = P_{actual}S = 1030\text{W}$. The coefficient to characterize the mode matching is given by $(P_{trans}/|t_2|^2)/(P_{actual}S) = 670\text{W}/1030\text{W} = 0.65$.

Standing wave dipole potential and resonator parameters

With all optical resonator parameters either measured or deduced (table 3.1), this subsection can be concluded with an expression for the dipole potential, which is created by a gaussian mode ($m=0$) inside a hemispherical resonator. By combining equations 3.4, 3.8 and the fact, that inside the resonator the intensity distribution is modulated with a sinusoidal function, we obtain an approximated expression for the resonator dipole potential:

$$U_{dip,res}(r, z, \omega_L) \simeq -2C(\omega_L) \frac{2P_{trans}/|t_2|^2}{\pi\omega_{\Delta L}^2(z)} \exp\left(\frac{-2r^2}{\omega_{\Delta L}^2(z)}\right) \sin^2\left(\frac{2\omega_L}{c}z\right). \quad (3.13)$$

With a maximal trap depth of $U_{dip,res,max}(0, L/2, \lambda_L = 1064) = k_B 46\mu\text{K}$ and an assumed temperature of the magneto-optically trapped atomic ensemble of $140\mu\text{K}$, we expect a transfer efficiency of 12%. The measured transfer efficiency is 0.46% (the atom number in the magneto-optical trap was determined by measuring the fluorescence signal giving only an order of magnitude). Here, the potential depth is mainly limited by the available laser power and the coupling efficiency due to limited impedance-matching.

Resonator parameters	
radius of curvature R_1 / R_2	150mm / ∞
resonator length L	1.485mm
distance to stability limit ΔL	115 μ m
beam waist ω_0	42 μ m
beam radii $\omega_{\Delta L}(\frac{L}{2})$ and $\omega_{\Delta L}(L)$	760 μ m / 1.52mm
reflectivities $ r_1 ^2$ and $ r_2 ^2$	99.98 \pm 0.005 %
transmission $ t_1 ^2$ and $ t_2 ^2$ at 0°	0.015%
antireflection coating at 1064nm, reflection	0.0228%
resonator loss factor $ l ^2$	0.999784
finesse F	10200
resonator linewidth $\Delta\nu_{res}$	98kHz
intensity enhancement S	1580
measured / theoretical coupling efficiency	32.5% / 50%
transmitted power P_{trans}	100mW
maximum power $P_{circ,max}$	670W
maximum intensity at $L/2$	1.5 \cdot 10 ⁹ W/m ²
maximum potential depth $U_{dip,res,max}(0, L/2, \lambda_L = 1064)$	k _B 46 μ K
maximum trap frequencies for ⁶ Li: w_r, w_z	100Hz / 4.1MHz
expected / measured atomic transfer efficiency	12% / 0.46%

Table 3.1: Properties of the optical resonator

3.7.4 Stabilizing the laser frequency

The power P_{circ} of the light that has been coupled into an optical resonator is only enhanced if its frequency fulfils the resonance condition given in equation 3.9, in our case with a gaussian mode $m = 0$. But since vibrations and thermal drifts change the resonator length L as well as the laser frequency ω_L , it would not only be hard to keep the power inside the optical resonator constant, it would also not be possible to reliably couple light into the resonator without active stabilization of either the length or the frequency. Especially in our setup, where the resonance width $\Delta\omega_{res}$ is reduced due to the large power enhancement S ,

$$\Delta\nu_{res} = \frac{c}{2L} \frac{1}{F} \sim \frac{1}{S}, \quad (3.14)$$

the maximal relative length changes are extremely small and hence make the stabilization challenging. In our case, the resonance width is only about $\Delta\nu_{res} = 98$ kHz.

This width in frequency corresponds to a change in resonator length of only $\Delta L_{res} = 5.3 \cdot 10^{-11} \text{m}$.

Here, we implemented two control loops to keep the resonance condition: one is the electronic control of the resonator length via the electro-striction of a piezo crystal, the other the laser frequency locked onto the resonator. The electronic control of the resonator length via a piezo tube is limited to a stroke of only about a tenth of the free spectral range and a bandwidth of only 200Hz. This limitation is most probably caused by friction between the piezo tube and its housing. So, we decided to control only the laser frequency. With a frequency modulation bandwidth up to 200kHz and a maximum frequency deviation of about a quarter of the free spectral range, we achieved a frequency stabilization with intensity fluctuations of approximately 1% rms.

The error signal for the laser frequency control is obtained with the Pound-Drever-Hall technique [107]: The laser light for the resonator dipole trap has a carrier frequency $\nu = \nu_L + \nu_{aom}$, which is the frequency of the laser source ν_L shifted with an accusto-optical modulator [AOM] by a frequency ν_{aom} . The carrier frequency ν is phase modulated with an electro-optical modulator [EOM], generating sidebands at $\nu \pm \nu_{eom}$. These are used to detect the phase shift of the laser light reflected at the mirror M_1 with respect to the light entering the resonator and leaving it via M_1 (figure 3.9, gray box): The beat signal at frequency ν_{eom} occurring between the carrier and the two sidebands is detected with a photodiode and demodulated by frequency-mixing it with a local oscillator of frequency ν_{eom} . The resulting DC-signal is proportional to the phase shift close to resonance. A deviation of the carrier frequency from resonance frequency is therefore converted into an unambiguous error signal $\delta\nu_{error}$. This error signal is fed back to a (frequency) PID control. Its control signal $\nu_{control}$ locks the carrier frequency onto the resonator length via three devices (figure 3.9).

The first device is the accusto-optical modulator, which controls ν_{aom} with a high regulation bandwidth on the order of 200kHz. The second is a piezo-electric element that changes the laser cavity length and hence the laser frequency ν_L . The regulation bandwidth of the laser cavity length is approximately 300Hz. The third is a temperature control of laser crystal and is implemented to correct for slow ($< 1\text{Hz}$), but large deviations of the resonator length or laser frequency ν_L .

The frequency stabilization explained above can only suppress frequency dependent power fluctuations, but not those caused by misalignment of optics and power drifts of the laser source. Hence, the power inside the resonator P_{circ} needs to be controlled separately. The power P_{circ} is proportional to the power P_{trans} , which is transmitted through the resonator. The latter can be measured and stabilized. As power control element we use the deflection efficiency of the same accusto-optical modulator used for the Pound-Drever-Hall lock.

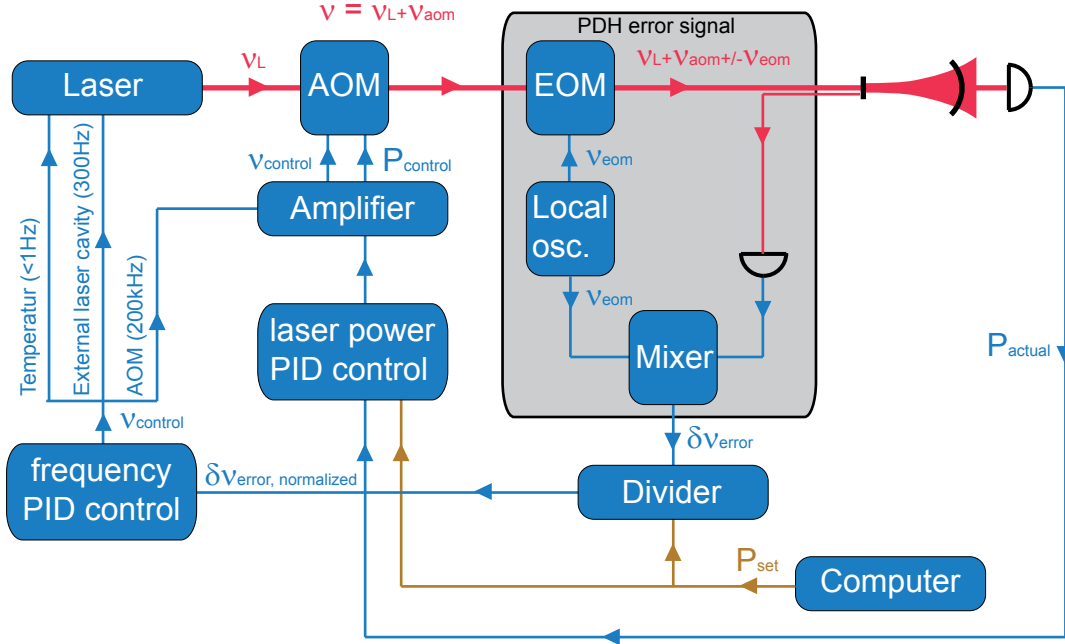


Figure 3.9: Schematic of the resonator frequency lock. The error signal $\delta\nu_{error}$ is obtained with the Pound Drever Hall (PDH) technique. Control elements of the frequency ν are the AOM (200kHz), external laser cavity (300Hz) and laser crystal temperature (<1 Hz). The resonator power is controlled with the same AOM.

Frequency and power control work independently as long as the stabilization level P_{trans} is constant. But during the preparation process, when atoms need to be evaporated, the dipole potential and therefore the level of P_{circ} is lowered to approximately 20% of the initial value. Because both the amplitude and the slope of the error signal $\delta\nu_{error}$ used for frequency control linearly depend on P_{trans} , the gain for the frequency lock changes and the control loop becomes unstable. We solved this problem by normalizing the error signal to obtain a constant gain: the error signal is divided by the signal P_{set} , which sets P_{trans} .

3.7.5 Mechanical setup

In our apparatus, the resonator dipole trap is the key element for a fast and efficient production of ultra-cold Fermi gases. Due to its large volume and its large enhancement, it enables the transfer of a large number of atoms from the magneto-optical trap into the resonator dipole trap with reasonable laser power. In order to obtain such a large enhancement, the resonator losses have to be minimized. This is done by placing the resonator mirrors into the vacuum chamber to avoid the most prominent loss source, the

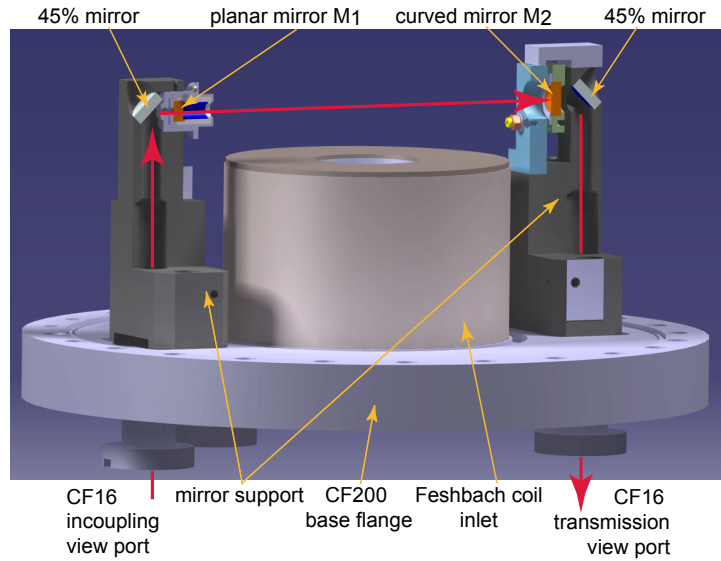


Figure 3.10: Optical resonator, which is illustrated as a partially cut CAD drawing. Two mirror mounts are precisely bolted onto a CF200 flange. Laser light, which is coupled in and out of the resonator, passes through these mount (red arrows).

transmission through vacuum windows (approximately 2% per round trip). Resonator losses are now dominated by the absorption and scattering losses of the mirrors, which are now 0.022%.

Placing a resonator inside the vacuum chamber and operating it so close to the stability limit is a high risk, because readjustment is impossible. Moreover, all materials used have to be UHV compatible and withstand temperatures of 250°C during the bake out of the vacuum chamber. In addition they need to be non-magnetic to assure high passive stability even during sudden magnetic field changes.

In figure 3.10 a partially cut through the resonator is depicted: Two large stainless steel supports (type 1.4436) are used to mount a resonator and a redirection mirror each. Both supports are rigidly bolted onto a CF200 blind flange. The maximal length deviation allowed before the resonator geometry is out of the stability region is $115\mu\text{m}$, which corresponds to a relative stability of $8 \cdot 10^{-4}$. The distance between the two supports is set by two parallel stop collars, that are machined into the CF200 flange with very high absolute precision. Despite the obvious advantage of vibration isolation we decided against it, since we feared that it might lead to drifts in the resonator length and position.

In the left support, the planar resonator mirror M_1 ($R_1 = \infty$) is mounted in such a way that there is only a translational degree of freedom along the resonator axis. A laser beam, which is approximately mode matched to the resonator mode, is transmitted

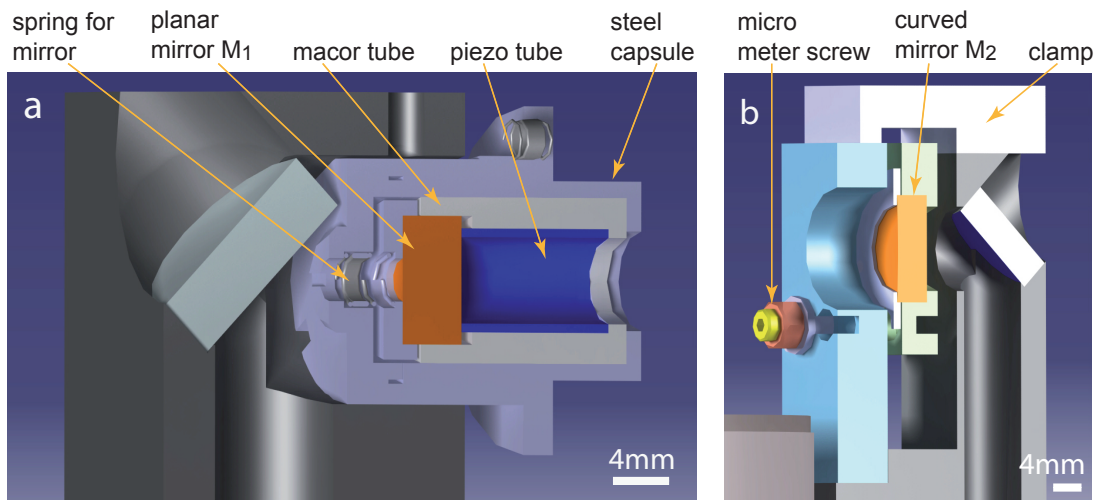


Figure 3.11: a. A cut through the planar mirror holder, which allows only a translational degree of freedom. b. A cut through the curved mirror holder, which allows only an angular degree of freedom.

through a CF16 viewport in upwards direction, reflected by a rigidly mounted 45° mirror and coupled into the resonator through mirror M_1 . On the right support, the second, curved mirror M_2 ($R_2 = 150\text{mm}$) is mounted. The transmitted light is coupled out through mirror M_2 and is redirected downwards, leaving the chamber through a CF16 viewport. The curved mirror is mounted in a mirror holder allowing angular adjustment only. Details of the two resonator mirror holders are shown in figure 3.11.

The planar mirror holder shown in figure 3.11a, contains mirror M_1 with a diameter of 7.75mm and a thickness of 4mm. The mirror is placed inside a macor tube. Macor is a ceramic whose surfaces can be precisely and smoothly machined. Inside that tube, the mirror can glide axially. A stainless steel spring, which is precisely pre-stressed with a custom machined adjustment screw, presses the mirror against a piezo-electric tube that can be electronically elongated for fine adjustment of the resonator length. The macor tube itself is put in a movable stainless steel capsule and the whole capsule is finally inserted into the precisely matching bore of the large mirror support. The position of the capsule can be coarsely adjusted axially by three set screws, with three springs acting as restoring forces. The capsule is partially slit to feed two Capton coated wires through for a high voltage connection of the piezo-electric tube. The wires were soldered directly to the piezo tube with Castolin 157 (an alloy made out of ^{50}Sn , ^{47}Ag and ^{82}Pb), which has a low melting point above 250°C and a sufficiently low vapor pressure to achieve ultra-high vacuum. Soldering flux Castolin 157 used for alloys evaporates during pump down.

The curved mirror holder shown in figure 3.11b contains the mirror M_2 with a diameter of 10mm and a thickness of 4mm. The mirror is mounted in a custom made kinetics mirror holder and fixed with a steel ring to distribute forces equally onto the mirror. The turning joint of the mirror mount is a non-magnetic sapphire ball. The angle of the mirror can be adjusted by three micrometer screws that push the holder against extremely stiff springs. The coarse outside thread of the micrometer screws fits into a counterpart, which is machined from OFHC copper. Locking screws allow to crush this relatively soft copper thread, which stops a creeping movement of the micrometer screws. After adjustment, each micrometer screw is fixed by a counter-nut. The whole mirror mount is clamped to reduce vibrations on the mirror.

3.8 Running wave dipole trap

In the standard preparation procedure of an ultra-cold Fermi gas, the atomic ensemble is transferred from the resonator dipole trap into a running dipole trap, the transport trap, which is created by a tightly focused laser beam. This transfer is essential for two reasons: the first is that the atomic ensemble cannot be cooled to Fermi temperature inside the resonator trap; the resonator power cannot be reduced to the required low values since the Pound-Drever-Hall error signal becomes too small for a reliable frequency control. Besides that, the evaporation process seems not to be very efficient in the standing wave trap. In the running wave dipole trap however, the trap depth can be precisely tuned over four orders of magnitude and hence the evaporation process is more easily controlled. The second reason is that atoms need to be transported into the glass cell to make use of the high resolution imaging. Here, atoms are transported from the center of the main chamber to the glass cell over distance of 268.8mm by mechanically moving a lens mounted on an air bearing translation stage [64].

Since atoms are also confined along the beam axis, they will follow the moving focus. The transport is done smoothly in order not to heat atoms and with a μm -precision in order to obtain comparable and reliable experimental data in every experimental cycle.

The following is an explanation of how atoms are transferred into the running wave dipole trap and how they are transported into the glass cell. Then, technical aspects, which focus on stability requirements and the control of the dipole trap depth, are discussed.

3.8.1 Transferring atoms into the transport trap

In order to efficiently transfer atoms into the running wave dipole trap, the trap depth should be on the order of the mean energy of the atoms trapped in the standing wave

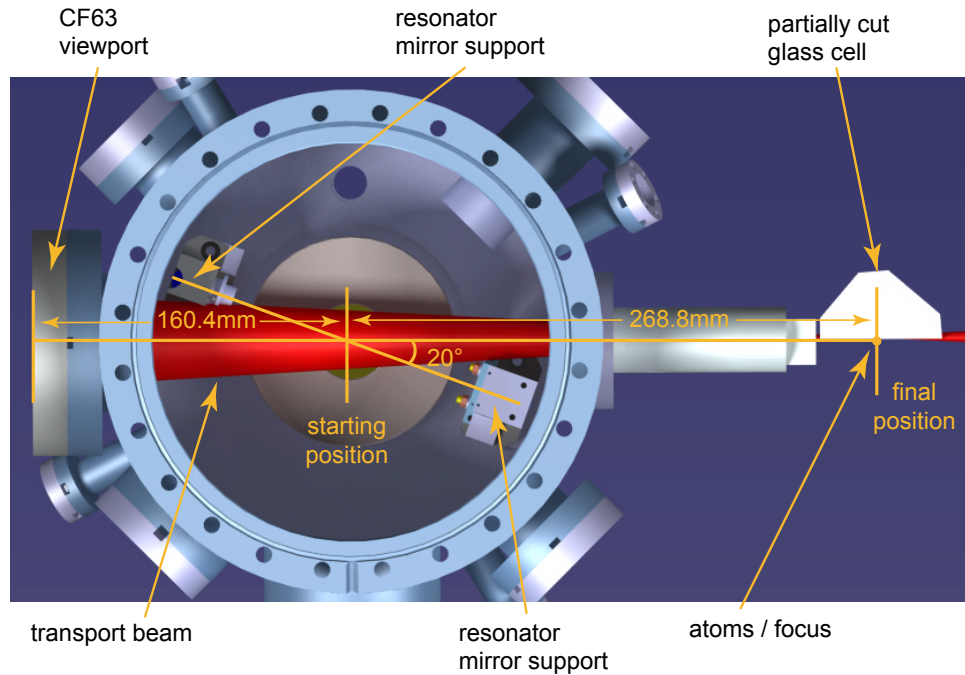


Figure 3.12: The top view of the main chamber and the partially cut glass cell illustrates the optical transport in the final position. The drawn beam radius of the transport laser beam, which is focussed by a lens with focal length $f = 1000\text{mm}$ and transmitted through the CF63 viewport, is approximately four times larger than the actual radius. Atoms which are initially trapped in the center of the main chamber (starting position) are transported over a distance of 268.8mm in less than 1s to the center of the glass cell (final position).

dipole trap, and the overlap region between the two traps should be as large as possible. So, first atoms are evaporated in the standing wave dipole trap to reduce their temperature. After some limited evaporative cooling, atoms are still trapped in the wells of the standing wave dipole potential at 20% of the initial potential depth, before the transfer into the running wave dipole trap begins. A tightly focused laser beam, which creates the running wave dipole trap, passes the standing wave dipole trap at an angle of 20° and overlaps approximately 1000 wells. In their overlap region, atoms are transferred from the wells of the standing wave potential into the running wave potential, before the former is switched off. Finally they are trapped only in the dipole potential of the tightly focused laser beam.

This dipole potential is created by a 10W fiber laser. After passing through an accusto-optical modulator and transversal mode cleaning with an optical single mode fibre, a maximum laser power $P = 3.5\text{W}$ is available, which forms a dipole potential that can be expressed with the intensity distribution of a gaussian beam [?, 63, 108]:

Transport trap parameters		
	P = 3.5W	P=10mW
beam waist ω_0	$22\pm 1\mu\text{m}$	
Rayleigh length z_R	1.3mm	
maximum potential depth $U_{dip,tt,max}$	$k_B 306\mu\text{K}$	$k_B 355\text{nK}$
trap frequencies w_r / w_z	9.9kHz / 112Hz	529Hz / 6Hz*
heating rate		2.93nK/s

Table 3.2: Properties of the transport trap. *At a low laser power, the axial confinement in the glass cell is determined by the magnetic field curvature of the Feshbach coil pair: $w_{magn.} = 2\pi\sqrt{\frac{\mu_B B''}{m}}$ with $B'' = (0.4145 \text{ T/m}^2\text{A}) \cdot I_{FB}$ and the current I_{FB} through the Feshbach coil.

$$U_{dip,tt}(r, z) = -C(\omega)I(r, z) = -C(\omega)\frac{2P}{\pi\omega^2(z)}e^{-2r^2/\omega^2(z)} \quad (3.15)$$

The maximal depth of the potential is given by $U_0 = 2P/\pi\omega_0^2$. The beam radius $\omega(z) = \omega_0\sqrt{1 + (\frac{z}{z_R})^2}$, with a measured beam waist $\omega_0 = 22\pm 1\mu\text{m}$, a Rayleigh range $z_R = 1.3\text{mm}$.

With the given values, estimates about the trapping potential can be made, which are listed in table 3.2.

3.8.2 A moveable dipole trap

Atoms which are trapped at the waist of the tightly focused laser beam can be transported by moving the focussing lens. For our experimental setup we chose a dipole trap, which is sufficiently deep to avoid spilling of atoms from the trap during the transport: while the radial confinement of atoms is only relevant in case of vibrations in transverse direction to the transport axis, the axial confinement along the transport axis is critical, because atoms should remain at the focus even at a higher acceleration of the trap.

First, we consider an accelerated gaussian trap in axial direction, whose effective potential can be regarded as a tilted gaussian trap. If the restoring force $F_{dip,tt}(z)$ of the transport trap in the axial direction is smaller than the inertial force $F = am$, where a is the acceleration and m is the mass, atoms will escape the trap. This relation can be expressed by

$$-\frac{\partial}{\partial z}U_{dip,tt}(0, z) = F_{dip,tt}(z) = C(\omega)\frac{2P}{\pi\omega_0^2}\frac{2}{(1 + (\frac{z}{z_R})^2)^2}\frac{z}{z_R^2} = am. \quad (3.16)$$

Atoms, which are located far away from the beam waist ($z > z_R$), will escape from the trap if

$$z \geq \sqrt[3]{C(\omega) \frac{2P}{\pi\omega_0^2} \frac{2z_R^2}{am}}. \quad (3.17)$$

With the beam configuration given in equation 3.15 and the low mass of ${}^6\text{Li}$, atoms can be transported over a distance of 268.8mm in only 1s. Shorter transport times did not cause a higher loss of atoms, but resulted in vibrations on the experiment table. We are not power-limited during transport.

In order to minimize atom loss and heating due to vibrations, we employ an air bearing translation stage and a tightly focussed the laser beam to achieve a strong axial and radial confinement. The translation stage onto which the lens is mounted has a maximum travel of 300mm. Brushless linear motors, driven by a linear power supply, move the stage. The position is measured by Hall sensors and is fed back to a controller, which can be actuated and triggered by the computer. The stage is accelerated and decelerated over a distance of 268.8mm in less than a second, according to a smooth velocity profile that can be programmed. Conventional oil free compressed air flows into the air bearings at a pressure of 5.8bar after being filtered through a series of fine filters. The performance of the experimental apparatus does not deteriorate by the air flow of about 0.14l/s.

Due to the divergence of the gaussian beam and the large transport distance (figure 3.12), the beam radius at the position of the resonator support for the planar mirror and the entrance port is $\omega(339.6mm) = 5.5mm$ and $\omega(429.2mm) = 6.9mm$, respectively. To limit reflections inside the vacuum chamber, the resonator mirror supports are designed and placed such that the laser beam is not cut off up to a radius of 4ω . The supports are positioned 15cm apart from each other and the resonator axis is tilted by 20° to still achieve a good spatial overlap between the two traps.

Two inch optics including the $f = 1000mm$ lens, mirrors for beam adjustment and a CF63 (63mm in diameter) fused silica viewport are used in order not to cut into the beam profile. The viewport is specially manufactured with surface flatness of $\lambda/8$ to minimize wave front distortions of the focused beam, which would limit the minimal achievable spot size. At the position of the lens, the beam radius $\omega(1000mm) = 16mm$ is 1.6 times smaller than lens radius.

3.8.3 Stability criteria

In every experimental sequence, atoms should be loaded at the same position and transported to the same final position in order to obtain comparable transfer efficiency and

hence reproducible experimental data. Especially in the final position, a positioning accuracy below $10\mu\text{m}$ is required in order to obtain high resolution images of the atomic ensemble at a depth of field on the same order. This requirement is challenging, since the beam path of the transport laser, which is mainly given by the focal length of the moving lens and the transport distance (adding up to a length of 1.3m) allows an angular deviation of only $4.4\cdot 10^{-4}$ °.

Using an air bearing translation stage, we achieve angular and position deviations such that initial and final position of the laser beam is reproducible to within $1\mu\text{m}$ in each direction. The position error in axial direction is given by the measurement error. Transverse to the transport direction, the position accuracy of the dipole trap focus is determined by the rigidity of the moving table, inhibiting roll, pitch and yaw, representing the maximum rotation angle around the transport axis, the horizontal and vertical transverse axis during motion, respectively. Position rigidity is given by flatness and straightness.

We observed transversal fluctuations of the final position of the atoms with a standard deviation of approximately $\pm 5\mu\text{m}$. Deviations are probably caused by drifts in the various mirror mounts. To solve this problem, the beam path is actively stabilized by relaying the final beam position onto a quadrant photodiode. The resulting error signal, calculated from the measured intensity difference in the vertical or horizontal transverse direction, is fed back into a PID loop. The output of this control loop acts on two piezo-electric elements. They tip and tilt a mirror in the beam path such that the intensity is again equally distributed on the photodiode. After this improvement, the standard deviation in atom position is less than $1\mu\text{m}$. This corresponds to an angular accuracy of $4.4\cdot 10^{-5}$ ° in our setup.

3.8.4 Logarithmic power control for evaporation

After the atoms are transferred into the transport trap and transported to their final position, the final evaporation step is performed, again by decreasing the depth of the optical dipole potential [14, 61]. While the initial power for the transfer is 3.5W, it is lowered to values below 10mW during the evaporation. In order to make a laser power control work over four orders of magnitude, a logarithmic photo diode is employed to measure the actual power. The advantage is that even at very low optical powers, the voltage at the photodiode output is still sizeable. Hence, residual electronic noise (e.g. pickup in the cables) has less of a detrimental effect. The error signal obtained when comparing the two logarithmic power levels, the measured and set power values, is a relative error signal, which is proportional to a relative control signal. Yet in a PID loop, the control element, which changes the laser power, acts on an absolute control signal. The crucial step in a logarithmic PID control is to obtain a control signal proportional

to the absolute error. This is achieved by multiplying the relative error signal with the set signal using a variable gain amplifier.

Let us now follow the signal path of a logarithmic PID loop step by step: When a laser beam of the power P_m is measured with a logarithmic photo diode, the output signal m is proportional to the logarithm of the power, i.e. $m \sim \log P_m$. In the PID-loop, the measured signal m is compared to the set value s , which is the logarithm of the desired power P_s , i.e. $s \sim \log P_s$. In general, the difference between two logarithmic values approximately equals their relative difference r :

$$s - m = \log P_s - \log P_m \simeq r = (P_s - P_m)/P_s, \quad (3.18)$$

with $r \ll 1$. Since the control signal c at the output of a PID loop should be proportional to the absolute error $P_s - P_m$, the relative difference r must be multiplied by the set value P_s . This set value is only known in logarithmic form $s = \log P_s$. Hence, the control signal c must be obtained from:

$$c = -GrP_s = -Gr \exp(s), \quad (3.19)$$

with a PID gain G . Adjusting the offsets and base of the logarithmic amplifier and the variable gain amplifier proved to be quite challenging. In our case, the minimum level in power and therefore the dynamic range in the setup is limited by the dynamic range of the acousto-optic modulator driver: Even for a zero control signal, some RF-power reaches the acousto-optic modulator leading maximum extinction of the deflected power of 0.3mW or 10^{-4} .

3.9 Imaging Systems

Besides the high resolution imaging systems employing the two microscope objectives, we use several imaging systems [38, 75] along different directions to image atomic ensembles in the main chamber and in the glass cell, not only to perform experiments, but also to adjust and calibrate the apparatus. These conventional imaging setups consist of a collimated imaging laser beam, two lenses and a CCD camera and achieve a resolution of approximately $5\mu\text{m}$. Five conventional imaging setups were built to image the atoms during various stages of the cooling procedure (figure 3.13).

The first imaging setup is employed to collect fluorescence light on a photodiode for atom number calibration in the magneto-optical trap. To provide complementary information, two more imaging setups are used to measure the atom number in the magneto-optical trap, the resonator trap or the transport trap in the initial position. Finally, another two setups image the cloud at the final position of the transport trap, one in y - and one in x -direction.

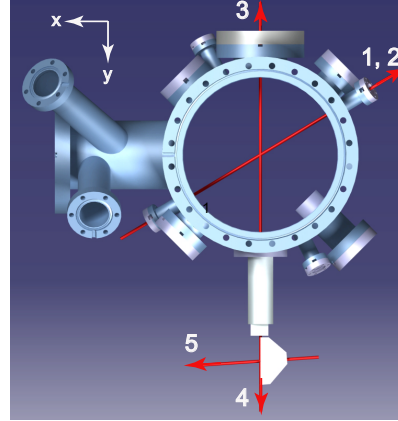


Figure 3.13: Top view of the main chamber and the partially cut glass cell with imaging laser beams to illustrate the imaging setups: fluorescence and absorption imaging (1,2,3) of atoms in the main chamber, and imaging in the glass cell in x - and y -directions in the glass cell (4,5).

3.10 Microscope Objectives

The heart of this experimental apparatus is the high resolution imaging setup, which allows us to measure density distributions and to shape dipole potentials down to a length scale of approximately 700nm . Two custom made microscope objectives are bolted onto actively stabilized mounts and axially aligned above and below a glass cell. The objective installed above the glass cell is used to shape dipole potentials, the one below reads out absorption and fluorescence. In order to obtain such a high resolution, the upper and lower windows of the glass cell are integrated into the optical system and are considered as two optical elements. The objectives are optimized for these windows such that the two foci overlap in the center of the glass cell and wave front distortions are kept below 7% rms, thus creating diffraction limited spots.

The whole mechanical and optical setup for microscopy needs to be designed in such a way that the adjustment of the objectives is not only feasible, but also reproducible and that long term drifts and vibrations on the length scale of the optical resolution are suppressed during operation. In addition, a rigidly built optical system to prepare imaging beams of clean transversal beam profile and an EMCCD camera with single photon sensitivity to detect the photon distribution are installed.

The following is an explanation of the optical setup, the mechanical setup for the two microscope objectives and their technical specifications.

3.10.1 Optical setup for microscopy

The optical system consists of three main components: the glass cell and the two microscope objectives. In addition, there are optical components to prepare beams for imaging and optical trapping.

The optics used to prepare laser beams for imaging and optical trapping, including the upper microscope objective, are mounted on a 20mm thick Vetroneit breadboard, supported by a 360mm tall aluminium construction that is totally separated from the magnetic field coil mounts. Single optical elements are aligned in cage systems to limit relative position deviations. In order to locally probe the gas, the imaging beam radius is enlarged and collimated by a telescope to a radius r of approximately 13mm, before it passes through the microscope objective. The clear aperture of the microscope objective is 20.8mm in diameter. Finally, spot sizes of approximately 700nm are achieved, which is the minimal length scale on which atoms can be illuminated. This resolution can only be obtained if the beam radius, collimation, the transversal mode profile as well as the angle and position of the microscope objectives are optimized. The rather long and complex alignment procedure will be explained in another work ([109] and references therein). The trapping beam, which is also radially enlarged and collimated to a radius of 13mm, is overlapped with the imaging beam. The polarization of the two beams can be adjusted separately.

For detection, optics including the lower microscope objective are mounted directly on the optical table. If atoms are imaged, the far off-resonant light to create dipole potentials is filtered out, while resonant imaging light is transmitted and magnified by a custom made telephoto objective and detected on a camera. If trapping potentials are imaged, the filter is taken out and resonant light is blocked.

With the configuration of two axially aligned microscope objectives, created optical potentials can be imaged, fitted and quantified experimentally. Moreover, there is a high flexibility for creating arbitrary potentials since none of the optical access of the upper microscope is taken up for detection.

3.10.2 Stable mounting

Experiments with fermionic lithium rely on relatively large and quickly changing magnetic fields that cause vibration, eddy currents and also thermal drifts due to ohmic heating of the magnetic field coils. At the same time, high resolution imaging requires a very stable mounting for the microscope objectives, with a stability on the same order as the optical resolution. The two microscope objectives are separately mounted to allow separate adjustment and relative positioning. They are totally disconnected from the magnetic field coil holder (figure 3.14). The objective mount above the glass cell is attached to the fibre glass bread-board supported by the aluminium construction, the one below is attached directly to the optics table.

The objective mounts include components for coarse and fine adjustment, which is realized in the following way: For coarse adjustment, both mounts consist of macor tubes with a fine thread to move the objectives in the vertical direction and a mechanical translation stage for movement in both horizontal directions, x and y . For fine adjustment and relative position adjustment, a three-axes translation stage driven by a piezo actuator is used with a positioning precision of 10nm ($7.2\mu\text{m}/\text{V}$ with the computer controlled set voltage). It is the only component of the mount that includes some magnetic parts. The angle between the microscope objectives and the glass cell can be set with a goniometer. Before two objectives were actually installed, the installation procedure had been practiced in a

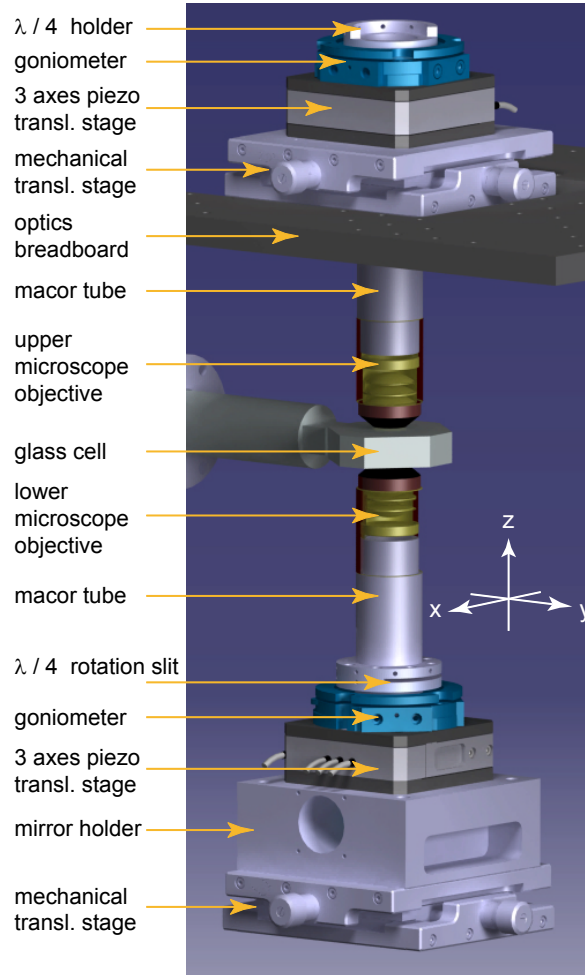


Figure 3.14: Mountings of the two microscope objectives above and below the glass cell. The optics breadboard is positioned 360mm above the experiment table.

test setup and technical specification were tested. Then the microscope objective was adjusted above and below the glass cell, following the adjustment scheme described above.

In order to image density distributions with a known resolution and maintain diffraction limited spot sizes needed for a controlled creation of dipole potentials, the mounting tolerances of the objectives must not be exceeded at any time. The only movement of the two microscope objective relative to each other that we observed was caused by temperature changes of the Feshbach coils and fast magnetic field ramps. While the relative movement caused by the temperature change appears within one hour after changing the magnetic field ramps in the experimental sequence, that caused by the fast ramps originates from the slightly magnetic three axes translation stages and happens during every magnetic field ramp. In order to keep the position of the microscope objectives stable, an active stabilization was implemented. The relative change in position between the microscope objective and their three axis translation stage during magnetic field ramps is measured by a strain gauge. Via a FPGA-based PID loop, the error in position is fed back to the piezo translation stage to automatically readjust the position.

3.10.3 Technical specifications of the objectives

The two microscope objectives employed are identical, custom designed, aligned and characterized by the manufacturer. They consist of 7 anti-reflection-coated lenses and are corrected for three wave lengths, 532nm, 671nm and 760nm. The effective focal length is 18mm and the working distance from the glass cell is 1.2mm. The field of view is $100 \times 100 \mu\text{m}^2$. Light transmitted through the lower microscope objective passes a custom made telephoto objective consisting of three lenses, before it is detected on an EMCCD camera. The numerical aperture of the whole optical system is 0.53 and the magnification is 54.

With both microscope objectives aligned along their common optical axis, a focal spot created by the first objective can be imaged by the second. Such a spot is shown in figure 3.15a. This allows us to characterize the created potential quantitatively: by fitting a Gauss function to the imaged photon distribution, in this case of light with a wavelength of 767nm, a spot size with a $1/e^2$ waist of $\omega_x = 734\text{nm}$ and $\omega_y = 726\text{nm}$ is experimentally obtained at a relative axial objective position $z = 0$. The position between the two objectives is tuned by the three axes piezo-driven translation stage to measure the Rayleigh length and astigmatism of the focussed beam (figure 3.15), which is approximately $2\mu\text{m}$.

In our case, to still obtain a diffraction-limited spot, the maximally allowed angular deviation of the objective axis to the perpendicular of the glass cell surface is 0.1° . The

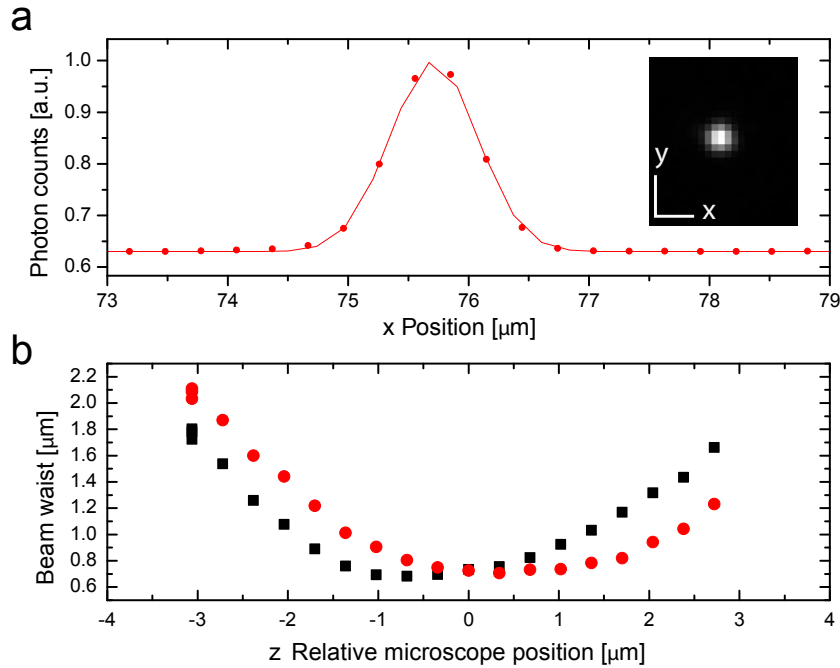


Figure 3.15: a. Image of a created focal spot (767nm) with an intensity distribution at the relative axial microscope position $z = 0$. b. Spot sizes, given by the fitted gaussian $1/e^2$ waist are plotted versus the relative axial microscope position z . There is an astigmatism of approximately $2\mu\text{m}$.

relative axial position shift for imaging a created focal spot is below the Rayleigh length of approximately $2\mu\text{m}$.

3.10.4 Detecting the photon distribution

For detecting the photon distribution either of created dipole potentials or fluorescence and absorption, a back illuminated CCD camera with an electron multiplier is used. This camera has single photon sensitivity, with maximally 53 counts per photon. The detector area is 512×512 pixels, each with size of $16 \times 16 \mu\text{m}^2$. Including the magnification of the imaging system, which is 54, the effective pixel size is only $300 \times 300 \text{nm}^2$, which is approximately half of the imaging resolution. The effective pixel size is only a relevant measure with respect to the optical resolution and the photon scattering cross section: With such a small effective pixel size, created spots as well as fluorescence and absorption signals can be well fitted. On the other hand, the atomic signal of scattered

photons is distributed over an area of the scattering cross section, which corresponds to approximately four pixels.

In order to suppress resonant stray light, different filtering techniques are applied. First, the microscope objective itself acts as a spatial filter, since it only collects photons of a limited solid angle. Far off resonant light at 767nm needed to create micro traps, which propagates in line with the resonant imaging light, is filtered out with an interference filter to an undetectably low photon signal. At the same time, transmission of resonant light is above 90%. Stray light close to 671nm, which is scattered onto the objective, is suppressed by covering the whole imaging system with black fabric.

3.10.5 Measuring dipole potentials with microscope objectives in line

One important advantage of a configuration with two microscope objectives, installed along the same optical axis, is that the intensity distribution of the trapping light created in and out of the focal plane can be measured. This allows us to determine the trapping potential of so-called micro traps into which atoms are then loaded. One example is given here.

In order to measure the non-saturated intensity distribution on a EMCCD camera, the trapping light is attenuated by a factor of about 10^{-3} to a few 10^{-9} W. The power of the original trapping beam is controlled by a logarithmic power control, which was also set up for the laser creating these micro potentials. Taking the transversal (figure 3.15a) and longitudinal (figure 3.15b) intensity distribution of the trapping light with a spot size of approximately 700nm, a Rayleigh length of $2.1\mu\text{m}$ and a beam power of $1\mu\text{W}$, a dipole potential for ${}^6\text{Li}$ atoms is obtained with a potential depth $U_0 = 200\text{nK}$, and radial and axial trapping frequencies $\nu_r = 7.60\text{kHz}$ and $\nu_x = 4.76\text{kHz}$. If we assume that the potential is a truncated harmonic trap, the approximate number of energy levels which could be populated at zero temperature is $N = 276$.

3.11 Magnetic field coils

For magneto-optical trapping, evaporative cooling, as well as for imaging atoms, several magnetic field coils are used. An overview is given in figure 3.16. All magnetic field coils are centered around the main chamber or the glass cell. They are mounted on a coil holder that is totally disconnected from the vacuum chamber and the optics to minimize vibrations during coil turn off. Depending on the operating current density, some coils are water-cooled. As a rule of thumb, wires of a coil are water-cooled from the outside if the current density exceeds $5\text{A}/\text{mm}^2$, while wires with a current density exceeding $10\text{A}/\text{mm}^2$ are water-cooled from the inside by using hollow wires. One power

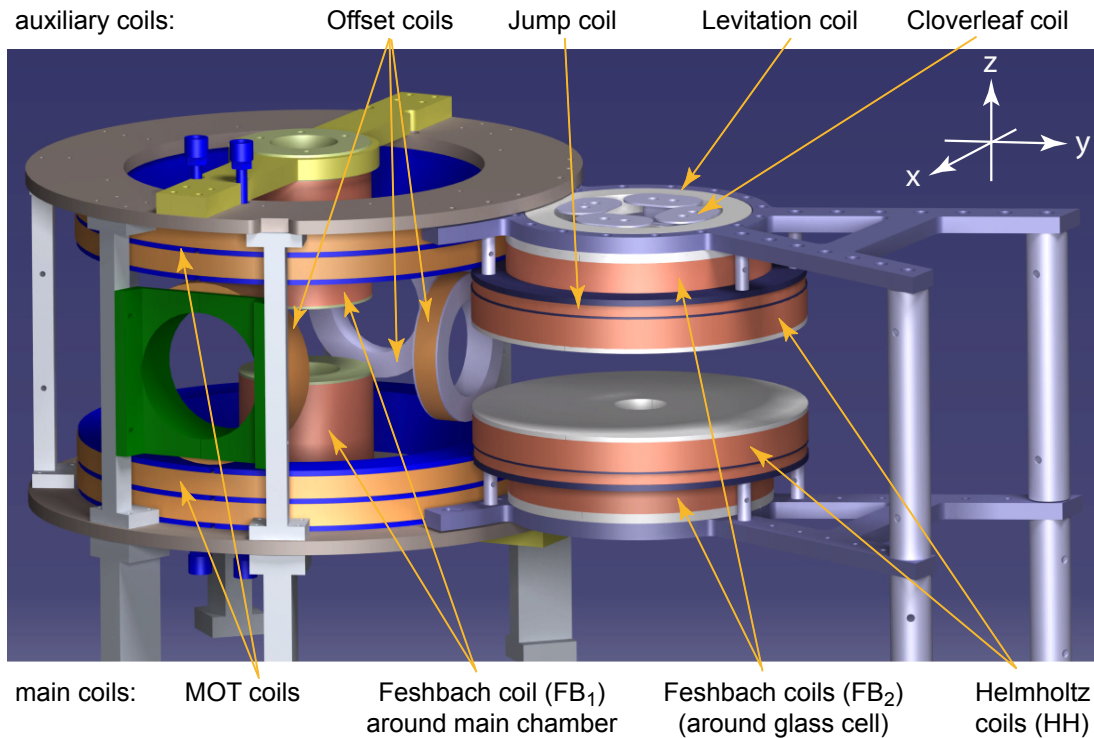


Figure 3.16: Overview of the magnetic field coils around the main chamber and the glass cell. Main coils are operated at currents above 10A to produce high magnitude magnetic fields. Auxiliary coils are operated up to 2A. Details of the magnetic field coils around the glass cell are shown in figure 3.17.

supply drives all coils that are operated at currents above 10A. Controlled magnetic field ramps are driven by a switch board with integrated PID loops for each coil. There are several auxiliary coils that are operated with separate commercially available power supplies.

The following present details about the different coil designs and the power supply. This subsection is summarized in table 3.3 on page 74, including the relevant data of the main coils implemented in the experiment.

3.11.1 Magnetic field coils for the magneto-optical trap

As explained in section 3.6.1, a magneto-optical trap makes use of a combination of laser light and a magnetic quadrupole field. To generate a quadrupole field, two magnetic field coils (MOT coils) in anti-Helmholtz configuration are placed around the main chamber. The direction and the shape of the quadrupole field is smoothly matched to the Zeeman slower field to optimize the loading efficiency (figure 3.5 on page 42). With

the large dimension of the main chamber (CF200 flanges with a diameter of 254mm) and the chosen MOT coil configuration, magnetic field gradients of $0.449 \frac{\text{G}}{\text{cm}}/\text{A}$ are realized. In our case, the ideal field gradients to trap lithium are 6.75G/cm in the x- and y-directions and -13.5G/cm in the z-direction (parallel to the axis of the two coils). At a corresponding operating current of 30A, current densities are 6A/mm². A coil holder with integrated water cooling is used to keep the wires from overheating.

The MOT coils are made out of 1 x 5 mm² high temperature doubly enamelled copper wire that is wound around a double-walled aluminium ring of a diameter of 288mm. The outer ring has three cooling ribs. The two coils between the cooling ribs, each containing 45 windings, are connected in series to form one MOT coil. Water is circulated around the coil axis in the double-walled aluminium ring to cool the 16 layers of wire. The coil could also permanently withstand higher current densities of up to 10A/mm².

The trapped atoms are centered around the zero point of the magnetic field. With so-called offset coils, the zero-point of the magnetic field, and hence the trap center, can be shifted in all directions to later overlap the magneto-optical trap with resonator dipole trap. Three such offset coils to move the trap center in the x- and y-directions are shown in figure 3.16. Two offset coils are wound around the Feshbach coils (FB₁ coil) to create a magnetic offset field in the z-direction. Currents up to 2A are supplied by commercially available power supplies that can be externally controlled.

3.11.2 Feshbach coils for the standing wave dipole trap

Evaporative cooling only works if the remaining atoms rethermalize in the dipole trap via elastic scattering. The scattering length is tuned with the magnetic field by accessing a Feshbach resonance to accelerate the thermalization process and efficiently cool atoms. In our experiment, we make use of the ⁶Li Feshbach resonance located at 834G. In order to create such magnetic fields with reasonable currents, two so-called Feshbach coils (FB₁) are placed as close as possible to the resonator dipole trap, in custom made recesses in the CF200 flanges outside of the vacuum chamber. The distance between the two coils of 57mm is set by the diameter of the laser beams for the magneto-optical trap and transport trap. Again, the coils are mounted totally independently from the main chamber. For the given coil configuration, a magnetic field of 3.5G/A is generated, which corresponds to a current of 238A at the magnetic field of 834G and a current density of approximately 15A/mm². Each coil consists of 99 windings and 4 layers of 4 x 4 mm² hollow copper wires with an inner diameter of 2.5mm. In a standard experimental cycle, efficient evaporative cooling of atoms is also achieved at 300G, where the scattering length reaches a local maximum of $|a| = 300a_0$. The coil pair is therefore usually operated at only 92A.

3.11.3 Magnetic field coils around the glass cell

In order to probe atomic ensembles in different states and therefore at different scattering lengths, magnetic fields need to be ramped to values of up to 1000G within milliseconds in each experimental cycle. The two main coil pairs around the glass cell that create these magnetic field magnitudes are the Feshbach coils (FB₂ coils) and the so-called Helmholtz coils (HH coils). The Feshbach coil pair (FB₂) is separated by 68mm. Each coil has a T-shaped cross section with 8 and 18 layers of 4x4mm² hollow copper wire and consists of 146 windings. In the given configuration a magnetic field of 8.629G/A is generated at the center of the glass cell. The hollow wires are cooled from the inside. This allows us to produce magnetic fields up to 2588G at a current of 300A, which is limited by the power supply. The Helmholtz coil pair (HH) is installed to generate magnetic fields of 5.42G/A with very low curvature at the center of the glass cell. The wires of the Helmholtz coils are wound onto the Feshbach coil (an exploded view of the two coils is shown in figure 3.17).

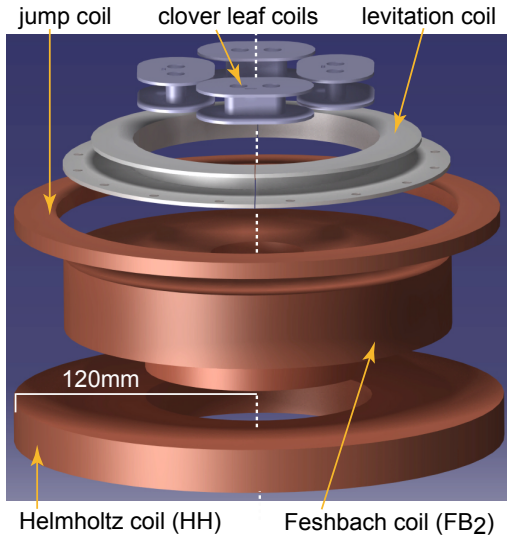


Figure 3.17: Exploded view of the upper set of coils around the glass cell. The two main coils are the Feshbach coil (FB₂) and the Helmholtz coil (HH). Auxiliary coils are the jump coil for fast switching, and the levitation and cloverleaf coils to add gradients.

Apart from coils to generate high magnitude magnetic fields, coils for fast switching and for field gradients are also required. There are different closely spaced coils set up around the glass cell to be operated with reasonably high currents without wasting the newly gained optical access: with a so-called jump coil pair, the magnetic field could be ramped much faster over a small range than the main coil due to its small inductance. Magnetic field gradients can be added with two levitation coils to compensate for gravitation, and eight clover leaf coils can create a gradient $\frac{\partial}{\partial r} B_z(r, z = 0)$ in the focal plane of the glass cell with a distance r from the microscope axis.

All coils have been tested, but so far only the Feshbach coil and the levitation coil have been in use. The current coil setup still leaves many possibilities.

3.11.4 Data of magnetic field coils

The previous sections are summarized by table 3.3, along with the data of the main magnetic field coils of this experimental apparatus:

Magnetic field coil parameters								
Coil	B/I [G/A]	B'_z/I [$\frac{\text{G}}{\text{cm}}/A$]	B''/I [$\frac{\text{G}}{\text{cm}^2}/A$]	R [Ω]	L [H]	wire mm^2	windings	water flow l/min
MOT	5.2	0.449		0.34		5 x 1	2 x 45	limited, 2.4
FB ₁	3.5			0.0292	$76 \cdot 10^{-6}$	4 x 4	99	0.53 at 6bar
FB ₂	8.629		0.4145	0.084	$980 \cdot 10^{-6}$	4 x 4	146	0.32 at 6bar
HH	5.42		~ 0	0.053	$314 \cdot 10^{-6}$	4 x 4	55	0.48 at 6bar

Table 3.3: Magnetic field and coil parameters of the magneto-optical trap coil (MOT), the Feshbach coils at the main chamber (FB₁) and the glass cell (FB₂), and the Helmholtz coils (HH). The relative magnitude B/I , the gradient B'_z/I and the curvature B''/I of the magnetic field are given for coil pairs in the actual configuration. The z -axis is the coil axis. The given values for the resistance R , the inductance L , winding numbers and water flow are with respect to a single coil.

3.11.5 Power supply

One versatile power supply operates the main magnetic field coils. Here an externally controlled switch mode power supply delivers currents up to 300A and voltages up to 80V with a maximal power limit of 9kW. Its internal current control time is approximately 50ms, which is rather slow for our experimental purposes. We increase this control time by implementing a switch box with an additional, much faster current control (approximately 1kHz). When turning a coil on, the power supply is first turned to a current set value, before the current is ramped to the set value by the switch box. This switch box consists of insulated gate bipolar transistors (IGBT), one for each coil pair. Although IGBTs are only made for fast switching, we managed to use them as tunable resistors for current control. Following is a description of the power supply used and of the basic idea of the IGBT driver.

Current control

In this experimental setup, the current source consists of three main components: the power supply, the IGBTs and a PID loops, which are schematically illustrated for one coil pair in figure 3.18. When the current through a coil pair is ramped up, the power

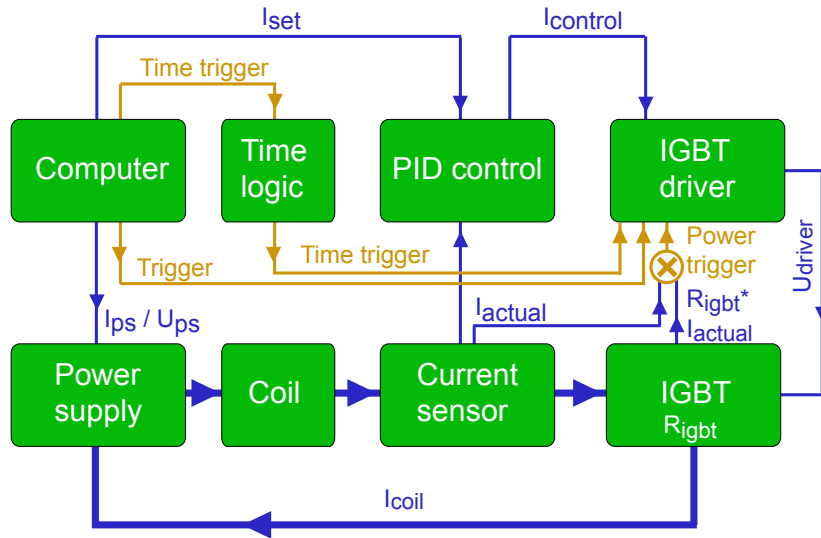


Figure 3.18: Schematic of the current control: the large current flowing through the coil is illustrated with a thick blue line. Analog signals of the PID loop and the external input of the power supply are blue, digital signals are brown. The control element is the IGBT whose resistance R_{igbt} is set such that $U_{ps} = R_{igbt} I_{set}$.

supply first is turned to a voltage value U_{ps} and a current value I_{ps} , while the IGBT is still closed. In order to obtain an actual controlled current I_{actual} , the resistance R_{igbt} of the corresponding IGBT is set via a PID loop such that the actual current is equal to the set current with $I_{actual} = I_{set} < I_{ps}$. To be able to control the current, I_{ps} has to be larger than the set value I_{set} and the power supply always has to be operated in the voltage limit with $U_{ps} = R_{igbt} I_{set}$. The control signal is determined by measuring the actual current value running through the coil with an external current sensor and comparing it to the set value.

If the voltage U_{ps} were too high, the IGBT would increase its resistance to keep the current at the set value and a large power dissipation would eventually destroy the IGBT. The IGBT is designed only for fast switching. Although the maximally allowed power dissipation is about 4.5kW, it cannot continuously dissipate such a power, even if the temperature of the device is kept constant. We found that as long as only a power of approximately 3kW is dissipated during a time of about 50ms, the IGBT will not be destroyed, even if being used for linear current control. Therefore, we implement an energy dissipation interlock, that integrates the dissipated power over time and closes the IGBT before it is destroyed. The dissipated energy is obtained by electronically multiplying the measured current and the voltage drop across the IGBT. In addition to

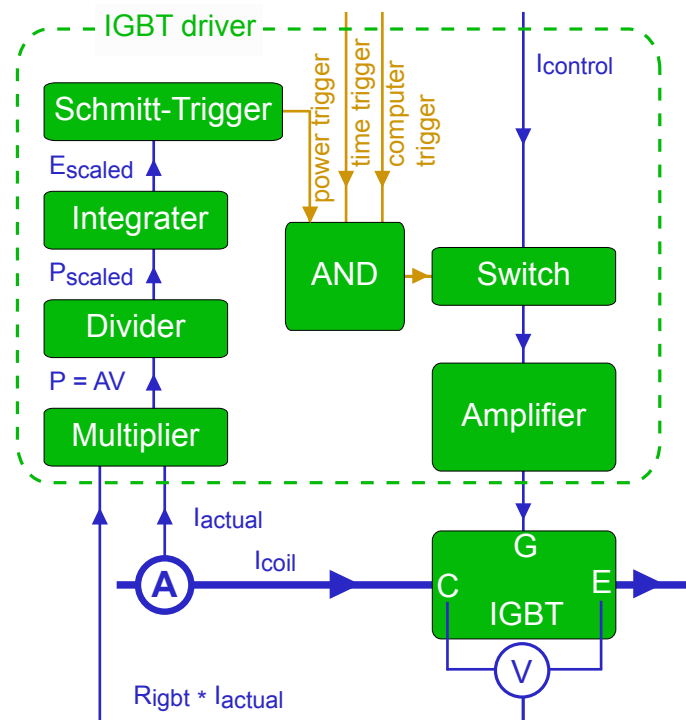


Figure 3.19: Schematic of an IGBT driver: The analog control signal $I_{control}$ is switched to zero, if either the computer-, time- or power trigger is zero. The power trigger is zero, if the scaled dissipated energy E_{scaled} in the IGBT exceeds $3\text{kW}\cdot 50\text{ms}$.

that power interlock, the maximal operation time of each coil pair is limited by a time logic to reduce the risk of overheating the coils. Induction voltages across the IGBT larger than 80V, which occur during coil turn off, are limited by varistors.

IGBT driver

Usually, IGBTs are only used for switching currents. According to data sheets, control voltages in the range between 0V to approximately 14V, i.e. a fully closed and fully open switch, must be avoided. With a newly designed driver working in the intermediate voltage regime, we managed to operate the power supply with the integrated current control. Its final version is schematically shown in figure 3.19.

The main component of the IGBT driver is a high-power amplifier to control the gate voltage of the IGBT. Due to the large capacity at the gate (G), fast current control is only feasible with an amplifier that can deliver currents up to 5A at the gate. Three logic channels, integrated in the driver, can turn the control signal $I_{control}$ to zero in order to close the IGBT. Two triggers set by the computer that controls the experiment,

are connected to the IGBT driver. The first trigger is directly connected to the logic of the driver. The second is first fed through an external time logic that limits the maximal turn on time of each coil pair, before it is connected to the driver. The third is a Schmitt-Trigger whose output is zero if the time integrated scaled power P_{scaled} , i.e. the dissipated energy E_{scaled} , is larger than a certain threshold value. The power P is given by the product of the voltage $V = R_{igbt}I_{actual}$ between collector (C) and emitter (E) and the measured current signal $A = I_{actual}$.

In order to adjust the power interlock, it is important to realize that the Schmitt-Trigger level as well as the time integrated power level needs to be adjusted such that the dissipated energy cannot exceed $3\text{kW}\cdot 50\text{ms}$. Since current sensors with different voltage-to-current ratios are used, the scaling factors between the actual dissipated power and the Schmitt-Trigger voltage level are also different for every coil pair.

3.12 Laser system

The first part of the cooling procedure, including Zeeman slowing and magneto-optical trapping as well as imaging of ${}^6\text{Li}$ atoms, makes use of resonant photon scattering. The cycling transitions $2^2S_{1/2} \rightarrow 2^2P_{3/2}$ of ${}^6\text{Li}$ are driven by red laser light with a wave length of $\lambda = 670.997\text{nm}$. The level structure of ${}^6\text{Li}$ is illustrated in the diagram (figure 3.20). Since there are two hyperfine ground states ($F=1/2$ and $F=3/2$) and three closely spaced excited states, which are considered as one combined excited state, ${}^6\text{Li}$ is treated as an actual three-level atom with two transition frequencies ν_1 and ν_2 separated by 228.2MHz .

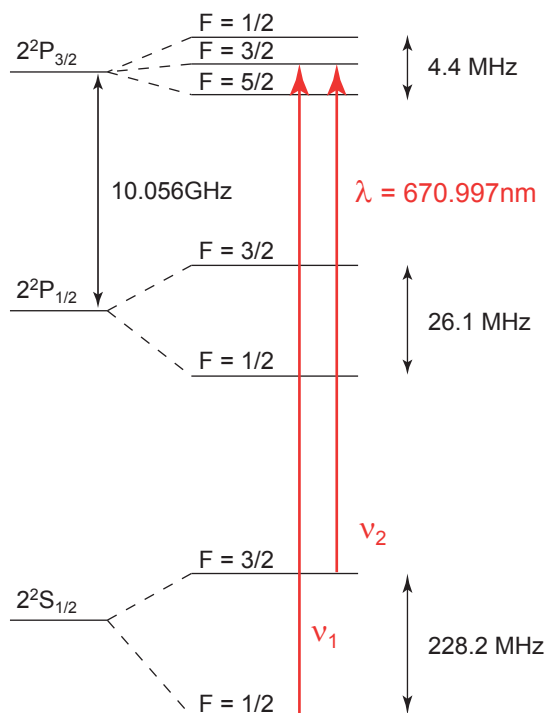


Figure 3.20: Level structure of ${}^6\text{Li}$ [101, 110]: The hyperfine spin states given by F , with $F \leq |J \pm I|$, where J is the electronic and orbital spin and $I = 1$ is the nuclear spin.

In order to maintain constant photon scattering rates, which set the corresponding light forces as well as the ratio of absorbed photons (relevant for absorption imaging), the frequency of the exciting laser are stabilized to a line width of about 1MHz, which is smaller than the natural, 6MHz line width of the excited state of ${}^6\text{Li}$. This corresponds to a relative frequency accuracy of 10^{-9} .

Laser light with different frequencies close to ν_1 and ν_2 , and linewidth of 1MHz are produced by grating stabilized diode lasers [111] and tapered amplifiers. One laser source serves as a frequency reference. Its frequency is stabilized to a spectral feature of lithium gained from a lock-in technique called frequency modulation spectroscopy [112]. The frequency of all the other laser sources are stabilized to that reference by an offset frequency lock-in technique [113].

The following is an explanation of the two lock-in techniques used here and of how laser frequencies and powers are set. The technical realization of the laser setup, including the characteristics of lasers sources and the ${}^6\text{Li}$ vapour cell are described in detail in another work [114].

3.12.1 Lock-in technique for the reference laser

For stabilizing the laser frequencies to a reference frequency, first an error signal that can be used as a frequency standard needs to be created. Here, the error signal is gained from frequency modulation spectroscopy, which combines spectroscopy and a frequency lock-in technique [112]. Frequency fluctuations are then fed back to the frequency control element of the diode laser, which is a piezo actuator that tunes the length of an external laser cavity [111] and hence the frequency.

In order to obtain an error signal serving as a frequency standard, a phase modulated laser beam with a carrier frequency and two sidebands $\nu \pm \nu_m$ passes through a lithium vapour cell to probe the spectral features of lithium. The generated sidebands at $\nu \pm \nu_m$ experience different phase shifts $\varphi(\nu \pm \nu_m)$ if the laser frequency ν_m is tuned over a resonance feature. The same lock-in technique as the Pound-Drever-Hall technique (section 3.7.4) is now used: the beat signal at frequency $\pm \nu_m$ occurring between the carrier and the two sideband is detected by a photo diode. This beat signal is then demodulated with the local oscillator frequency ν_m to obtain a dispersion-like DC error signal (a linear function in frequency that vanishes at resonance), while the frequency component at $2\nu_m$ is filtered out. The resulting control signal of the PID loop, which is proportional to the error signal, adjusts the external cavity length and hence the laser frequency. Here, the dispersion feature used for frequency stabilisation is called crossover, which is a peculiarity of the so-called Doppler-free saturation spectroscopy. The crossover frequency ν_{co} is approximately the mean of the two transition frequencies ν_1 and ν_2 (see figure 3.20), which is $\nu_{co} = \nu_1 - 114.1\text{MHz} = \nu_2 + 114.1\text{MHz}$.

3.12.2 Offset lock-in technique

If a laser frequency is stabilized to the reference laser with fixed offset frequency, the offset lock-in technique is used [113]. Its error signal is generated in the following way: the beat frequency $\Delta\nu$ between the reference laser and the offset laser frequency is detected on a photodiode and mixed with a certain set frequency $\Delta\nu_{set}$. While the frequency component $\Delta\nu + \Delta\nu_s$ is attenuated by a low-pass filter, the mixed signal $\Delta\nu_{mix} = \Delta\nu - \Delta\nu_{set}$ is split into two branches. The lock-in technique is now applied: one part of the signal is transmitted through a radio-frequency cable serving as a frequency dependent delay line to accumulate an extra phase before it is mixed again with the original signal, which serves as a local oscillator. After passing a low-pass filter, we obtain a frequency dependent DC error signal, which is proportional to $\cos(\varphi(\Delta\nu))$, where $\varphi(\Delta\nu)$ is the phase lag experiences in the delay line. As described in the previous section, the resulting error signal is used to adjust the external cavity length of the diode laser [111], which in turn sets the laser frequency.

3.12.3 Laser setup

For Zeeman slowing, magneto-optical trapping as well as for imaging, frequency stabilized laser sources are set up, each with a specific laser frequency and power. There is one laser source providing light that serves as a frequency reference. The frequency of this reference laser light is stabilized via frequency modulation spectroscopy to the crossover frequency of ${}^6\text{Li}$. Frequencies of the light produced by other lasers are stabilized via offset locks. The laser power is obtained with different types of diode lasers. The diode laser setups with an external cavity provide light with power up to 25mW, while tapered amplifier diode lasers can amplify input laser powers between 12mW to 18mW up to 500mW. For technical reasons, the light of the diode lasers is coupled into single mode optical fibres, where the transversal mode is cleaned. About 50% of the laser output power is transmitted through the fibre.

The following is an explanation of how components are arranged in order to obtain all the required frequencies and powers. The laser setup is summarized in figure 3.21. This section is intended for practical use.

Reference diode laser

The frequency standard to which the reference laser is stabilized, is the crossover frequency ν_{co} , which lies approximately in between the transitions ν_1 and ν_2 , with $\nu_{co} = \nu_1 - 114\text{MHz} = \nu_2 + 114\text{MHz}$. The laser source that sets the frequency reference is a diode laser with a power of about 20mW. Its frequency is first shifted 200MHz to

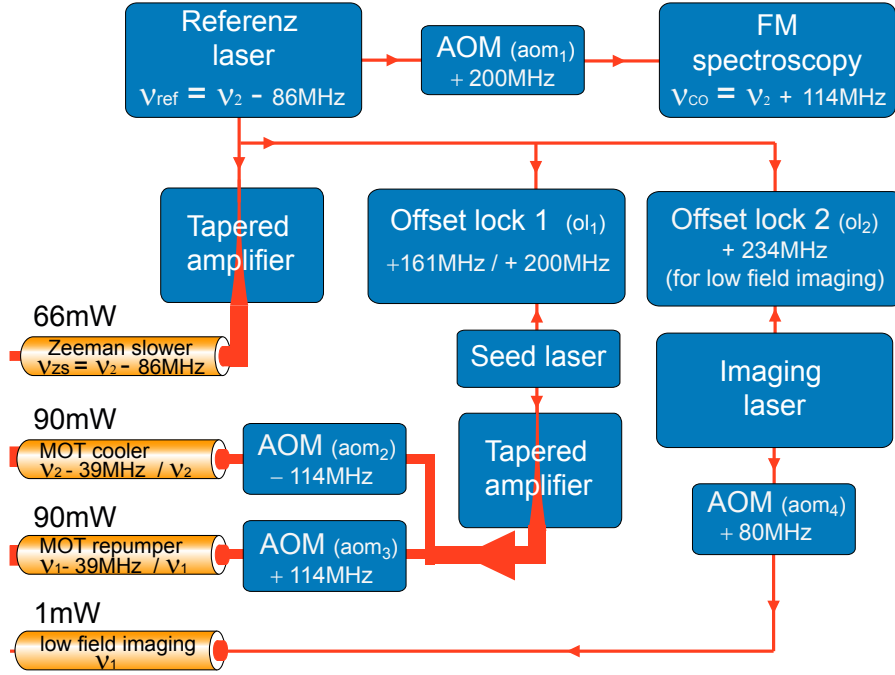


Figure 3.21: The laser setup producing resonant light for Zeeman slowing, magneto-optical trapping and imaging, consists of three diode lasers and two tapered amplifiers. Laser frequencies and powers are indicated at the output of the optical fibres. The frequency standard is the crossover frequency ν_{co} , obtained from frequency modulation spectroscopy. Seed and imaging laser frequencies are offset-locked to the reference laser frequency ν_{ref} .

the red by an acousto-optical modulator of frequency ν_{aom_1} , before it is stabilized to the crossover. This results in a frequency reference $\nu_{ref} = \nu_{co} - \nu_{aom_1} = \nu_2 - 86\text{MHz}$.

Tapered amplifier for Zeeman slowing

As explained in section 3.3.1, the atomic beam is decelerated by the Zeeman slower laser beam, whose power is such that the scattering rate is higher than $\frac{\Gamma}{4}$ everywhere along the atomic beam axis. This corresponds to a minimum power of 20mW. Here, the Zeeman slower is operated at a power of 66mW. In order to obtain a final velocity of 60m/s, the laser frequency ν_{zs} needs to be 86MHz below the transition frequency ν_2 . A tapered amplifier is seeded by the reference laser, whose frequency ν_{ref} is equal to $\nu_{zs} = \nu_2 - 86\text{MHz}$.

Seed laser and tapered amplifier for magneto-optical trapping

As explained in section 3.6.1 and shown in figure 3.20, fermionic lithium can be regarded as an actual-three level system. Two laser frequencies ν_1 and ν_2 , which are detuned to the red by $\Delta_{min} = 3\text{MHz}$ to $\Delta_{max} = 39\text{MHz}$, are needed to keep lithium atoms in a cycling transition for magneto-optical trapping. The detuning Δ depends on the required size of the atomic cloud. The resulting frequencies are $\nu_{mot_{1,2}} = \nu_{1,2} - \Delta$. The power in each frequency component and each beam is equal, adding up to 180mW.

In order to obtain laser light with such frequencies and power, the frequency of a diode laser is first offset-locked to the reference frequency with a frequency difference ν_{ol_1} , before a tapered amplifier is seeded. Afterwards, the amplified laser beam is split into two branches. By means of an acousto-optical modulator, the frequency of one is shifted by $\nu_{aom_2} = -114\text{MHz}$ to red, that of the other by $\nu_{aom_3} = +114\text{MHz}$ to the blue, to finally obtain the needed laser frequencies $\nu_{mot_{1,2}} = \nu_{1,2} - \Delta = \nu_{ref} + \nu_{ol_1} + \nu_{aom_{2,3}}$, with $162\text{MHz} < \nu_{ol_1} < 197\text{MHz}$. For the cooling procedure in the case of lithium to finally obtain an ultra-cold gas it is crucial to be able to tune the relative power between the two frequency components and their exact turn off times at the end of the magneto-optical trapping phase (section 4). Therefore, the two acousto-optical modulators have been built into the laser system.

Diode laser for imaging

In order to resonantly illuminate an atomic ensemble at zero magnetic field for measuring absorption or fluorescence (henceforth simply called imaging), either the transition ν_1 or ν_2 is driven. Imaging is done by switching the illumination light on and off within $4\mu\text{s}$ to $20\mu\text{s}$ with an acousto-optical modulator (aom_4). This AOM shifts the laser frequency by 80MHz to the red. The imaging laser frequency is offset-locked to the reference with an offset lock frequency ν_{ol_2} . For low field imaging of atoms, the frequencies $\nu_{1,2} = \nu_{ref} + \nu_{ol_2} - 80\text{MHz}$ are obtained by choosing an offset lock frequency $\nu_{ol_2} = 234\text{MHz}$ and 6MHz, respectively. Since atoms are transferred into the $2^2S_{1/2}, F=1/2$ state at the end of the magneto-optical trapping phase, only the offset frequency $\nu_{ol_2} = 234\text{MHz}$ is relevant for low field imaging.

In the case of imaging atoms at non zero magnetic fields, the magnetic field dependence of the energy levels needs to be taken into account. The energy levels split into Zeeman sublevels, which are shown in figure 3.22. By illuminating atoms populating one of the ground states $|1\rangle$, $|2\rangle$ and $|3\rangle$ with circularly polarized σ_+ light, transitions $|1\rangle \rightarrow |1'\rangle$, $|2\rangle \rightarrow |2'\rangle$ and $|3\rangle \rightarrow |3'\rangle$ are driven.

Due to the different slopes in the energy shift between ground and excited state, the corresponding offset lock frequencies ν_{ol_2} depend on the magnetic field. In order to drive

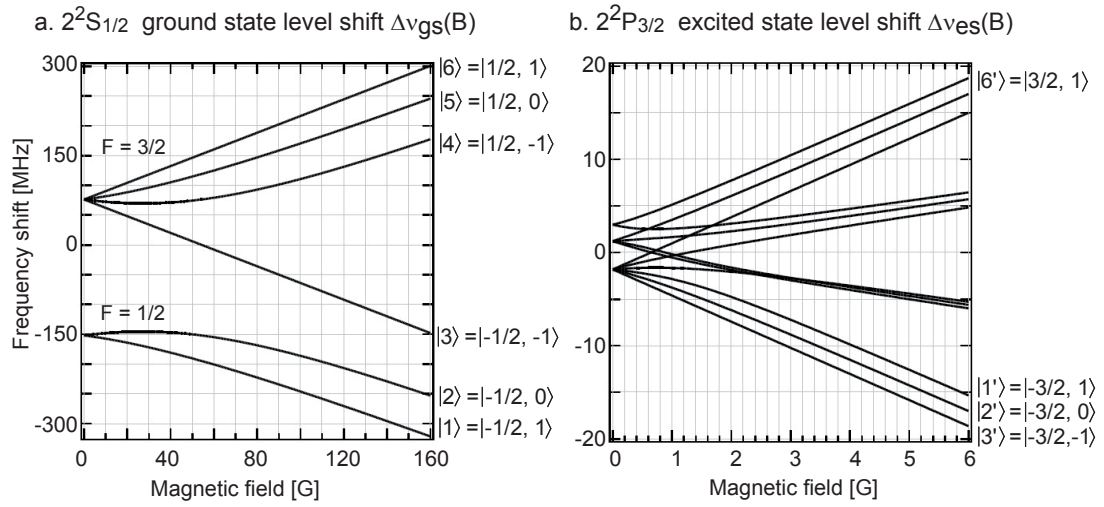


Figure 3.22: Zeeman splitting of ground and excited state levels [101, 110]. Imaging transitions of atoms in the ground state are $|a\rangle \rightarrow |a'\rangle$, with $a = 1, 2, 3$. Only the transitions $|3\rangle \rightarrow |3'\rangle$ and $|6\rangle \rightarrow |6'\rangle$ are closed transitions. The latter is driven during Zeeman slowing of atoms.

the above described cycling transitions, ν_{ol_2} needs to be tuned to

$$\nu_{|1,2\rangle \rightarrow |1',2'\rangle}(B) = 234\text{MHz} + \Delta\nu_{gs}(B) - \Delta\nu_{es}(B) < \nu_1 \quad (3.20)$$

and

$$\nu_{|3\rangle \rightarrow |3'\rangle}(B) = 6\text{MHz} + \Delta\nu_{gs}(B) - \Delta\nu_{es}(B) < \nu_2, \quad (3.21)$$

respectively. Atoms are imaged at externally applied magnetic fields, which vary from 0 to 900G, which corresponds to a frequency shift up to approximately -1.26GHz. This range is covered by the offset lock ol_2 .

4 Performance of the apparatus

Being able to control the smooth interplay of the many newly developed components of this experimental apparatus to prepare and image degenerate fermionic ensembles determines its performance. Each component was tested and the time sequence of the preparation procedure was optimized. This is of particular importance, because after every measurement, which destroys the initial state of the atoms, a new experimental sequence starts. The experimental apparatus must not only prepare and image a new atomic ensemble in exactly the same manner, but also in the shortest possible time in order to obtain reliable data.

The following is a description of an optimized experimental standard sequence. A programmed time sequence controls laser light and magnetic fields, and also triggers externally controlled devices via analog and digital channels to cool, transport and image an atomic ensembles. At the end of each sequence, pictures of illuminated atoms are made, from which information about physical quantities is gained.

Prime examples of degenerate Fermi gases, such as non-interacting Fermi gases and molecular Bose-Einstein condensates, are presented and their density distribution, from which the temperature is extracted, are shown.

4.1 Experimental preparation of an ultra-cold Fermi gas of Li6

A standard experimental sequence lasts about 15s with an additional delay of 2s for data processing and analysis. Each cycle starts with the magneto-optical trapping phase [14, 59, 60], during which atoms are cooled from 670°K to about 140 μ K, which is the Doppler limit.

Atoms which are evaporated from the oven, collimated to a beam and Zeeman slowed, are magneto-optically trapped at a maximum velocity of 60m/s. With laser light at saturation intensity and a frequency detuning $\Delta = -6.5\Gamma$ below resonance, approximately 10^{10} atoms are trapped after a loading time of 4s (figure 4.1). This atom number is

mainly set by the loading rate, i.e. the effective flux of the atomic beam, and the loss rate, which is governed only by the collisional loss rate of lithium atoms inside the magneto-optical trap.

The loss rate caused by scattering with atoms of the background gas can be neglected totally, because the life time of the magneto-optically trapped atomic ensemble is approximately 15minutes. At the end of the trapping phase, the laser beam and the magnetic field coils of the Zeeman slower are turned off.

The second part of the experimental cycle is the evaporation phase [61, 14], during which atoms are cooled from about $140\mu\text{K}$ to about 200nK , which is below Fermi temperature in our case. While sub-Doppler cooling is very efficient for other alkali atoms, it is not applicable in the case of lithium [105].

A relatively hot atomic ensemble is transferred into the resonator dipole trap [58, 62], where resonant photon scattering is largely suppressed and much lower temperatures can be achieved. First, magneto-optically trapped atoms are shifted in position and compressed to achieve good spatial overlap with the resonator dipole trap.

The position of the atomic ensemble is set by moving the zero point of the magnetic gradient field with the three offset coils pairs that are set up in each direction. In order to compress the atomic cloud, the frequencies of the magneto-optical trapping light is tuned to $\nu_{mot_{1,2}} = \nu_{1,2} - \Delta$, with $\Delta = -1\Gamma$. The atomic ensemble has now a diameter of only about 1mm. Due to enhanced resonant photon scattering, inelastic loss rates increase and the lifetime of the atomic ensemble is significantly shortened to a millisecond timescale. Before the magneto-optical trap is turned off, atoms populating the $2^2S_{1/2}, F=3/2$ state are transferred to the $2^2S_{1/2}, F=1/2$ hyperfine ground state to reduce inelastic collisions [62] occurring between the Zeeman substates [1]

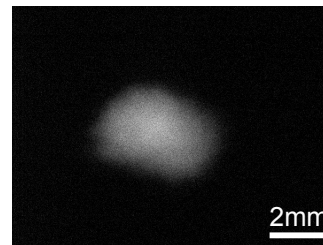


Figure 4.1: Fluorescence image of 10^{10} magneto-optically trapped atoms, detected at a laser frequency detuning of $\Delta = -3\Gamma$.

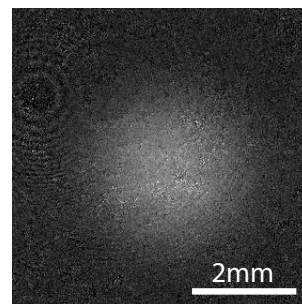


Figure 4.2: Absorption image of $3.5 \cdot 10^7$ atoms after 3ms expansion from the resonator dipole trap.

and $|2\rangle$, and higher lying states, in further cooling steps at higher magnetic fields.

This transfer is done by reducing the power of the repumper light (with frequency $\nu_{mot_1} = \nu_1 - \Delta$) that drives the transition $2^2S_{1/2}, F = 1/2 \rightarrow 2^2P_{3/2}, F = 3/2$ during 8ms, such that only the state $F = 1/2$ is populated, which is a so-called dark state and does not couple to the light field. Finally, the two energetically lowest Zeeman substates $|1\rangle$ and $|2\rangle$ will be occupied, whose scattering length a can be precisely tuned. After the laser light and magnetic field gradients for magneto-optical trapping are turned off, about 0.5% or $5 \cdot 10^7$ atoms remain in the resonator dipole trap, which was already turned on during the magneto-optical trapping phase (figure 4.2). According to the intensity inside the resonator, the atomic ensemble inside the resonator trap has a maximal temperature of about $46\mu\text{K}$. The evaporation process is started by turning the Feshbach (FB_1) coils on. At currents of 92A and a corresponding magnetic field of 322G, the scattering length between the two spin states $|1\rangle$ and $|2\rangle$ is approximately $-300a_0$, which is large enough for efficient evaporative cooling in our case.

Within 2.7s, the light power inside the resonator is exponentially decreased to 20% of the initial power. About $2 \cdot 10^7$ of the atoms initially loaded remain. Before the first part of the evaporation phase in the optical resonator started, the transport dipole trap was turned on. In the overlap region between the two traps, about $1.5 \cdot 10^6$ atoms are transferred into the transport trap (figure 4.3 and 4.4) at an initial laser power of 3.5W, which corresponds to a potential depth of approximately $k_B 300\mu\text{K}$. Since the atoms are confined in the radial as well as in the axial direction of the focused laser beam, they can be moved to the glass cell by simply translating the focussing lens [64]. The laser light coupled into the resonator, and the current through the Feshbach coils need

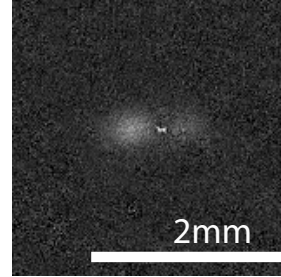


Figure 4.3: Absorption image of atoms along the transport axis: Atoms transferred to the transport trap are visible on a few bright pixels in the center of the image, while the other atoms are freely expanding from the resonator dipole trap.

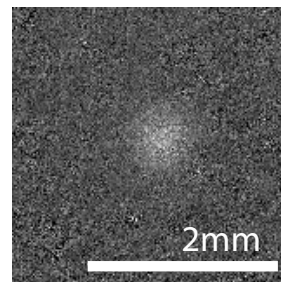


Figure 4.4: Absorption image of approximately $1.4 \cdot 10^6$ atoms after 2ms of free expansion from the transport trap.

to be turned off first. Both, the standing wave potential of the resonator as well as the magnetic potential would inhibit an atomic motion in the transport direction.

Before transport, the laser power is decreased from 3.5W to 2W to reduce the resonant scattering which would heat the atomic ensemble. Finally, atoms are moved to the glass cell. In the final position, transversal position deviations are automatically readjusted to the position of the magnetic field maximum of the Feshbach coil pair (FB₂) around the glass cell center. In order to start the final evaporation, the current in the Feshbach coil pair at the glass cell is raised to 35A, which corresponds to 302G and a scattering length of approximately $300a_0$. Within a total evaporation time of 3.1s, the power of the transport laser beam is reduced to values of around 10mW. At the corresponding trap depth, the atomic ensemble reaches degeneracy: $3 \cdot 10^5$ lithium atoms at a temperature of 200nK and $0.16T/T_F$ reveal the fermionic statistics. Depending on the magnetic field, either a non-interacting Fermi gas or a strongly-interacting Fermi gas, which is superfluid at these temperatures, is formed.

4.2 Characterization of the preparation procedure

In order to obtain reliable data after each experimental cycle and to efficiently operate this experimental apparatus, a significant part of the work for this thesis was to optimize the various preparation and measurement techniques, finally resulting in the standard experimental cycle explained in the previous section.

A few key points of the optimization procedure are presented in the following section. The data shown reflect the optimization procedure applied here, which basically involves two tasks: First experimental parameters of the apparatus which are critical with respect to the atom number and the temperature have been identified. The accuracy of these parameters needs to be such that fluctuations in atom number and temperature are minimized. In a second step, the whole optimization mainly focuses on achieving a small final absolute temperature T , a high atom number N and for practical reasons, a short experimental cycle time t . Although we are able to detect small atom numbers, a large initial number of atoms in the transport trap is required to obtain a degenerate Fermi gas after evaporation.

4.2.1 Loading the Magneto-optical trap

Approximately 10^{10} atoms are magneto-optically trapped at a phase space density ρ of approximately 10^{-6} [115]. After this initial trapping and cooling phase, atoms are transferred to two different types of dipole traps and are evaporatively cooled, resulting in a major particle loss. In order to reach degeneracy ($\rho = 1$) with a final atom number

of approximately $3 \cdot 10^5$, a large initial atom number in the magneto-optical trap is crucial.

In order to efficiently trap a large number of atoms in a short time, the ratio between the loading and loss rate l_+ and l_- needs to be maximized. Resonant light forces are adjusted such that atoms with an initial velocity at 60m/s are decelerated and trapped to obtain a high loading rate. When atoms traverse the magnetic gradient field, they are in resonance with laser light only at positions $x \sim \Delta/B'$. In this ellipsoidal shell, atoms are trapped. By tuning the frequency difference Δ closer to zero, trap volume V_{mot} decreases and hence the density $n = N/V_{mot}$ increases. This results in a reduced loading rate l_+ due to a limited density n_{max} and an enhanced loss rate l_- , which is mainly caused by inelastic collisions between trapped atoms in the ground and the excited state. At a small density ($\Delta = -6.5\Gamma$), the life time of the magneto-optically trapped ensemble is approximately 15min. So, losses occurring due to collisions between trapped atoms as well as with the background gas can be neglected. At a high density corresponding to a small frequency detuning $\Delta < -1\Gamma$, the life time is reduced to milliseconds.

The ratio between loading and loss rate l_+/l_- is optimized by measuring the atom number $N_{mot}(\Delta, t)$ for different frequency detunings Δ and after different loading times t . This is done by collecting the fluorescence on a calibrated CCD camera, which is here used as a photo diode (figure 4.5a). Before detecting the fluorescence signal in a time span of $32\mu s$, the laser frequency is tuned to -3Γ (-18MHz) to compress the atomic ensemble and to increase the scattering rate. According to a rate equation including loading and loss rates [116], the atom number $N_{mot}(\Delta = -6.5\Gamma, t)$ can be expressed by

$$N_{mot}(t) = N_{mot,max} \left(1 - \exp\left(-\frac{t}{\tau_{mot}}\right) \right). \quad (4.1)$$

The maximal atom number is determined by the equilibrium condition, where the loading and the loss rates achieve a balance: $N_{mot,max} = l_+/l_-$. By fitting this function to the measured data (figure 4.5b), one obtains a threshold value of the maximally trappable atom number $N_{mot,max} = 4 \cdot 10^{10}$ and the characteristic loading time $\tau_{mot} = 11.5s$ for a certain set of experimental parameters given in table 4.1. The loading rate l_+ is approximately $2 \cdot 10^9/s$. In figure 4.5c, the atom number $N_{mot}(\Delta, t = 4s)$, which is proportional to l_+/l_- , is shown with respect to the frequency detuning Δ during loading. For frequency differences larger than $\Delta = -8.5\Gamma$, the magneto-optical trap volume increases such that the trapping region becomes larger than the laser beam radii. The loading rate l_+ drops to zero. In an intermediate regime between -8Γ and -6Γ , the ratio between loading and loss rate l_+/l_- is best. Very close to resonance with $\Delta < -3\Gamma$, magneto-optical trapping is inefficient for two reasons: the loading rate l_+ drops, because the trap volume is too small and light forces of two counter-propagating

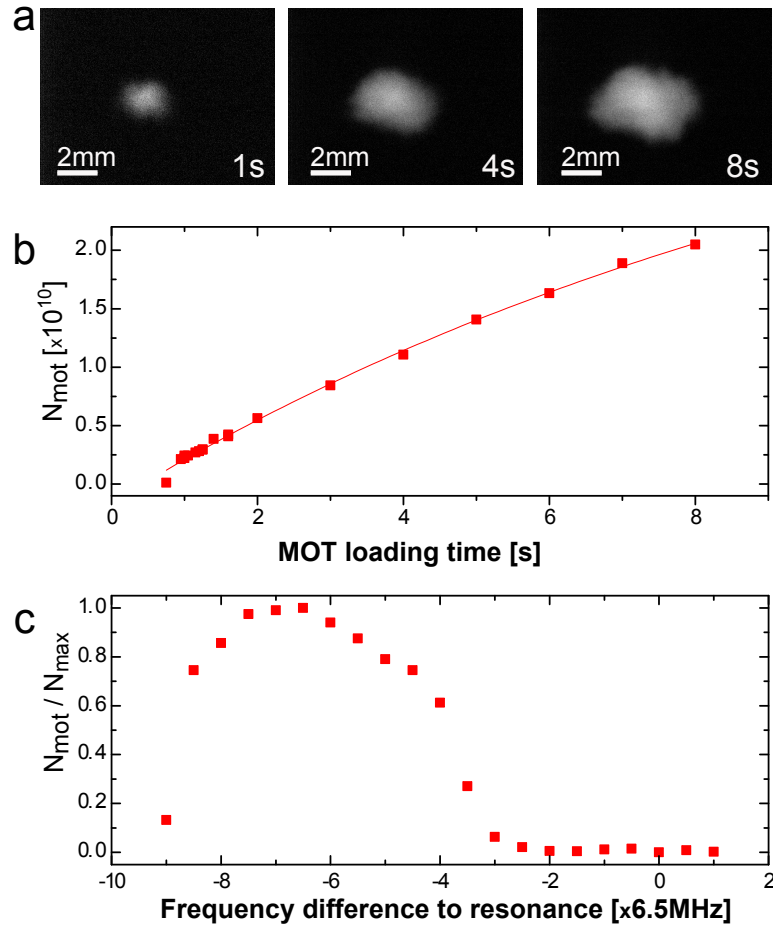


Figure 4.5: Loading of the magneto-optical trap. a. Fluorescence pictures of trapped atoms after different loading times. b. Loading curve $N_{mot}(\Delta = -6.5\Gamma, t)$ with a loading time $\tau_{mot} = 11.5\text{s}$ and a maximal atom number $N_{mot,max} = 4 \cdot 10^{10}$. c. Atom number $N_{mot}(\Delta, t = 4\text{s}) \sim l_+/l_-$ trapped at different frequency detunings Δ .

laser beams are resonant at the same position in space and start to cancel each other. The loss rate l_- is strongly enhanced due to the small volume of the trap.

4.2.2 Transfer into the standing wave dipole trap

The magneto-optically trapped atoms are transferred into the resonator dipole trap to reduce heating caused by resonant photon scattering. In order to achieve similar trap volume and depth for efficient transfer, the laser power inside the resonator dipole trap is turned to its maximum of 158W corresponding to a potential depth of $k_B 11\mu\text{K}$ and the atomic ensemble is compressed to approximately 1mm in diameter, which is

Magneto-optical trapping parameters	
oven temperature	402°C
cone temperature	267°C
nozzle temperature	300°C
Zeeman slower laser power	66mW
MOT laser power: ν_{mot_1} (repumper) / ν_{mot_2} (cooler)	92mW / 85mW
MOT loading frequency detuning Δ	$-6.5\Gamma = -39MHz$
magnetic field gradients	6.75G/cm and $-13.5G/cm$

Table 4.1: Magneto-optical trapping parameters

done by tuning the laser frequency difference Δ from $-6.5\Gamma = -39MHz$ to only $-1 = -6MHz$ within 10ms. The compression time needs to be short compared to the life time of the atomic ensemble to limited inelastic losses. In a narrow range of about $\pm 0.3\Gamma = \pm 2MHz$, we find the best ratio between particle losses and good overlap with the standing wave dipole trap. Approximately $5 \cdot 10^7$ or 0.5% of the magneto-optically trapped atoms are then transferred.

The number of atoms N_{res} transferred to the resonator dipole trap is here measured by absorption imaging atoms after 3.5ms of free expansion from the trapping potential and fitting a gaussian function to the density distribution (figure 4.6a). $N_{res}(N_{mot})$ exponentially scales with the magneto-optically trapped atom number N_{mot} (figure 4.6b). For optimized parameters, the atom number threshold is $N_{res,max} = 8.6 \cdot 10^7$. The characteristic loading time $\tau_{res} = 4.5s$, which includes simultaneous loading of the magneto-optical trap, is obtained by measuring $N_{res}(t)$ and by fitting the function given in equation 4.1 to the data.

With the ideal parameters for compression and a loading time of 4s, the atom number $N_{res}(U_0)$ is now measured with respect to the initial potential depth U_0 of the resonator dipole trap for transfer. We observe an atom number dependance $N_{res}(U_0) \sim U_0^{1.61 \pm 0.13}$ (figure 4.6c), which is expected from the decrease in density of states given by

$$N_{res}(U_0) = \int \rho(\varepsilon) d\varepsilon \sim \sqrt{U_0}^3 \int \sqrt{u(x)}^3 dx^3 \sim \sqrt{U_0}^3 \quad (4.2)$$

with the scaled potential $U_{res}(x) = U_0 u(x)$.

Once atoms are trapped in the resonator dipole trap, heating caused by resonant photon scattering is largely suppressed. Now, heating processes are governed by frequency and intensity noise of the laser source. Here we characterize the atomic loss rate by measuring the trapped atom number $N_{res}(a, t)$ after different hold times t (figure 4.7) for two different scattering length a . Measured data is fitted to an exponential loss

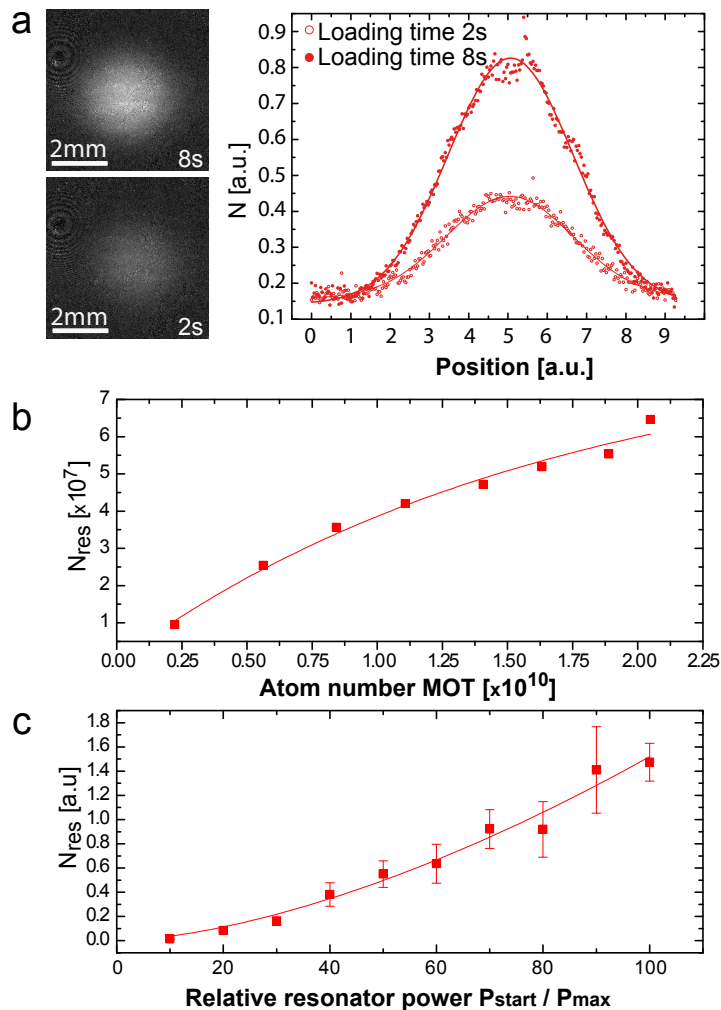


Figure 4.6: Atom number after transfer into the resonator dipole trap. a. Absorption image after 3.5ms of expansion from trap for 2s and 8s loading time (left) with the corresponding horizontally integrated density distributions to extract atom numbers N_{res} (right). b. Number $N_{res}(N_{mot})$ of transferred atoms with respect to the magneto-optically trapped atom number. The maximal transfer efficiency is approximately 0.5%. c. Atom number $N_{res}(U_0)$ with respect to the initial resonator trap depth, scaling with $U_0^{3/2}$.

curve [62], which is given by

$$N_{res}(t) = N_{res,max} \exp\left(\frac{-t}{\tau_{res}}\right). \quad (4.3)$$

The life time $\tau_{res,0a_0}$ of the atomic ensemble obtained at the maximal potential depth

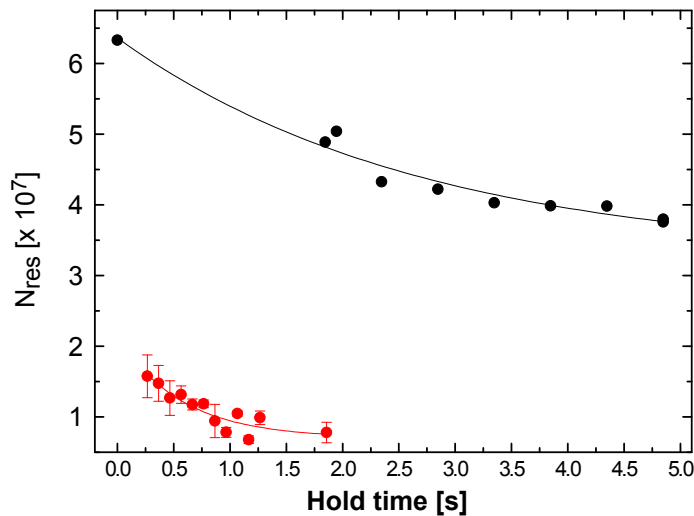


Figure 4.7: Atom loss in the resonator dipole trap. The life time of the atomic ensemble is $\tau_{res,0a_0} = 2.7 \pm 0.6$ s (black circles) and $\tau_{res,300a_0} = 0.6 \pm 0.3$ s (red circles) for a scattering length $a = 0$ and $a = 300a_0$, respectively. The cycling transition for imaging the atoms is not closed at low magnetic fields. Atoms which decay into a dark state become invisible. To correct for the effectively reduced scattering cross section of the atoms, measured atom numbers are scaled by those obtained from high field imaging.

and at zero scattering length is $\tau_{res,0a_0} = 2.7 \pm 0.6$ s. The atomic loss is mainly due to the heating processes mentioned above. Atom loss due to evaporative cooling at the s-wave scattering length $a(B=0)=0$ can be neglected.

At a magnetic field of 322G, where the s-wave scattering length $a(B)$ is approximately equal to $-300a_0$, large atom number losses are measured. The lifetime of the atomic ensemble is decreased to only $\tau_{res,-300a_0} = 0.6 \pm 0.3$ s. A reason for this increased atom loss is the evaporation of the atoms from the resonator dipole trap. Due to the diverging density of states given by the gaussian trap [108] and the atomic distribution at $140\mu K$, it can be assumed that most of the atoms populate energy levels close to the trap edge. This leads to a major atom loss, while the reduction in thermal energy of those remaining in the trap is not very large. Evaporative cooling is expected to be inefficient. As we will see in the following, this initial particle loss is an important step in the evaporation process and leads to a larger phase space density in the end.

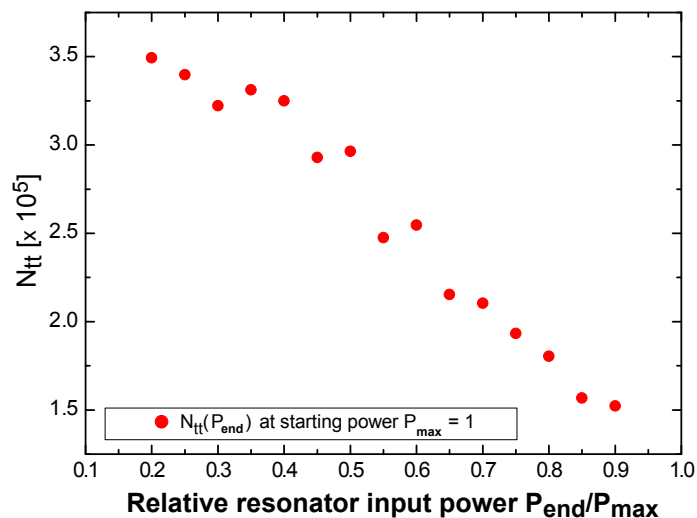


Figure 4.8: Atom number $N_{tt}(P_{end}, a = -300a_0)$ in the running wave dipole trap after evaporation to different trap depths $U_0 \sim P_{end}$. A gain in atom number N_{tt} of a factor 2.3 is achieved by evaporating to laser powers $P_{end} = 0.2P_{max}$.

4.2.3 Transfer into the running wave dipole trap

In order to efficiently transfer atoms from the standing into the running wave dipole trap, the atoms populating higher lying states of the combined potential need to be redistributed to lower lying states by evaporation. The evaporation process is controlled by the laser power that sets the resonator potential depth $U_0(t)$ and by the magnetic field that sets the scattering length a . When simultaneously lowering the trap depth and letting the atoms collide, which is called forced evaporation, lower lying states are populated and atoms are finally transferred into the running wave dipole trap. The transfer has been characterized regarding the two parameters $U_0(t)$ and a . The remaining atom number $N_{tt}(U_0, a)$ is measured after transport to the glass cell and a second evaporation step, where the power of running wave is reduced from 3.5W to 50mW.

The number $N_{tt}(U_0, a = -300a_0)$ of atoms trapped in the running wave dipole trap was measured after evaporation at a scattering length $a = -300a_0$ to different final values of the final resonator power P_{end} , which is proportional to $U_0(t = 2.7s)$. In figure 4.8, a linear increase $N(P_{end})$ is found when lowering P_{end} , which is limited by an increase of number fluctuations for $P_{end} < 0.2P_{max}$. The slope $dU_0(t)/dt$ proved to be insensitive to the final atom number.

In figure 4.9, the atom number $N_{tt}(P_{end} = 0.2P_{max}, a)$ and the corresponding temperature T in the running wave dipole trap after evaporation to $P_{end} = 0.2P_{max}$ are

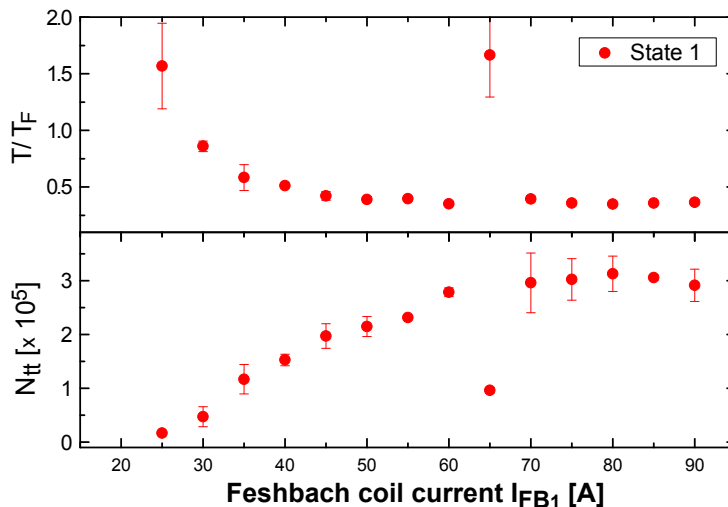


Figure 4.9: Number of atoms $N_{tt}(P_{end} = 0.2P_{max}, a)$ transferred to the running wave dipole trap. The scattering length a decreases with the current I_{FB_1} , resulting in a less efficient transfer, i.e. a reduced atom number, due to a less efficient evaporation process. Atom loss and heating at $I_{FB_1}=65\text{A}$ are attributed to inelastic losses at a p-wave scattering resonance.

shown as a function of current I_{FB_1} in the Feshbach coils, which sets the scattering length a . At $I_{FB_1} = 92\text{A}$ corresponding to approximately $-300a_0$, evaporation is most efficient: N_{tt} is largest and low temperatures are obtained ($T/T_F = 0.4$). By lowering the current, the scattering length decreases and evaporation is less efficient. The redistribution of atoms into lower lying states is hindered: the final atom number is lower as well as the final temperature higher.

Two kinds of heating processes were identified during the evaporation. One is caused by resonantly enhanced inelastic p-wave scattering, i.e. scattering into states with relative momentum $l = 1$. The other is due to inelastic collision between the two ground states and higher lying states.

In figure 4.9, evaporation at 65A leads to a small atom number and high temperatures ($T/T_F = 1.7$), although the s-wave scattering length a is still large. This heating process can be attributed to inelastic collisions caused by resonantly enhanced p-wave scattering. Usually, scattering into a final state with angular momentum $l = 1$ is suppressed, since the partial wave amplitude scales with k^{2l} . But at 214.9G (which would correspond to 61.4A at a relative magnetic field of 3.5G/A), it seems that a p-wave Feshbach resonance [117] is accessed, where identical fermions in state $|2\rangle$ inelastically scatter.

The second heating process caused by inelastic collisions between atoms in the two ground states $|1\rangle$ and $|2\rangle$, and higher lying states from the $2^2S_{1/2}, F = 3/2$ manifold

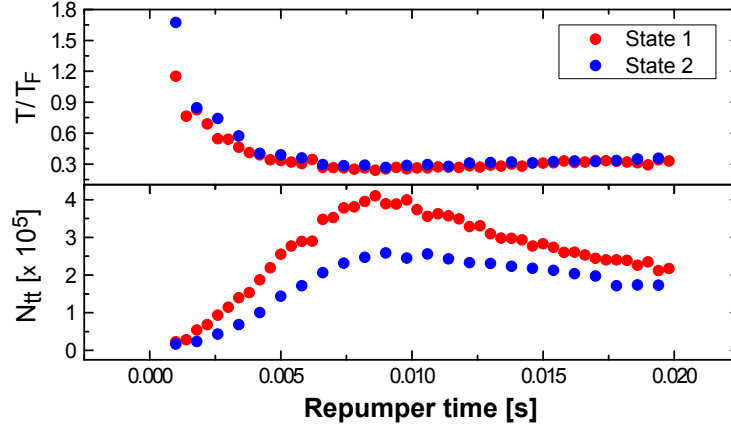


Figure 4.10: Atom number $N_{tt}(\Delta t_{repump})$ and the corresponding relative temperature T with respect to the time delay, called repumper time Δt_{repump} , between the turn off time of repumper and cooler.

is minimized by depopulating higher lying states. This is done by first turning off the repumping transition with frequency ν_{mot_1} and by only driving the cooling transition $2^2S_{1/2}, F = 3/2 \rightarrow 2^2P_{3/2}, F = 5/2$ until all atoms decay into state $2^2S_{1/2}, F = 1/2$ [62]. In figure 4.10, the final atom number and the temperature in the running wave dipole trap at 50mW is shown as a function of the time delay between the turn off time of the repumper and the cooler. If this time delay, here called the repumper time, is shorter than 8ms, heating and atom losses are observed.

4.2.4 Optical transport of the atomic ensemble

Atoms centered at the focus of transport trap are accelerated and decelerated [64] according to a smooth velocity profile, which can be programmed. During the movement of atoms centered at the focus of transport trap, too rapid acceleration and vibrations will heat the atomic ensemble, which causes a loss of atoms. Either dipole oscillations of the atomic ensemble are excited, or atoms are spilled from the trap or parametrically heated.

We could not observe any oscillation. Atom loss due to resonant scattering and to parametric heating the transport trap was measured by comparing a one way trip with a three way trip from the center of the main chamber to the glass cell. While the former is characterized by a transfer efficiency e_1 , the latter is given by $e_3 = e_1^3$. By comparing atom numbers and temperatures after evaporation to a final laser power 50mW of a one way transport with those of a three way transport, we obtain $Ne_1 = N_{tt,1} = 3.9 \cdot 10^5$ and $Ne_3 = N_{tt,3} = 2.3 \cdot 10^5$. With a corresponding transfer efficiency $e_1 = 76\%$, the

atom total atom number loss is $\Delta N_1 = 1.2 \cdot 10^5$. When applying the same method to the relative temperature with $(T/T_F)_1 = 0.23$ and $(T/T_F)_3 = 0.33$, the resulting heating rate is $\Delta(T/T_F)_1 = 0.05$ for a one way transport.

4.3 Observation of degenerate Fermi gases

In this section, density distributions of degenerate non-interacting Fermi gases, molecular Bose-Einstein condensates at different temperatures and gases with imbalanced spin population are shown.

In the center of the glass cell, fermions are evaporatively cooled in the running wave dipole trap by reducing the laser power from 2W to different values below 50mW within 3.1s. Atom numbers N and temperatures T are extracted from the column density distributions. These are measured with the conventional imaging setup in x-direction after free expansion from the trapping potential, by fitting the corresponding functions $n_{2D}(x, y)$. The trapping potential is harmonically approximated here, although fermions are trapped in a gaussian trap. At low temperatures, the fitted temperature is overestimated, because the density distribution changes from a gaussian distribution to a distribution showing the characteristic shape of the trapping potential, $n \sim (\mu - V(r))^{3/2}$. The gaussian shape in the density distribution is interpreted as the contribution from a thermal gas instead of the gaussian shape of the trap.

In order to convert the photon distribution detected on the camera to an atomic density distribution, we assume that the atomic column density is proportional to the optical density. This assumption is true if atoms are illuminated such that only a few photons per atom are scattered to avoid a reduction in the photon scattering cross section, the optical density ($OD \ll 1$) is small and the imaging light intensity is much below saturation intensity ($I \ll I_{sat}$) [118].

4.3.1 Non-interacting Fermi gas

In order to obtain non-interacting degenerate Fermi gases, atomic ensembles are evaporatively cooled in the running wave dipole trap down to different final potential depths $U_{tt,0}$ at a magnetic field of 300G, which corresponds to a scattering length $-300a_0$. After a thermalization time of approximately 160ms, the magnetic field is turned to 528G, where the scattering length is zero. The atomic ensemble is then released from the trap for 1.5ms, before it is illuminated with resonant light. In the insets of figure 4.11a, images of a degenerate Fermi gas after evaporation down to 5mW and 40mW are shown. By fitting the corresponding functions to the obtained column density distribution, the temperature is extracted, which is 194nK ($0.16T/T_F$) and 364nK ($0.23T/T_F$),

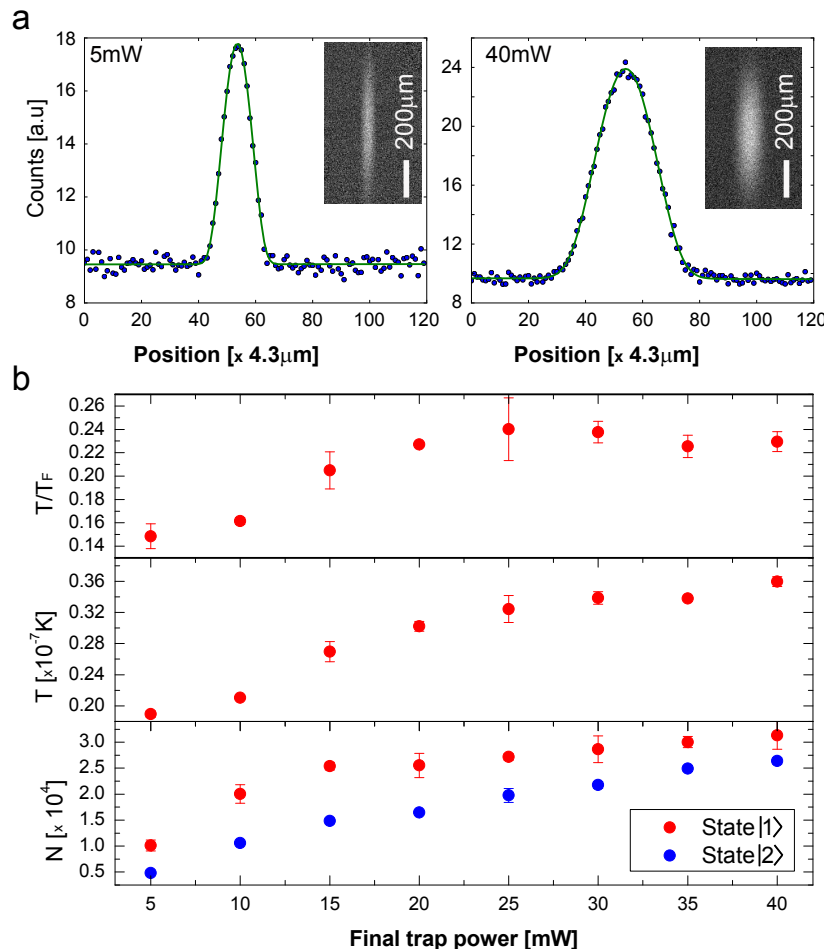


Figure 4.11: Non-interacting degenerate Fermi gas: a. Absorption images and vertically integrated column density distribution after 1.5ms expansion from a trap with a laser power of 5mW (left) and 40mW (right). From the fitted function (green line), the atom number N and the temperature T is extracted, which are shown in b.

respectively. In figure 4.11b, the atom number N as well as the absolute and relative temperature T and T/T_F are shown with respect to the final trap depth after evaporation.

If the trap depth is lowered at a magnetic field of 528G, where the scattering length a is zero, atoms are not evaporatively cooled but just spilled from the dipole trap at zero scattering length. The minimum temperature achieved is $1.6T/T_F$ and the number of atoms is approximately a factor of three smaller than after evaporation at $a = -300a_0$. Hence evaporative cooling is essential for obtaining a degenerate Fermi gas.

4.3.2 Molecular Bose-Einstein condensate

A molecular Bose-Einstein condensate is obtained by evaporative cooling close below the Feshbach resonance. There, Feshbach molecules are formed during the evaporation process, while the excess binding energy is transferred to atoms which then escape from the trap. By reducing the temperature below $0.55T/T_F$, Feshbach molecules then condense to a Bose-Einstein condensate.

In our case, atoms are evaporated at a magnetic field of 794G, which corresponds to a scattering length of $a \simeq 9100a_0$. After an expansion time of 3.5ms at a magnetic field of 776G, corresponding to a scattering length of $5900a_0$, the molecular condensate is resonantly illuminated. In figure 4.12a, the column density of a condensate measured after evaporation down to 20mW and 50mW is shown. A bimodal function is fitted to the density distribution. The fraction of atoms, which is fitted to a parabolic function (red line) represents condensed molecules, while the underlying gaussian density distribution (green line) contains thermal molecules.

The ratio between the condensed molecules N_0 and total number of molecules N , i.e. the condensate fraction, is shown in figure 4.12b with respect to the final potential depth, which is again set by laser power. The condensate fraction given in equation 2.26, is fitted to a function $N_0/N \sim c_1 - c_2 P_{tt}^3$, with fitting parameters $c_1 = 0.68$ and $c_2 = 3.35 \cdot 10^{-6} \text{mW}^{-3}$, and the laser power P_{tt} , which is proportional to the potential depth U_0 . According to this fit, the onset of Bose-Einstein condensation occurs at a laser power of 59mW.

With decreasing potential depth, the total molecule number N as well as the absolute temperature T decreases to $N = 10^5$ and a minimal detectable temperature of approximately 150nK, respectively.

4.3.3 Realization of a spin imbalanced Fermi gas

In ultra-cold atomic Fermi gases, the relative spin population between the two lowest hyperfine states can be controlled experimentally by either a radio-frequency transfer between two hyperfine spin states or by accessing a p-wave Feshbach resonance to induce inelastic losses of only one spin state.

Here, an imbalanced spin mixture was produced by accessing the $|2\rangle + |2\rangle$ p-wave Feshbach resonance at 214.9G with a width of 0.4G to remove atoms populating state $|2\rangle$. The loss in this spin component is controlled by the time remaining on resonance, which is 50ms, here. Afterwards, atoms are evaporatively cooled below the s-wave Feshbach resonance at 776G. Again after 3ms expansion at a magnetic field of 703G from the trap with a laser power of 28mW, each spin state is imaged separately (figure 4.13).

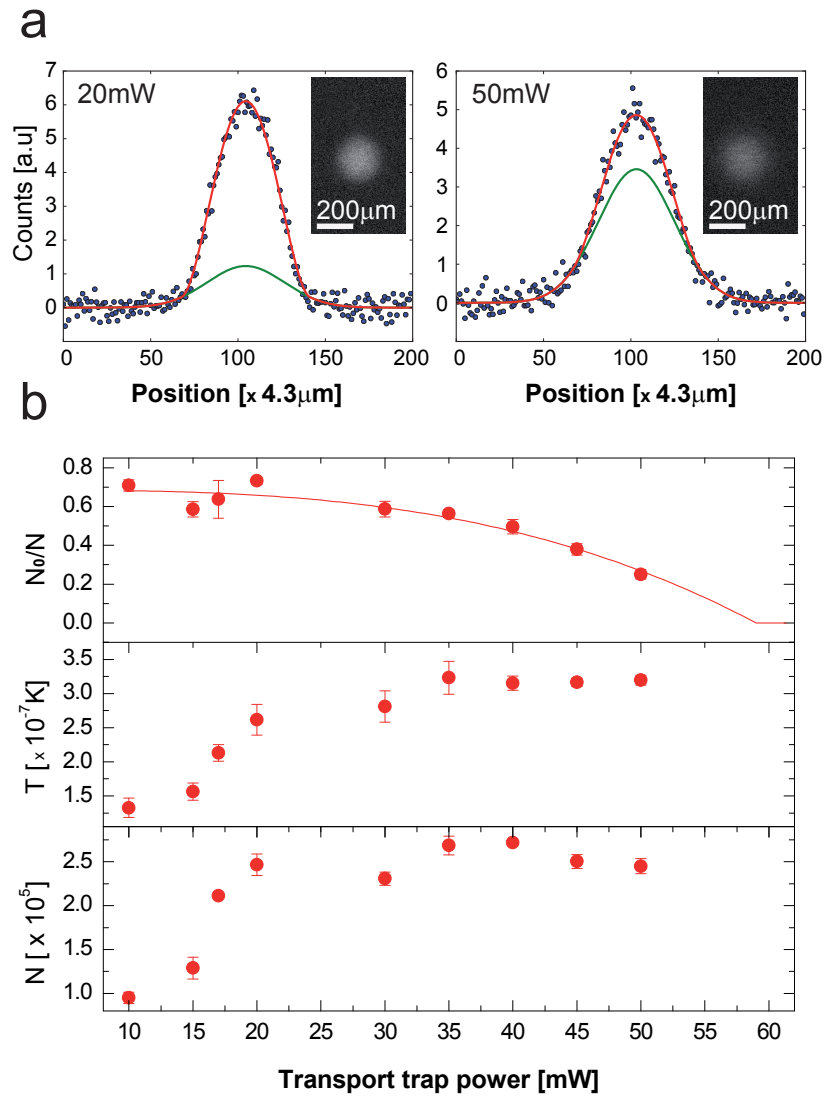


Figure 4.12: Formation of molecular Bose-Einstein condensation. a. Absorption images and vertically integrated column density distribution after a 3.5ms expansion from the trapping potential with a final laser power of 20mW and 50mW. From a bimodal fit, with a parabolic (red line) and gaussian shape (green line), the number N_0 and $N - N_0$ of condensed and non-condensed molecules is extracted. b. The total molecule number N , the absolute temperature T and the condensate fraction N_0/N with respect to the final laser power in the running wave dipole trap. From the fit (see text), the onset of condensation is expected at 59mW.

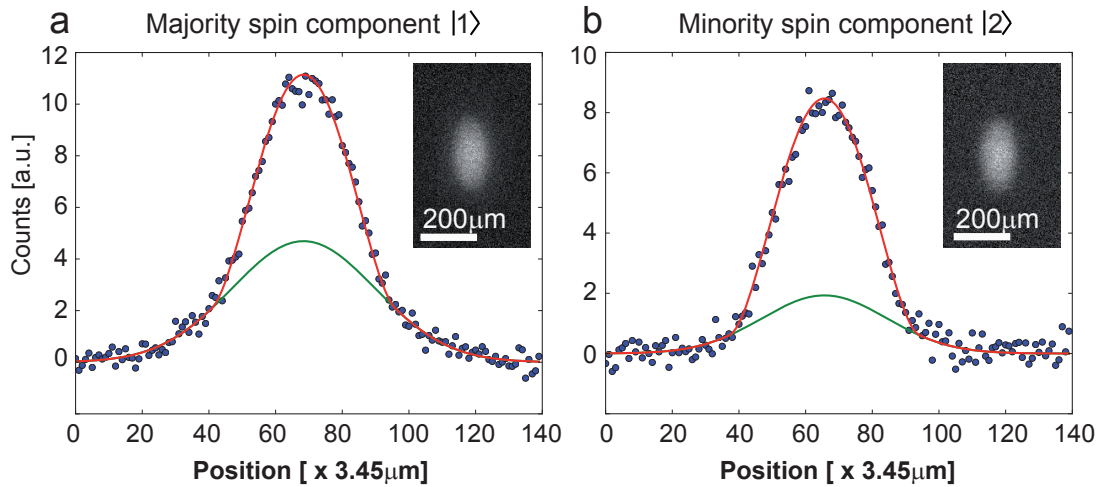


Figure 4.13: Absorption images (insets) and vertically integrated column density distribution of a two component spin mixture of state $|1\rangle$ and $|2\rangle$ with a spin population imbalance of 21%. The minority and majority spin components contain 39.5% and 60.5% of the total atom number, respectively. The temperature of the gas, obtained from the bimodal fitting function of the minority component is 377nK.

The total atom number in state $|1\rangle$ in the left picture is equal to $N_{|1\rangle} = 1.92 \cdot 10^5$, the one in state $|2\rangle$ in the right picture equals to $N_{|2\rangle} = 1.25 \cdot 10^5$. The former is called the majority spin component, while the latter is called the minority spin component. Here, the spin imbalance, which is defined as $(N_{|1\rangle} - N_{|2\rangle}) / (N_{|1\rangle} + N_{|2\rangle})$ is 0.21. By fitting a bimodal function to the density distribution of each spin component, we obtain a condensate fraction of 43% and 68% for the majority and minority components, respectively. This corresponds to a condensed molecule number of $N_0 = 8.5 \cdot 10^4$ in both cases.

In other work [33, 34, 35, 119], it could actually be shown, that the equal number in the condensed phase is no coincidence, but really due to a phase separation between the molecular Bose-Einstein condensate and the spin polarized Fermi gas consisting of excess atoms in the majority components located in the wings of the profile.

4.4 Microscopy of a Fermi gas

The whole experimental setup was designed to finally obtain high resolution images of trapped Fermi gases. This imaging system allows us to detect the atomic density distribution with a resolution of 700nm, of which some example are presented in this section. For comparison, an absorption image of a trapped non-interacting Fermi

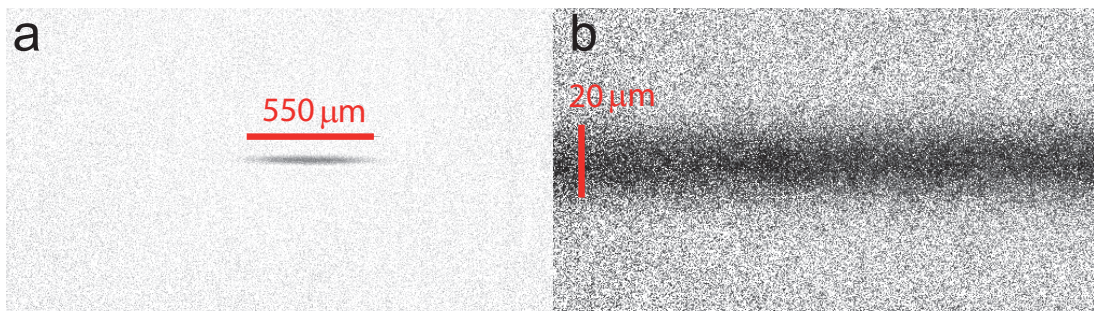


Figure 4.14: Comparison between conventional and high resolution imaging. a. The axial extension the trapped atomic ensemble absorption-imaged with the conventional imaging setup along x-direction is approximately $550\mu m$. b. The same ensemble is detected with the high resolution imaging along the z-direction. The dimension of the image is $152\mu m \times 84\mu m$. Approximately a quarter of the atomic ensemble is shown here.

gas below Fermi temperature obtained with the conventional and the high resolution imaging are shown in figure 4.14.

With a different imaging technique, the phase contrast imaging [120], differences in the population, $N_{\uparrow} - N_{\downarrow}$, of a two-component spin mixture can be measured locally. Off-resonant light passing through an atomic ensemble experiences a detectable phase shift. For an equal spin population at a certain frequency de-tuning, the phase shift caused by the one spin state is negative with respect to that of the other. The phase shift cancels and the atomic ensemble becomes transparent. If the spin population is not equal in certain domains of the trapped atomic ensemble, there is a phase shift which turns the direction of the linearly polarized light. With a polarizing beam splitting cube, a change in polarization is converted into an intensity signal. If these domains are larger than the imaging resolution, a local fluctuation in the spin population corresponding to an intensity fluctuation appears on the detector (figure 4.15).

The last example is a fluorescence image of approximately $N = 10^3$ spin-polarized fermions trapped in a micro potential, which is created by focussing red de-tuned laser light (767nm) by means of the upper microscope objective (inset of figure 4.16). Here, the optical resolution has been artificially reduced by a diaphragm to obtain a beam waist $\omega_0 = 2.4\mu m$ and a Rayleigh length of $z_R = 13.2\mu m$. With the measured waist, the Rayleigh length and the given laser power, trapping frequencies are $\nu_r = 58\text{kHz}$ and $\nu_{ax} = 4.1\text{kHz}$ in radial and axial directions, respectively (photon recoil frequency = 73.7kHz). The corresponding Fermi energy is approximately 240kHz .

The fluorescence image shown in figure 4.16 was taken by illuminating the trapped atomic ensemble with $2.5\Gamma = 15\text{MHz}$ blue de-tuned light at an intensity $I \gg I_{sat}$ for

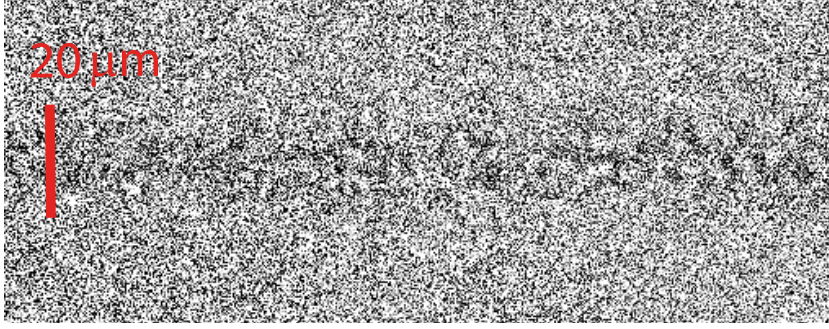


Figure 4.15: Phase-contrast image of a trapped non-interacting degenerate fermionic ensemble located at the $20\mu\text{m}$ wide horizontal bar. The cloud is transparent unless there are local differences in the spin population, which appear here as coarsely grained fluctuations in intensity.

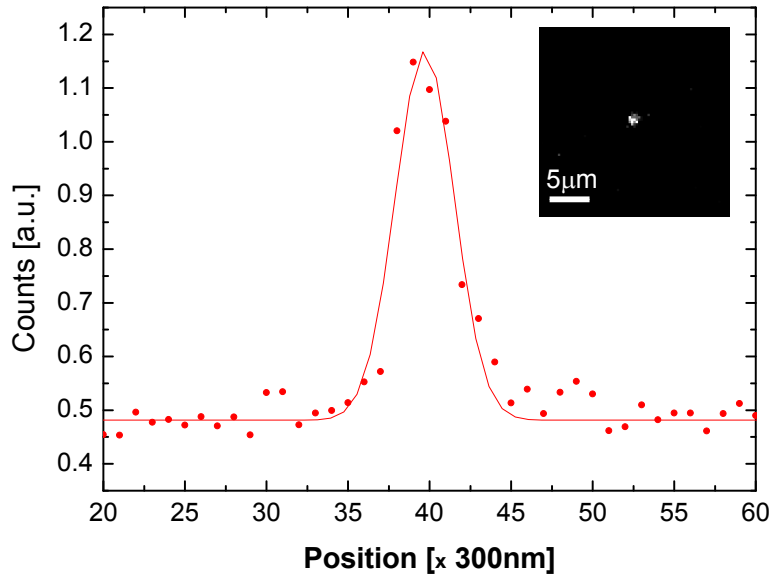


Figure 4.16: Fluorescence image an atomic ensemble (inset) and the detected photon distribution. The atoms is trapped in a micro dipole potential create by a focussed laser beam with a waist $\omega_0 = 2.4\mu\text{m}$ and a Rayleigh length $z_0 = 13.2\mu\text{m}$. The fitted diameter of the photon distribution is $d_r = 2.2\mu\text{m}$.

$4\mu\text{s}$. The fluorescence signal was detected on the EMCCD camera by collecting photons at the resonance wave-length (671nm) with the lower microscope and filtering out far off-resonant light. By fitting a gaussian function to the detected photon distribution, a maximum cloud diameter of $d_r = 2.2\mu\text{m}$ is obtained.

With simple estimates one can obtain a rough idea about the atomic ensemble under

investigation. By assuming an axial extension of $d_{ax} = d_r \nu_r / \nu_{ax}$, we obtain an approximate volume $V = d_r^2 d_{ax} = 154 \mu\text{m}^3$, a density of $6.5 \cdot 10^{12} \text{cm}^{-3}$ and an optical density $N\sigma_0/d_r^2 = 45 < \text{OD}$. It can be assumed that the actual volume in which the atoms are confined is smaller. At these high density, imaging is not yet understood because the response of the atomic ensemble changes and the deduction of the atoms number in trap from photon distribution is difficult.

5 Local observation of antibunching in a trapped Fermi gas

This chapter has been submitted to the Physical Review Letters and is published on the preprint server, arXiv:1005.0302v1 [121].

A finite-size system in thermodynamic equilibrium with its surrounding shows characteristic fluctuations, which carry important information about the correlation properties of the system. In a classical gas, fluctuations of the number of atoms contained in a small sub-volume yield a Poisson distribution, reflecting the uncorrelated nature of the gas. An intriguing situation arises when the thermal de Broglie wavelength approaches the interparticle separation and the specific quantum statistics of the constituent particles becomes detectable. For bosons, positive density correlations build-up, until Bose-Einstein condensation occurs, as measured in Hanbury Brown-Twiss (HBT) experiments [122, 123, 124, 125, 126, 127, 128]. The effect of bunching also manifests itself in enhanced density fluctuations in real space [129]. In contrast, fermions obey the Pauli principle. This gives rise to anti-correlations, which have been observed in HBT experiments [130, 131, 132, 133, 134], and are expected to squeeze density fluctuations below the classical shot noise limit. Moreover, for trapped fermions, the anti-correlations vary in space, reaching a maximum in the dense center of the cloud, which should be accessible to a local measurement.

In this letter we report on high-resolution in-situ measurements of density fluctuations in an ultracold Fermi gas of weakly interacting ${}^6\text{Li}$ atoms. We extract the mean and the variance of the density profile from a number of absorption images recorded under the same experimental conditions. Our measurements show that the density fluctuations in the center of the trap are suppressed for a quantum degenerate gas as compared to a non-degenerate gas. We analyze our data using the fluctuation-dissipation theorem, which relates the density fluctuations of the gas to its isothermal compressibility. This allows us to extract the temperature of the system [65].

We first describe the experimental procedure to obtain a quantum degenerate gas of about 6×10^4 ${}^6\text{Li}$ atoms equally populating the two lowest hyperfine states. Following

the method described in [17], the atoms are loaded into an optical dipole trap created by a far off-resonant laser with a wavelength of 1064 nm, focused to a $1/e^2$ -radius of $(22 \pm 1) \mu\text{m}$ (unless otherwise stated, errors are a combination of statistical errors and uncertainties in the determination of experimental parameters). The cloud is then optically moved [64] into a glass cell that provides high optical access, see Fig. 5.1(a). In the glass cell, forced evaporation is performed by reducing the trap power from initially 2 W to 4.7 mW. During evaporation a homogeneous magnetic field of 300 G is applied to set the s-wave scattering length a for inter-state collisions to $-300 a_0$, where a_0 is the Bohr radius. The magnetic field is then ramped to 475 G in 150 ms, changing a to $-100 a_0$, and finally the power of the trapping beam is increased to 10 mW in 100 ms. Alternatively, we prepare the lithium gas at temperatures above quantum degeneracy. For this, we evaporate to 50 mW before recompressing to 100 mW, followed by a 100 ms period of parametric heating. In both cases, the cloud is allowed to thermalize for 350 ms before an absorption image is taken.

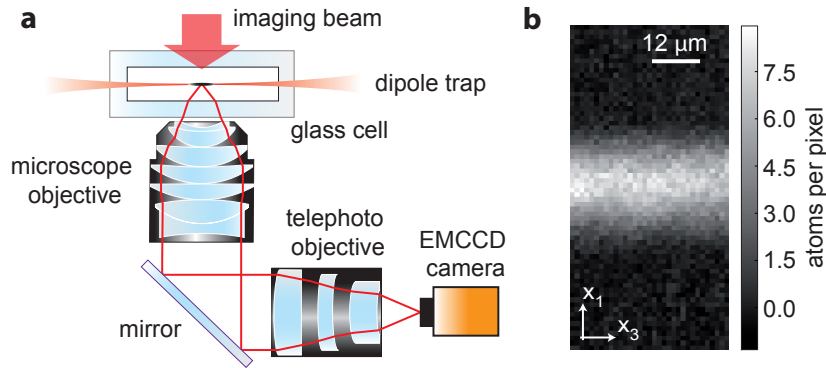


Figure 5.1: (a) Setup for high-resolution imaging of the trapped ${}^6\text{Li}$ gas. The shadow cast by the atoms held in the dipole trap is imaged through the microscope objective and a telephoto objective onto an EMCCD chip. The resolution ($1/e^2$ -radius) is $1.8 \mu\text{m}$ at a wavelength of 671 nm and the magnification is 54 (the resolution of the $\text{NA}=0.55$ microscope objective has been artificially reduced with a diaphragm in order to increase the depth of field to the order of the cloud size). (b) Density distribution (atoms per pixel) of the trapped atoms obtained by averaging over 20 realizations. The effective pixel size measures $1.2 \mu\text{m}$ (The size of a camera pixel corresponds to 300 nm in the object plane. We do 4×4 software binning, yielding an effective pixel size of $1.2 \mu\text{m}$. The image is $\sim 40 \mu\text{m}$ wide and shows about one tenth of the cloud).

Our imaging setup is sketched in Fig. 5.1(a). The probe light, resonant with the lowest hyperfine state of the $|2S_{1/2}\rangle$ to $|2P_{3/2}\rangle$ transition, is collected by a high-resolution microscope objective and imaged on an electron-multiplying CCD (EMCCD) chip. The atoms are illuminated for $8 \mu\text{s}$, each atom scattering about 20 photons on average. Fig. 5.1(b) shows the average density distribution obtained in 20 experiments.

We now present our procedure for extracting the spatially resolved variance of the atomic density. The position of each pixel in the imaging plane of the camera defines a line of sight intersecting with the atomic cloud. Correspondingly, each pixel, having an effective area A , determines an observation volume in the atomic cloud along this line of sight. At low saturation, the transmission t of the probe light through an observation volume containing N atoms reads $t = e^{-\sigma \cdot N/A}$, where σ is the photon absorption cross section. As a consequence, for small Gaussian fluctuations of the atom number, the *relative* fluctuations of the transmission coefficient are equal to the *absolute* fluctuations of the optical density and are thus directly proportional to the number fluctuations:

$$\frac{\delta t^2}{\langle t \rangle^2} = \frac{\sigma^2}{A^2} \delta N^2, \quad (5.1)$$

where δt^2 , $\langle t \rangle$ and δN^2 are the variance and the mean of the transmission coefficient, and the variance of atom number, respectively.

Experimentally, repeated measurements of identically prepared clouds provide us with a set of count numbers C for each pixel, i.e. each observation volume, corresponding to a certain number of incoming photons registered by the EMCCD. We then compute the variance δC^2 and mean $\langle C \rangle$. The relative noise of the counts and the relative noise of the transmission are related by:

$$\frac{\delta C^2}{\langle C \rangle^2} = \frac{2g}{\langle C \rangle} + \frac{\delta t^2}{\langle t \rangle^2}. \quad (5.2)$$

Here, g is the gain of the camera for converting photoelectrons to counts. The first term is the contribution of photon shot noise while the second term is the contribution of atomic noise. The factor 2 in the photon shot noise term has its origin in excess noise caused by the electron-multiplying register [135, 136]. We extract the contribution of the atoms to the relative fluctuations of the counts, by subtracting photon shot noise on each pixel according to (5.2). This requires the value of g which we determine from the linear relationship between the variance and the mean of the number of counts in a set of repeated measurements. The atom number fluctuations are subsequently obtained from (5.1).

In order to reduce technical noise adding to these fluctuations, we reject images showing the largest deviations of total atom number or cloud position (images deviating more than 1.5 standard deviations in the mean position and more than 1.0 standard deviations in the total atom number are excluded), which amounts to excluding about 30% of the images. The remaining shot-to-shot fluctuations of the total atom number δN_{tot}^2 are taken into account by further subtracting the quantity $\delta N_{\text{tot}}^2 / N_{\text{tot}}^2 \langle N \rangle^2$ ($< 2\%$ of N), which is essentially a rescaling of the data using the mean density profile [129]. Applying this algorithm to each pixel of the images yields a local measurement of the variance of the atom number. This process neither requires knowledge about

the quantum efficiency of the camera nor a calculation of the absolute value of the transmission coefficient for each shot and pixel. We thus avoid extra noise related to the division operation by a reference picture.

As in standard absorption imaging, the mean atom number per pixel is calculated by dividing the mean transmission profile by the mean of reference images taken without atoms after each shot. The values for variance and mean, obtained by applying the above procedures, are then averaged along equipotential lines of the trap. These lines deviate from horizontal lines (x_3 -axis) in our images by less than half a pixel ($0.6 \mu\text{m}$).

Fig. 5.2 shows the observed variance of the atom number plotted against the mean atom number detected on a pixel. One set of data was taken for a gas at temperatures above quantum degeneracy (red squares) and another set of data for a quantum degenerate gas (blue circles). Above quantum degeneracy, the observed variance is found to be proportional to the mean number of atoms. This linear behavior gives us confidence in our data processing procedure and confirms that the fluctuations originate from atomic shot noise.

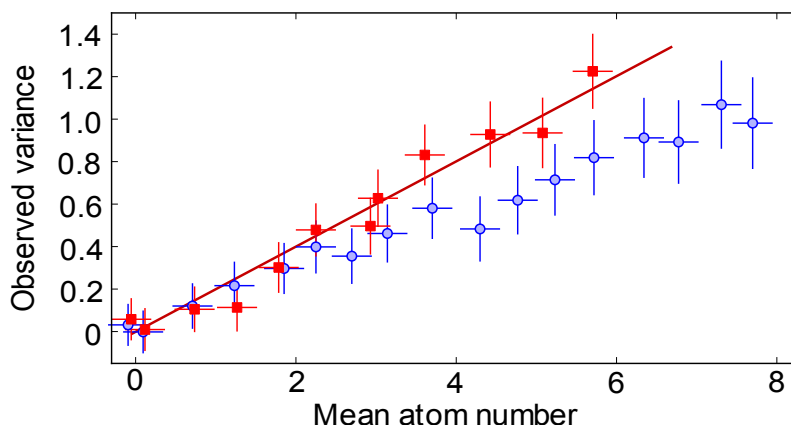


Figure 5.2: Observed variance versus mean of the atom number detected on a pixel. Red squares show the data for a non-degenerate and blue circles for a quantum degenerate gas. The solid red line is a linear fit to the non-degenerate gas, yielding a slope of 0.20 ± 0.02 . For the data shown, 80 experiments were performed, 60 for the degenerate case and 20 for the non-degenerate case. The error bars shown are estimated from the subtraction of photon shot noise which is the dominant contribution.

In order to quantitatively understand the slope of the noise curve, which is fitted to be 0.20 ± 0.02 , two main effects have to be considered. These reduce the observed variance and explain the deviation from a slope of one, which would be expected for the full shot noise. First, the effective size of the pixel is of the order of the resolution of the imaging system. As a consequence, the observed noise is the result of a blurring of the

signal over the neighboring pixels. This effect is also observed in [129, 67], and explains a reduction factor of 0.22 (by binning pixels over a 4x4 region, the observed slope is increased up to 0.8, at the cost of a strong decrease of the signal to noise ratio). Second, the probe light intensity used for the detection is $(15 \pm 1)\%$ of the saturation intensity. This leads to a reduction of the photon absorption cross section due to saturation by 0.95 and due to the Doppler-shift by about 0.9. Together, these effects lead us to expect a slope of about 0.19, in good agreement with the observations.

We now turn to the data taken for the quantum degenerate gas (blue circles in Fig. 5.2). At low densities, the variance is again found to be proportional to the mean density. For increasingly higher densities, we observe a departure from the linear behavior and the density fluctuations are reduced compared to the shot noise limit seen for the non-degenerate gas. This is a direct consequence of the Pauli principle which determines the properties of a quantum degenerate Fermi gas. One can think of the Pauli principle as giving rise to an interatomic "repulsion" [137], which increases the energy cost for large density fluctuations. This is similar to the case of bosonic systems with strong interparticle interactions, where observations have shown a reduction of density fluctuations [129] and squeezing of the fluctuations below the shot noise limit [67, 42].

In contrast to previous measurements on antibunching [133, 134], we have measured density fluctuations in a spatially resolved way. For the construction of Fig. 5.2, we have averaged the observed variance for regions of equal mean density, whereas Fig. 5.3 shows the variance (blue circles) and the mean (black line) of the atom number as a function of the radial position in the trap for a quantum degenerate gas. While the variance is proportional to the mean in the wings, at low density, we observe a reduction of the variance by about 2 dB close to the center, at higher density. The inset shows data for a non-degenerate gas; in both cases the variance has been rescaled using the slope fitted in Fig. 5.2. The reduction of fluctuations is a direct indication of the level of quantum degeneracy of the gas. The larger the average occupation of a single quantum state, the more the effect of the Pauli principle becomes important and fluctuations are consequently suppressed. Fig. 5.3 thus represents a direct measurement of the local quantum degeneracy, which is larger in the center of the cloud than in the wings.

In order to understand this quantitatively, we describe the atoms contained in an observation volume in terms of the grand-canonical ensemble with a local chemical potential fixed by assuming local density approximation. For a non-interacting gas, the ratio of mean atom number and its variance is determined by the fugacity z of the system. This leads to the equation

$$\frac{\delta N^2}{\langle N \rangle} = \frac{\int \text{Li}_{1/2}(-z(x_1, x_2)) dx_2}{\int \text{Li}_{3/2}(-z(x_1, x_2)) dx_2}, \quad (5.3)$$

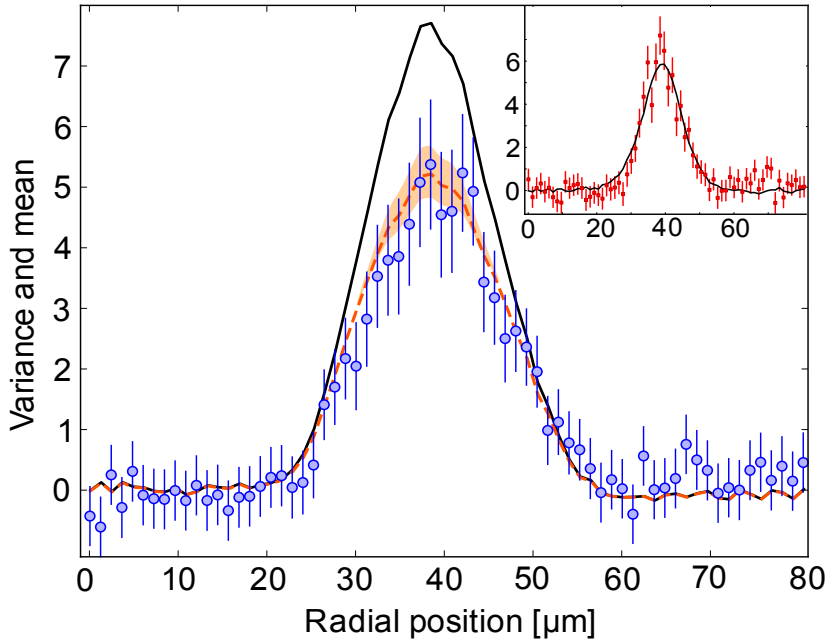


Figure 5.3: Spatially resolved measurement of antibunching. The black line shows the mean atom number and the blue circles the corresponding variance along the x_1 -axis for a degenerate gas. The variance is rescaled using the slope fitted in Fig. 5.2. Error bars are estimated from the subtraction of photon shot noise, which is the dominant contribution. The dashed line shows the variance derived from theory. The shaded region indicates the uncertainty originating from uncertainties in the trap parameters. The inset shows corresponding data for a non-degenerate gas.

where Li_i is the i -th polylogarithmic function, x_1 and x_2 are radial coordinates of the cloud and line-of-sight integration is performed along the x_2 -axis.

The dashed line in Fig. 5.3 is computed using (5.3). For the computation we make use of the Gaussian shape of the trap, the central fugacity of 13_{-4}^{+18} , obtained in an independent time-of-flight experiment (see below), and the experimental density profile. The agreement between theory and experiment also confirms our assumption of negligible interactions as well as the description in terms of the grand-canonical ensemble (the Fermi wavelength is of the order of the pixel size. However, column integration is expected to average out possible correlations).

We now focus on the interpretation of our results using the fluctuation-dissipation theorem. At thermal equilibrium, density fluctuations are universally linked to the thermodynamic properties of the gas through the fluctuation-dissipation theorem, which can be expressed as:

$$k_B T \frac{\partial \langle N \rangle}{\partial \mu} = \delta N^2 \quad (5.4)$$

where T is the temperature of the gas, μ the chemical potential and k_B the Boltzmann constant. Since the local density approximation allows one to assign a local chemical potential to any position in the trap, it is possible to determine the compressibility $\frac{\partial \langle N \rangle}{\partial \mu}$ directly from the mean density profiles [67]. From (5.4), the ratio of this quantity to the measured variance profile of the cloud provides a universal temperature measurement [65].

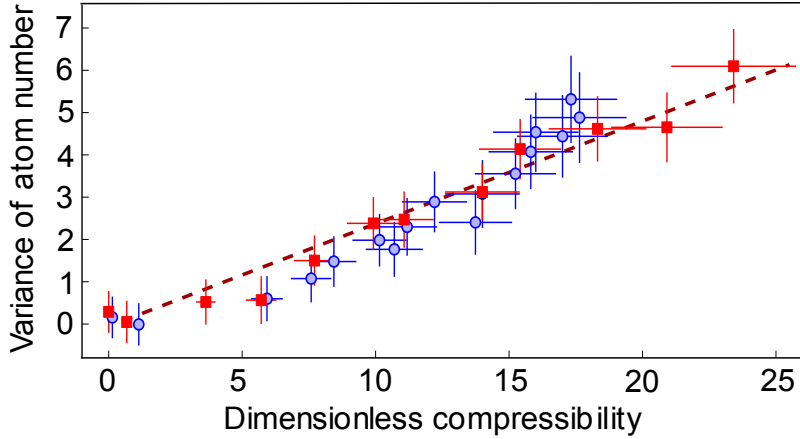


Figure 5.4: Fluctuation-based temperature measurement. Variance of atom number detected on an effective pixel versus dimensionless compressibility. The blue circles and red squares show the data for the quantum degenerate and the non-degenerate case, respectively. The slope gives a measure of the temperature in units of the trap depth, according to (5.4). The dashed red line is fitted to the red squares.

We apply this procedure to our data by computing the compressibility, $\frac{\partial \langle N \rangle}{\partial \mu} = \frac{\partial \langle N \rangle}{\partial x} \left(\frac{\partial \mu}{\partial x} \right)^{-1}$, where we take the Gaussian shape of the optical dipole trap into account. To avoid the problems of numerically differentiating experimental data, we fit the mean density profile with a linear combination of the first six even Hermite functions and use the fitted curve as a measure of the density profile in (5.4). Fig. 5.4 shows the variance of atom number plotted against the dimensionless compressibility $U_0 \frac{\partial \langle N \rangle}{\partial \mu}$, where U_0 is the trap depth. We observe the linear relation described by (5.4) with a slope of $\frac{k_B T}{U_0} = 0.27 \pm 0.04$ for both data sets, the degenerate and the non-degenerate. From the physics of evaporative cooling it is expected that both slopes are the same [138]. Using trap depths derived from the measured laser powers, we obtain temperatures of (145 ± 31) nK and (1.10 ± 0.06) μ K for the quantum degenerate and the non-degenerate gas, respectively.

To assess the quality of this measurement, we have also performed time-of-flight measurements with clouds prepared under the same conditions. In this method, we determine the temperatures by fitting the measured density profiles after free expansion of 1.5 ms (1 ms for the non-degenerate gas) to the calculated shape of a non-interacting gas released from a Gaussian trap. This procedure gives us slightly higher temperatures for the degenerate and the non-degenerate clouds, which are (205 ± 30) nK ($T/T_F = 0.34 \pm 0.1$) and (1.6 ± 0.2) μ K ($T/T_F = 1.9 \pm 0.1$), respectively. We attribute the discrepancy between the two temperature measurements to deviations of the trapping beam from a Gaussian shape and residual experimental fluctuations from shot to shot, which both affect the two methods.

In conclusion, we have measured density fluctuations in a trapped Fermi gas locally, observing antibunching in a degenerate gas. In addition, we have determined the temperature of the system by comparing the fluctuations with the predictions of the fluctuation-dissipation theorem (for other fluctuation-based temperature measurements see [139, 93]). In contrast to bosons, fermions cannot exhibit first-order long range coherence due to the Pauli principle. However, when a Fermi system enters a quantum correlated phase, e.g. a superfluid phase, long range even-order correlations build up [93]. The spatially resolved measurement of density fluctuations, probing second-order correlations, is thus a natural tool to study strongly correlated Fermi gases.

6 Outlook

The ability to locally measure density fluctuations of a trapped non-interacting gas of fermionic lithium below the Fermi temperature naturally leads to an intriguing question: how will the fluctuations change in the presence of interactions?

Since pairing between fermions of opposite spin occurs in the BEC-BCS crossover regime, the quantum statistics are expected to change qualitatively: in case of weakly bound pairs, it is reasonable to assume that the fermionic nature revealed by reduced number fluctuations $\delta N(r)$ dominates. For tightly bound thermal molecules, enhanced fluctuations are expected.

When investigating pairing between fermions of opposite spin in the BEC-BEC crossover regime, it should be possible to observe a qualitative change in quantum statistics by measuring local fluctuations in the spin imbalance [140], $\delta(N_{\uparrow} - N_{\downarrow})(r)$. For example in a non-interacting Fermi gas, spin imbalance and number fluctuation should be proportional, because the atoms in each spin state can be regarded as two independent systems. The situation is different for fermionic pairs: local spin fluctuations are expected to decrease with respect to those of the non-interacting Fermi gas because the energy to break a pair and form a domain of unequal spin population increases.

The detection of number fluctuations of a trapped fermionic ensemble is experimentally challenging because small deviations from the mean density profile have to be measured. With the applied absorption imaging technique, the atoms are illuminated with resonant light at intensities $I \ll I_{sat}$ for a sufficiently short time to avoid a reduction of the photon scattering cross section occurring after multiple photon scattering. Due to the relatively high optical density of the trapped fermionic ensemble, only a small photon number is detected, leading to a large photon shot noise, which limits the signal to noise ratio.

From an implementation point of view, there is the opportunity of measuring spin imbalance with significantly reduced photon shot noise: phase contrast imaging [120] can be employed, a technique to determine local differences in the spin population directly without subtracting a large mean value. The feasibility of this approach has been shown in section 4.4. Because the fermionic ensemble is illuminated with off-resonant light,

and thereby the photon scattering cross section reduced, both the intensity and time of illumination can be increased to minimize photon shot noise.

With the experimental approach presented in this thesis, the pairing mechanism of fermionic lithium in the BEC-BCS crossover regime can now be explored by measuring local spin fluctuations with the high resolution phase contrast imaging technique.

Bibliography

- [1] S. Bose. *Z. Phys* **26**, 178 (1924).
- [2] A. Einstein. *Sitzungsberichte der Preussischen Akademie der Wissenschaften, Physikalisch-mathematische Klasse* p. 261 (1924).
- [3] A. Einstein. *Sitzungsberichte der Preussischen Akademie der Wissenschaften, Physikalisch-mathematische Klasse* p. 3 (1925).
- [4] W. Pauli. ‘The Connection Between Spin and Statistics’. *Phys. Rev.* **58**(8), 716–(1940).
- [5] B. DeMarco and D. S. Jin. ‘Onset of Fermi Degeneracy in a Trapped Atomic Gas’. *Science* **285**, 1703 (1999).
- [6] A. G. Truscott, K. E. Strecker, W. I. McAlexander, G. B. Partridge, and R. G. Hulet. ‘Observation of Fermi Pressure in a Gas of Trapped Atoms’. *Science* **291**, 2570 (2001).
- [7] F. Schreck, L. Khaykovich, K. L. Corwin, G. Ferrari, T. Bourdel, J. Cubizolles, and C. Salomon. ‘Quasipure Bose-Einstein Condensate Immersed in a Fermi Sea’. *Phys. Rev. Lett.* **87**(8), 080403– (2001).
- [8] J. Bardeen, L. N. Cooper, and J. R. Schrieffer. ‘Theory of Superconductivity’. *Phys. Rev.* **108**, 1175 (1957).
- [9] J. Bardeen, L. N. Cooper, and J. R. Schrieffer. ‘Microscopic Theory of Superconductivity’. *Phys. Rev.* **106**, 162 (1957).
- [10] M. H. Anderson, J. R. Ensher, M. R. Matthews, C. E. Wieman, and E. A. Cornell. ‘Observation of Bose-Einstein Condensation in a Dilute Atomic Vapor’. *Science* **269**, 198 (1995).
- [11] K. B. Davis, M. O. Mewes, M. R. Andrews, N. J. van Druten, D. S. Durfee, D. M. Kurn, and W. Ketterle. ‘Bose-Einstein Condensation in a Gas of Sodium Atoms’. *Phys. Rev. Lett.* **75**, 3969 (1995).

- [12] C. C. Bradley, C. A. Sackett, J. J. Tollett, and R. G. Hulet. ‘Evidence of Bose-Einstein Condensation in an Atomic Gas with Attractive Interactions’. *Phys. Rev. Lett.* **75**, 1687 (1995).
- [13] C. C. Bradley, C. A. Sackett, J. J. Tollett, and R. G. Hulet. ‘Erratum: Evidence of Bose-Einstein Condensation in an Atomic Gas with Attractive Interactions [Phys. Rev. Lett. 75, 1687 (1995)]’. *Phys. Rev. Lett.* **79**, 1170 (1997).
- [14] H. J. Metcalf and P. van der Straten. *Laser Cooling and Trapping* (Springer-Verlag, New York, 1999).
- [15] S. Inouye, M. R. Andrews, J. Stenger, H.-J. Miesner, D. M. Stamper-Kurn, and W. Ketterle. ‘Observation of a Feshbach resonance in a Bose-Einstein condensate’. *Nature* **392**, 151 (1998).
- [16] K. M. O’Hara, S. L. Hemmer, M. E. Gehm, S. R. Granade, and J. E. Thomas. ‘Observation of a Strongly Interacting Degenerate Fermi Gas of Atoms’. *Science* **298**, 2179 (2002).
- [17] S. Jochim, M. Bartenstein, A. Altmeyer, G. Hendl, S. Riedl, C. Chin, J. Hecker Denschlag, and R. Grimm. ‘Bose-Einstein Condensation of Molecules’. *Science* **302**(5653), 2101–2103 (2003).
- [18] M. Greiner, C. A. Regal, and D. S. Jin. ‘Emergence of a molecular Bose-Einstein condensate from a Fermi gas’. *Nature* **426**, 537 (2003).
- [19] M. W. Zwierlein, C. A. Stan, C. H. Schunck, S. M. F. Raupach, S. Gupta, Z. Hadzibabic, and W. Ketterle. ‘Observation of Bose-Einstein Condensation of Molecules’. *Phys. Rev. Lett.* **91**, 250401 (2003).
- [20] C. Chin, M. Bartenstein, A. Altmeyer, S. Riedl, S. Jochim, J. H. Denschlag, and R. Grimm. ‘Observation of the Pairing Gap in a Strongly Interacting Fermi Gas’. *Science* **305**(5687), 1128–1130 (2004).
- [21] J. T. Stewart, J. P. Gaebler, and D. S. Jin. ‘Using photoemission spectroscopy to probe a strongly interacting Fermi gas’. *Nature* **454**(7205), 744–747 (2008).
- [22] C. H. Schunck, Y.-i. Shin, A. Schirotzek, and W. Ketterle. ‘Determination of the fermion pair size in a resonantly interacting superfluid’. *Nature* **454**(7205), 739–743 (2008).
- [23] M. W. Zwierlein, J. R. Abo-Shaeer, A. Schirotzek, C. H. Schunck, and W. Ketterle. ‘Vortices and superfluidity in a strongly interacting Fermi gas’. *Nature* **435**, 1047 (2005).

-
- [24] C. A. Regal, M. Greiner, and D. S. Jin. ‘Observation of Resonance Condensation of Fermionic Atom Pairs’. *Phys. Rev. Lett.* **92**, 040403 (2004).
- [25] G. B. Partridge, K. E. Strecker, R. I. Kamar, M. W. Jack, and R. G. Hulet. ‘Molecular Probe of Pairing in the BEC-BCS Crossover’. *Phys. Rev. Lett.* **95**, 020404 (2005).
- [26] M. W. Zwierlein, C. A. Stan, C. H. Schunck, S. M. F. Raupach, A. J. Kerman, and W. Ketterle. ‘Condensation of Pairs of Fermionic Atoms near a Feshbach Resonance’. *Phys. Rev. Lett.* **92**, 120403 (2004).
- [27] T. Bourdel, L. Khaykovich, J. Cubizolles, J. Zhang, F. Chevy, M. Teichmann, L. Tarruell, S. J. J. M. F. Kokkelmans, and C. Salomon. ‘Experimental Study of the BEC-BCS Crossover Region in Lithium 6’. *Phys. Rev. Lett.* **93**, 050401 (2004).
- [28] M. Bartenstein, A. Altmeyer, S. Riedl, S. Jochim, C. Chin, J. H. Denschlag, and R. Grimm. ‘Crossover from a molecular Bose-Einstein condensate to a degenerate Fermi gas’. *Phys. Rev. Lett.* **92**, 120401 (2004).
- [29] J. Kinast, S. L. Hemmer, M. E. Gehm, A. Turlapov, and J. E. Thomas. ‘Evidence for Superfluidity in a Resonantly Interacting Fermi Gas’. *Phys. Rev. Lett.* **92**, 150402 (2004).
- [30] D. M. Eagles. ‘Possible Pairing without Superconductivity at Low Carrier Concentrations in Bulk and Thin-Film Superconducting Semiconductors’. *Phys. Rev.* **186**, 456 (1969).
- [31] A. J. Leggett. *Modern Trends in the Theory of Condensed Matter* (Springer-Verlag, Berlin, 1980).
- [32] P. Nozières and S. Schmitt-Rink. ‘Bose condensation in an attractive fermion gas: From weak to strong coupling superconductivity’. *J. Low Temp. Phys.* **59**, 195 (1985).
- [33] M. W. Zwierlein, A. Schirotzek, C. H. Schunck, and W. Ketterle. ‘Fermionic Superfluidity with Imbalanced Spin Populations’. *Science* **311**(5760), 492–496 (2006).
- [34] G. B. Partridge, W. Li, R. I. Kamar, Y.-a. Liao, and R. G. Hulet. ‘Pairing and Phase Separation in a Polarized Fermi Gas’. *Science* **311**(5760), 503–505 (2006).
- [35] Y.-i. Shin, C. H. Schunck, A. Schirotzek, and W. Ketterle. ‘Phase diagram of a two-component Fermi gas with resonant interactions’. *Nature* **451**(7179), 689–693 (2008).

- [36] S. Nascimbène, N. Navon, K. J. Jiang, F. Chevy, and C. Salomon. ‘Exploring the thermodynamics of a universal Fermi gas’. *Nature* **463**(7284), 1057–1060 (2010).
- [37] N. Navon, S. Nascimbene, F. Chevy, and C. Salomon. ‘The Equation of State of a Low-Temperature Fermi Gas with Tunable Interactions’. *Science* pp. science.1187582– (2010).
- [38] W. Ketterle, D. Durfee, and D. Stamper-Kurn. ‘Making, probing and understanding Bose-Einstein Condensation’. *arXiv:cond-mat/9904034v2* (1999).
- [39] M. Greiner, O. Mandel, T. Esslinger, T. W. Hansch, and I. Bloch. ‘Quantum phase transition from a superfluid to a Mott insulator in a gas of ultracold atoms’. *Nature* **415**, 39 (2002).
- [40] M. Albiez, R. Gati, J. Fölling, S. Hunsmann, M. Cristiani, and M. K. Oberthaler. ‘Direct Observation of Tunneling and Nonlinear Self-Trapping in a Single Bosonic Josephson Junction’. *Phys. Rev. Lett.* **95**(1), 010402– (2005).
- [41] S. Levy, E. Lahoud, I. Shomroni, and J. Steinhauer. ‘The a.c. and d.c. Josephson effects in a Bose-Einstein condensate’. *Nature* **449**(7162), 579–583 (2007).
- [42] J. Esteve, C. Gross, A. Weller, S. Giovanazzi, and M. K. Oberthaler. ‘Squeezing and entanglement in a Bose-Einstein condensate’. *Nature* **455**(7217), 1216–1219 (2008).
- [43] B. D. Josephson. ‘The discovery of tunnelling supercurrents’. *Rev. Mod. Phys.* **46**(2), 251– (1974).
- [44] G. Roati, F. Riboli, G. Modugno, and M. Inguscio. ‘Fermi-Bose Quantum Degenerate ^{40}K – ^{87}Rb Mixture with Attractive Interaction’. *Phys. Rev. Lett.* **89**, 150403 (2002).
- [45] J. Goldwin, S. Inouye, M. L. Olsen, B. Newman, B. D. DePaola, and D. S. Jin. ‘Measurement of the interaction strength in a Bose-Fermi mixture with ^{87}Rb and ^{40}K ’. *Phys. Rev. A* **70**, 021601 (2004).
- [46] M. Köhl, H. Moritz, T. Stöferle, K. Günter, and T. Esslinger. ‘Fermionic Atoms in a Three Dimensional Optical Lattice: Observing Fermi Surfaces, Dynamics, and Interactions’. *Phys. Rev. Lett.* **94**, 080403 (2005).
- [47] S. Aubin, S. Myrskog, M. H. T. Extavour, L. J. Leblanc, D. McKay, A. Stummer, and J. H. Thywissen. ‘Rapid sympathetic cooling to Fermi degeneracy on a chip’. *Nature Physics* **2**, 384 (2006).

-
- [48] S. Ospelkaus, C. Ospelkaus, R. Dinter, J. Fuchs, M. Nakat, K. Sengstock, and K. Bongs. ‘Degenerate K-Rb Fermi-Bose gas mixtures with large particle numbers’. *Journal of Modern Optics* **54**(5), 661–673 (2007).
- [49] C. Klempt, T. Henninger, O. Topic, J. Will, S. Falke, W. Ertmer, and J. Arlt. ‘Transport of a quantum degenerate heteronuclear Bose-Fermi mixture in a harmonic trap’. *The European Physical Journal D - Atomic, Molecular, Optical and Plasma Physics* **48**(1), 121–126 (2008).
- [50] S. R. Granade, M. E. Gehm, K. M. O’Hara, and J. E. Thomas. ‘All-Optical Production of a Degenerate Fermi Gas’. *Phys. Rev. Lett.* **88**, 120405 (2002).
- [51] Z. Hadzibabic, C. A. Stan, K. Dieckmann, S. Gupta, M. W. Zwierlein, A. Görlitz, and W. Ketterle. ‘Two-Species Mixture of Quantum Degenerate Bose and Fermi Gases’. *Phys. Rev. Lett.* **88**, 160401 (2002).
- [52] S. Jochim, M. Bartenstein, A. Altmeyer, G. Hendl, C. Chin, J. H. Denschlag, and R. Grimm. ‘Pure Gas of Optically Trapped Molecules Created from Fermionic Atoms’. *Phys. Rev. Lett.* **91**, 240402 (2003).
- [53] C. Silber, S. Günther, C. Marzok, B. Deh, P. W. Courteille, and C. Zimmermann. ‘Quantum-Degenerate Mixture of Fermionic Lithium and Bosonic Rubidium Gases’. *Phys. Rev. Lett.* **95**, 170408 (2005).
- [54] J. Fuchs, G. J. Duffy, G. Veeravalli, P. Dyke, M. Bartenstein, C. J. Vale, P. Hannaford, and W. J. Rowlands. ‘Molecular Bose Einstein condensation in a versatile low power crossed dipole trap’. *J. Phys. B* **40**, 4109 (2007).
- [55] Y. Inada, M. Horikoshi, S. Nakajima, M. Kuwata-Gonokami, M. Ueda, and T. Mukaiyama. ‘Critical Temperature and Condensate Fraction of a Fermion Pair Condensate’. *Phys. Rev. Lett.* **101**(18), 180406– (2008).
- [56] M. Taglieber, A.-C. Voigt, T. Aoki, T. W. Hänsch, and K. Dieckmann. ‘Quantum Degenerate Two-Species Fermi-Fermi Mixture Coexisting with a Bose-Einstein Condensate’. *Phys. Rev. Lett.* **100**(1), 010401– (2008).
- [57] F. Spiegelhalder, A. Trenkwalder, D. Naik, G. Kerner, E. Wille, G. Hendl, F. Schreck, and G. R. ‘All-optical production of a degenerate mixture of 6Li and 40K and creation of heteronuclear molecules’. *arXiv:1001.5253v1* (2010).
- [58] S. Jochim. ‘Bose-Einstein Condensation of Molecules’. Ph.D. thesis, Leopold-Franzens-Universität Innsbruck (2004).
- [59] J. V. Prodan, W. D. Phillips, and H. Metcalf. ‘Laser Production of a Very Slow Monoenergetic Atomic Beam’. *Phys. Rev. Lett.* **49**(16), 1149– (1982).

- [60] E. L. Raab, M. Prentiss, A. Cable, S. Chu, and D. E. Pritchard. ‘Trapping of Neutral Sodium Atoms with Radiation Pressure’. *Phys. Rev. Lett.* **59**(23), 2631–(1987).
- [61] K. M. O’Hara, M. E. Gehm, S. R. Granade, and J. E. Thomas. ‘Scaling laws for evaporative cooling in time-dependent optical traps’. *Phys. Rev. A* **64**(5), 051403–(2001).
- [62] A. Mosk, S. Jochim, H. Moritz, T. Elsässer, M. Weidemüller, and R. Grimm. ‘Resonator-enhanced optical dipole trap for fermionic lithium atoms’. *Opt. Lett.* **26**(23), 1837–1839 (2001).
- [63] R. Grimm, M. Weidemüller, and Y. B. Ovchinnikov. ‘Optical dipole traps for neutral atoms’. *Adv. At. Mol. Opt. Phys.* **42**, 95 (2000).
- [64] T. L. Gustavson, A. P. Chikkatur, A. E. Leanhardt, A. Görlitz, S. Gupta, D. E. Pritchard, and W. Ketterle. ‘Transport of Bose-Einstein Condensates with Optical Tweezers’. *Phys. Rev. Lett.* **88**(2), 020401– (2001).
- [65] Q. Zhou and T. Ho. ‘Universal Thermometry for Quantum Simulation’. *arXiv:0908.3015* (2009).
- [66] I. Bloch, J. Dalibard, and W. Zwerger. ‘Many-body physics with ultracold gases’. *Rev. Mod. Phys.* **80**, 885 (2008).
- [67] N. Gemelke, X. Zhang, C.-L. Hung, and C. Chin. ‘In situ observation of incompressible Mott-insulating domains in ultracold atomic gases’. *Nature* **460**(7258), 995–998 (2009).
- [68] C. J. Pethick and H. Smith. *Bose-Einstein Condensation in Dilute Gases* (Cambridge University Press, 2002).
- [69] L. Landau and E. Lifschitz. *Quantenmechanik* (Akademie-Verlag Berlin, 1979).
- [70] H. Feshbach. ‘Unified theory of nuclear reactions’. *Ann. Phys.* **5**, 357 (1958).
- [71] A. J. Moerdijk, B. J. Verhaar, and A. Axelsson. ‘Resonances in ultracold collisions of ${}^6\text{Li}$, ${}^7\text{Li}$, and ${}^{23}\text{Na}$ ’. *Phys. Rev. A* **51**, 4852 (1995).
- [72] S. Inouye, M. R. Andrews, J. Stenger, H.-J. Miesner, D. M. Stamper-Kurn, and W. Ketterle. ‘Observation of Feshbach resonances in a Bose-Einstein condensate’. *Nature* **392**, 151 (1998).
- [73] K. M. O’Hara, S. L. Hemmer, S. R. Granade, M. E. Gehm, J. E. Thomas, V. Venturi, E. Tiesinga, and C. J. Williams. ‘Measurement of the zero crossing in a Feshbach resonance of fermionic ${}^6\text{Li}$ ’. *Phys. Rev. A* **66**(4), 041401– (2002).

-
- [74] L. N. Cooper. ‘Bound Electron Pairs in a Degenerate Fermi Gas’. *Phys. Rev.* **104**, 1189 (1956).
- [75] W. Ketterle and M. W. Zwierlein. ‘Making, probing and understanding ultracold Fermi gases’. Proceedings of the International School of Physics "Enrico Fermi", Course CLXIV, Varenna, edited by M. Inguscio, W. Ketterle, and C. Salomon, IOS Press, Amsterdam (2008). 0801.2500.
- [76] A. Perali, P. Pieri, L. Pisani, and G. C. Strinati. ‘BCS-BEC Crossover at Finite Temperature for Superfluid Trapped Fermi Atoms’. *Phys. Rev. Lett.* **92**, 220404 (2004).
- [77] M. Randeria. ‘Crossover from BCS Theory to Bose-Einstein Condensation’. in *Bose-Einstein Condensation*, edited by A. Griffin, D. Snoke and S. Stringari (1993).
- [78] T.-L. Ho. ‘Universal Thermodynamics of Degenerate Quantum Gases in the Unitarity Limit’. *Phys. Rev. Lett.* **92**(9), 090402– (2004).
- [79] T.-L. Ho and E. J. Mueller. ‘High Temperature Expansion Applied to Fermions near Feshbach Resonance’. *Phys. Rev. Lett.* **92**(16), 160404– (2004).
- [80] D. A. Butts and D. S. Rokhsar. ‘Trapped Fermi gases’. *Phys. Rev. A* **55**, 4346 (1997).
- [81] Y. Castin and R. Dum. ‘Bose-Einstein Condensates in Time Dependent Traps’. *Phys. Rev. Lett.* **77**, 5315 (1996).
- [82] Y. Kagan, E. L. Surkov, and G. V. Shlyapnikov. ‘Evolution of a Bose gas in anisotropic time-dependent traps’. *Phys. Rev. A* **55**, R18 (1997).
- [83] C. Menotti, P. Pedri, and S. Stringari. ‘Expansion of an Interacting Fermi Gas’. *Phys. Rev. Lett.* **89**, 250402 (2002).
- [84] B. DeMarco. ‘Quantum behavior of an atomic Fermi gas’. Ph.D. thesis, University of Colorado (2001).
- [85] F. Kuypers. *Klassische Mechanik* (Wiley-VCH, Weinheim, 1997).
- [86] M. Bartenstein, A. Altmeyer, S. Riedl, R. Geursen, S. Jochim, C. Chin, J. Hecker-Denschlag, R. Grimm, A. Simoni, E. Tiesinga, C. J. Williams, and P. S. Julienne. ‘Precise determination of ^6Li cold collision parameters by radio-frequency spectroscopy on weakly bound molecules’. *Phys. Rev. Lett.* **94**, 103201 (2005).
- [87] C. Chin, R. Grimm, P. Julienne, and E. Tiesinga. ‘Feshbach resonances in ultracold gases’. *Rev. Mod. Phys.* **82**(2), 1225– (2010).

- [88] C. Chin. ‘A simple model of Feshbach molecules’. *arXiv:cond-mat/0506313v2* (2005).
- [89] D. S. Petrov, C. Salomon, and G. V. Shlyapnikov. ‘Weakly Bound Dimers of Fermionic Atoms’. *Phys. Rev. Lett.* **93**, 090404 (2004).
- [90] C. A. Regal, C. Ticknor, J. L. Bohn, and D. S. Jin. ‘Creation of ultracold molecules from a Fermi gas of atoms’. *Nature* **424**, 47 (2003).
- [91] J. Cubizolles, T. Bourdel, S. J. J. M. F. Kokkelmans, G. V. Shlyapnikov, and C. Salomon. ‘Production of Long-Lived Ultracold ^2Li Molecules from a Fermi Gas’. *Phys. Rev. Lett.* **91**, 240401 (2003).
- [92] H. Ott. ‘Supraleitung’. In *Lecture notes on superconductivity* (2006).
- [93] C. N. Yang. ‘Concept of Off-Diagonal Long-Range Order and the Quantum Phases of Liquid He and of Superconductors’. *Rev. Mod. Phys.* **34**, 694 (1962).
- [94] D. D. Osheroff, R. C. Richardson, and D. M. Lee. ‘Evidence for a New Phase of Solid He3’. *Phys. Rev. Lett.* **28**(14), 885– (1972).
- [95] J. Bednorz and K. Müller. ‘Possible high-Tc superconductivity in the Ba-La-Cu-O system’. *Z. Phys B* **64**, 189 (1986).
- [96] J. Kinast, A. Turlapov, J. E. Thomas, Q. Chen, J. Stajic, and K. Levin. ‘Heat Capacity of a Strongly Interacting Fermi Gas’. *Science* **307**, 1296 (2005).
- [97] L. Luo, B. Clancy, J. Joseph, J. Kinast, and J. E. Thomas. ‘Measurement of the Entropy and Critical Temperature of a Strongly Interacting Fermi Gas’. *Phys. Rev. Lett.* **98**, 080402 (2007).
- [98] J. T. Stewart, J. P. Gaebler, C. A. Regal, and D. S. Jin. ‘Potential Energy of a ^{40}K Fermi Gas in the BCS-BEC Crossover’. *Phys. Rev. Lett.* **97**, 220406 (2006).
- [99] W. Meissner and R. Ochsenfeld. ‘Ein neuer Effekt bei Eintritt der Supraleitfähigkeit’. *Naturwissenschaften* **21**, 787 (1933).
- [100] M. W. Zwierlein, C. H. Schunck, A. Schirotzek, and W. Ketterle. ‘Direct observation of the superfluid phase transition in ultracold Fermi gases’. *Nature* **442**, 54 (2006).
- [101] M. E. Gehm. ‘Properties of ^6Li ’. Ph.D. thesis, Duke University (2003).
- [102] R. D. Swenumson and U. Even. ‘Continuous flow reflux oven as the source of an effusive molecular Cs beam’. *Review of Scientific Instruments* **52**(4), 559–561 (1981).

-
- [103] J. O’Hanlon. *A User’s Guide to Vacuum Technology* (Wiley, New York, 1989).
- [104] W. Petrich, M. H. Anderson, J. R. Ensher, and E. A. Cornell. ‘Stable, Tightly Confining Magnetic Trap for Evaporative Cooling of Neutral Atoms’. *Phys. Rev. Lett.* **74**, 3352 (1995).
- [105] J. Dalibard and C. Cohen-Tannoudji. ‘Laser cooling below the Doppler limit by polarization gradients: simple theoretical models’. *J. Opt. Soc. Am. B* **6**(11), 2023–2045 (1989).
- [106] A. Siegmann. *Lasers* (University Science Books, Sausalito California, 1986).
- [107] E. D. Black. ‘An introduction to Pound–Drever–Hall laser frequency stabilization’. *Am. J. Phys.* **69**, 79–87 (2001).
- [108] L. Simon and W. Strunz. ‘A Bose gas in a single-beam optical dipole trap’. *arXiv:0912.4513v1* (2009).
- [109] T. Müller. ‘PHD thesis in preparation’. Ph.D. thesis, Swiss Federal Institute of Technology, Zürich (2010/11).
- [110] E. Arimondo, M. Inguscio, and P. Violino. ‘Experimental determinations of the hyperfine structure in the alkali atoms’. *Rev. Mod. Phys.* **49**, 31 (1977).
- [111] L. Ricci, M. Weidemüller, T. Esslinger, A. Hemmerich, C. Zimmermann, V. Vuletic, W. König, and T. W. Hänsch. ‘A compact grating-stabilized diode laser system for atomic physics’. *Optics Communications* **117**(5-6), 541–549 (1995).
- [112] G. C. Bjorklund, M. D. Levenson, W. Lenth, and C. Ortiz. ‘Frequency modulation (FM) spectroscopy’. *Applied Physics B: Lasers and Optics* **32**(3), 145–152 (1983).
- [113] U. Schunemann, H. Engler, R. Grimm, M. Weidemüller, and M. Zielonkowski. ‘Simple scheme for tunable frequency offset locking of two lasers’. *Rev. Sci. Instrum.* **70**(1), 242–243 (1999).
- [114] C. Zipkes. ‘Lasersystem zum Kühlen, Fangen und Abbilden von fermionischem Lithium’. In *Diploma Thesis, ETH Zürich* (2007).
- [115] C. G. Townsend, N. H. Edwards, C. J. Cooper, K. P. Zetie, C. J. Foot, A. M. Steane, P. Szriftgiser, H. Perrin, and J. Dalibard. ‘Phase-space density in the magneto-optical trap’. *Phys. Rev. A* **52**, 1423 (1995).
- [116] J. Fortagh, A. Grossmann, T. W. Hänsch, and C. Zimmermann. ‘Fast loading of a magneto-optical trap from a pulsed thermal source’. *J. Appl. Phys.* **84**(12), 6499–6501 (1998).

- [117] C. H. Schunck, M. W. Zwierlein, C. A. Stan, S. M. F. Raupach, W. Ketterle, A. Simoni, E. Tiesinga, C. J. Williams, and P. S. Julienne. ‘Feshbach resonances in fermionic ${}^6\text{Li}$ ’. *Phys. Rev. A* **71**(4), 045601– (2005).
- [118] G. Reinaudi, T. Lahaye, Z. Wang, and D. Guéry-Odelin. ‘Strong saturation absorption imaging of dense clouds of ultracold atoms’. *Opt. Lett.* **32**(21), 3143–3145 (2007).
- [119] Y. Shin, M. W. Zwierlein, C. H. Schunck, A. Schirotzek, and W. Ketterle. ‘Observation of Phase Separation in a Strongly Interacting Imbalanced Fermi Gas’. *Phys. Rev. Lett.* **97**, 030401 (2006).
- [120] C. C. Bradley, C. A. Sackett, and R. G. Hulet. ‘Bose-Einstein Condensation of Lithium: Observation of Limited Condensate Number’. *Phys. Rev. Lett.* **78**(6), 985– (1997).
- [121] T. Müller, B. Zimmermann, J. Meineke, J. Brantut, T. Esslinger, and H. Moritz. ‘Local observation of antibunching in a trapped Fermi gas’. *arXiv:1005.0302v1* (2010).
- [122] R. Hanbury Brown and R. Twiss. ‘A Test of a New Type of Stellar Interferometer on Sirius’. *Nature* **178**, 1046 (1956).
- [123] G. Baym. ‘The Physics of Hanbury Brown–Twiss Intensity Interferometry: from Stars to Nuclear Collisions’. *Acta Phys. Pol B* **29**, 1839 (1998).
- [124] M. Yasuda and F. Shimizu. ‘Observation of Two-Atom Correlation of an Ultracold Neon Atomic Beam’. *Phys. Rev. Lett.* **77**(15), 3090– (1996).
- [125] E. Altman, E. Demler, and M. D. Lukin. ‘Probing many-body states of ultracold atoms via noise correlations’. *Phys. Rev. A* **70**(1), 013603– (2004).
- [126] A. Öttl, S. Ritter, M. Köhl, and T. Esslinger. ‘Correlations and Counting Statistics of an Atom Laser’. *Phys. Rev. Lett.* **95**(9), 090404– (2005).
- [127] S. Fölling, F. Gerbier, A. Widera, O. Mandel, T. Gericke, and I. Bloch. ‘Spatial quantum noise interferometry in expanding ultracold atom clouds’. *Nature* **434**(7032), 481–484 (2005).
- [128] M. Schellekens, R. Hoppeler, A. Perrin, J. V. Gomes, D. Boiron, A. Aspect, and C. I. Westbrook. ‘Hanbury Brown Twiss Effect for Ultracold Quantum Gases’. *Science* **310**(5748), 648–651 (2005).
- [129] J. Esteve, J.-B. Trebbia, T. Schumm, A. Aspect, C. I. Westbrook, and I. Bouchoule. ‘Observations of Density Fluctuations in an Elongated Bose Gas: Ideal Gas and Quasicondensate Regimes’. *Phys. Rev. Lett.* **96**(13), 130403– (2006).

-
- [130] M. Henny, S. Oberholzer, C. Strunk, T. Heinzel, K. Ensslin, M. Holland, and C. Schönberger. ‘The Fermionic Hanbury Brown and Twiss Experiment’. *Science* **284**(5412), 296–298 (1999).
- [131] W. D. Oliver, J. Kim, R. C. Liu, and Y. Yamamoto. ‘Hanbury Brown and Twiss-Type Experiment with Electrons’. *Science* **284**(5412), 299–301 (1999).
- [132] M. Iannuzzi, A. Orecchini, F. Sacchetti, P. Facchi, and S. Pascazio. ‘Direct Experimental Evidence of Free-Fermion Antibunching’. *Phys. Rev. Lett.* **96**(8), 080402– (2006).
- [133] T. Rom, T. Best, D. van Oosten, U. Schneider, S. Fölling, B. Paredes, and I. Bloch. ‘Free fermion antibunching in a degenerate atomic Fermi gas released from an optical lattice’. *Nature* **444**, 733 (2006).
- [134] T. Jeltjes, J. M. McNamara, W. Hogervorst, W. Vassen, V. Krachmalnicoff, M. Schellekens, A. Perrin, H. Chang, D. Boiron, A. Aspect, and C. I. Westbrook. ‘Comparison of the Hanbury Brown-Twiss effect for bosons and fermions’. *Nature* **445**(7126), 402–405 (2007).
- [135] A. G. Basden, C. A. Haniff, and C. D. Mackay. ‘Photon counting strategies with low-light-level CCDs’. *Mon. Not. R. Astron. Soc.* **345**, 985–991 (2003).
- [136] K. Matsuo, M. Teich, and B. Saleh. ‘A Theory of Multiplication Noise’. *IEEE T. Electron Dev.* **32**, 2615 (1985).
- [137] K. Huang. *Statistical Mechanics* (Wiley, New York, 1987).
- [138] O. J. Luiten, M. W. Reynolds, and J. T. M. Walraven. ‘Kinetic theory of the evaporative cooling of a trapped gas’. *Phys. Rev. A* **53**(1), 381– (1996).
- [139] S. Manz, R. Bücker, T. Betz, C. Koller, S. Hofferberth, I. E. Mazets, A. Imambekov, E. Demler, A. Perrin, J. Schmiedmayer, and T. Schumm. ‘Two-point density correlations of quasicondensates in free expansion’. *Phys. Rev. A* **81**(3), 031610– (2010).
- [140] G. M. Bruun, B. M. Andersen, E. Demler, and A. S. Sørensen. ‘Probing Spatial Spin Correlations of Ultracold Gases by Quantum Noise Spectroscopy’. *Phys. Rev. Lett.* **102**(3), 030401– (2009).

Acknowledgements - Danksagung

Vor etwa sieben Jahren wurde ich mit Experimenten zur Bose-Einstein Kondensation vertraut gemacht, und das nur Dank einem kleinen Missverständnis, denn ich sass in der falschen Vorlesung. Beim Zuhören hatte ich das erste Mal das Gefühl, dass Quantenmechanik etwas Aufregendes, ja Lebendiges an sich hat. Speziell die BEC-Apparaturen, die uns während einer Laborführung erklärt wurden, fasziierten mich.

Heute möchte ich mich ganz herzlich bei Tilman Esslinger bedanken. Er hat mein Interesse für die Quantenoptik geweckt. Er hat mich über all die Jahre persönlich begleitet und mich mit seiner positiven Art gefördert. Ich durfte bei ihm die Semesterarbeit, die Diplomarbeit und nun die Doktorarbeit machen. Unter hervorragenden Arbeitsbedingungen zusammen mit einem motivierten Team bekam ich die Möglichkeit, selber eine Apparatur aufzubauen! Vor allem im Schlusspurt meiner Doktorarbeit durfte ich auf Tilmans Unterstützung zählen. Ganz herzlich bedanken möchte ich mich auch bei:

Beim Lithium Team,

- Henning Moritz für die gute Anleitung, Rat und Tat, und vorallem für die Geduld, die er aufbrachte.
- Torben Müller für die tolle Zusammenarbeit. Wir haben die schwierigsten Aufbau- und Experimentierphasen gut gemeistert!
- Jakob Meineke für die vielen Diskussionen und Beiträge, ohne die ich nur mühsam weitergekommen wäre. Zu jeder Tat ein Zitat – das wird mir fehlen.
- Jean-Philippe Brantut für seine wichtigen Impulse und Beiträge, von denen wir schon nach sehr kurzer Zeit profitieren durften.
- David (Michi) Stadler für die Hilfsbereitschaft in allen Belangen. Gib Acht mit der Resonatoreinkopplung!

bei den technischen Mitarbeitern,

- Alexander Frank, unserem Elektroingenieur für seine Expertise in allen Bereichen der Elektronik und für die Nachsicht bei der Rückgabe von zerstörten Elektronikkomponenten.
- Andreas Stuker und Bernhard Morat, stellvertretend für alle Mitarbeiter der Werkstatt, für die termingerechte und präzise Erfüllung aller Aufträge.
- Marcel Bär und Walter Bachmann für die Beratung in CAD und Konstruktion. Marcel hat das Konzept des optischen Resonators hervorragend umgesetzt und auch einige schöne CAD-Bilder für uns gemacht.
- Paul Herrmann für seinen Beitrag zum Bau und zur Revision des Ofens, für die Zeeman Slower-Aussenkühlung und für die vielen Tipps und Tricks.
- Hansruedi Scherrer, für die prompte Beratung in Sachen Ultrahochvakuumtechnik.
- Hans-Jürg Gübeli für die Unterstützung in allen Belangen der Labortechnik, wie z.B. Laborumbau, Klimaanlage usw.
- Herrmann Wüest, stellvertretend für alle Mitarbeiter in den Lagerbetrieben, für die rasche Erfüllung aller Wünsche.

bei Veronica Bürgisser für die perfekte Administration und für die Geduld, auch in Zeiten der grössten Materialbestellschlacht.

beim ehemaligen QO-Team: Thilo Stöferle, Stephan Ritter, Toni Öttl, Kenneth Günter, Tobias Donner, Christine Guerlain und Niels Strohmaier für die vielfältige Unterstützung.

beim jetzigen QO-Team: Ferdinand Brennecke, Robert Jördens, Kristian Baumann, Daniel Greif, Letitia Tarruell, Thomas Uehlinger, Rafael Mottl und Thomas Schnyder, für eine tolle Arbeitsatmosphäre, die grosse Hilfsbereitschaft und für die vielen guten Diskussionen. Über jeden wüsste ich etwas zu berichten, erwähnen möchte ich aber nur Letitia. Sie hat mir beim Schreiben der Doktorarbeit viele Ideen und Denkanstösse gegeben, die mir sehr geholfen haben.

bei Frau Hanselmann für die Korrektur des Textes.

Ein grosser Dank geht an meine Eltern, die mich stark unterstützt haben, und auch an Renzo Biagini. Er hat mir die Augen geöffnet. Zuletzt, aber nicht weniger herzlich, danke ich meiner lieben Frau, die immer für mich da war und vor allem in den letzten Monaten auf vieles verzichtet hat.

11. Mai 2010

Curriculum Vitae

Personal data

Name: Bruno Felix Zimmermann
Date of birth: 22 January, 1980
Place of birth: Zürich, Switzerland
Citizen of: Vilters-Wangs, Wangs SG, Switzerland

Education

- 2005 – 2010 Graduate studies at the ETH Zürich, Switzerland
under the supervision of Prof. Dr. T. Esslinger
PhD thesis: *‘Microscopy of Ultra-Cold Fermionic Lithium’*
- 2005 – 2009 Physics teacher education (Didaktischer Ausweis)
at the ETH Zürich, Switzerland
- 2004 – 2005 Diploma Thesis at the ETH Zürich, Switzerland
under the supervision of Prof. Dr. T. Esslinger:
‘Aufbau einer magneto-optischen Falle für ^{39}K ’
- 1999 – 2004 Undergraduate studies in physics at the ETH Zürich, Switzerland
- 1995 – 1996 High school, Atholton High School, Columbia MD, USA
- 1992 – 1999 High school, Kantonsschule Wiedikon, Zürich, Switzerland
- 1987 – 1992 Elementary school in Birmensdorf ZH, Switzerland

